Verification Studies of

Computational Fluid Dynamics

in Fixed Bed Heat Transfer

by

ir. Michiel Nijemeisland

A Thesis

submitted to the Faculty of the

Worcester Polytechnic Institute

in partial fulfillment of the requirements for the

Degree of Master of Science

in Chemical Engineering

_____

April 2000

Approved:

_____

Prof. Dr. Anthony G. Dixon, Advisor

_____

Prof. Dr. Ravindra Datta, Department Head

Summary

Computational Fluid Dynamics (CFD) is one of the fields that has strongly developed since the recent development of faster computers and numerical modeling. CFD is also finding its way into chemical engineering on several levels. We have used CFD for detailed modeling of heat and mass transfer in a packed bed. One of the major questions in CFD modeling is whether the computer model describes reality well enough to consider it a reasonable alternative to data collection.

For this assumption a validation of CFD data against experimental data is desired. We have developed a low tube to particle, structured model for this purpose. Data was gathered both with an experimental setup and with an identical CFD model. These data sets were then compared to validate the CFD results.

Several aspects in creating the model and acquiring the data were emphasized. The final result in the simulation is dependent on mesh density (model detail) and iteration parameters. The iteration parameters were kept constant so they would not influence the method of solution. The model detail was investigated and optimized, too much detail delays the simulation unnecessarily and too little detail will distort the solution.

The amount of data produced by the CFD simulations is enormous and needs to be reduced for interpretation. The method of data reduction was largely influenced by the experimental method. Data from the CFD simulations was compared to experimental data through radial temperature profiles in the gas phase collected directly above the packed bed.

It was found that the CFD data and the experimental data show quantitatively as well as qualitatively comparable temperature profiles, with the used model detail. With several systematic variances explained CFD has shown to be an ample modeling tool for heat and mass transfer in low tube to particle (N) packed beds.

Acknowledgments

During the last three years I spent at the Worcester Polytechnic Institute I've had the privilege to work with many interesting concepts and people. Even though a Masters project is considered to be a one-man operation these things rarely are. That explains why the acknowledgment chapter is a regularly returning concept in most of these theses.

First of all, I would like to thank Professor Anthony G. Dixon, my advisor, for all the help he has provided during this project as well as for supplying the opportunity. When I thank for opportunities I also would like to thank Professor William M. Clark and Professor David D. DiBiasio, together with my advisor they supported me financially. Additionally I would like to thank the other entire faculty at WPI for their help and advice.

Naturally I am thankful towards the other graduate students in the chemical engineering department for all the cases where they supported me with ideas or distractions. I would name names but that will only certify that I would forget somebody, so thanks to one and all and some especially, you know who you are.

A few people I do want to thank specifically, my roommates, Ivo, Chris, Fred and Uta for putting up with me, and the many friends that made my stay in Worcester a pleasant one, Thank You John, Simon, Helgo, Martina, Solvi, Paul, Krista, Mirjam and many more.

Last but by no means least I would like to thank my parents and my brother for their support in my choices and their influences, which made me who I am today, thank you very much.

Michiel

Table of Contents

List of Figures

List of Tables

1. Introduction

A good qualitative understanding and an accurate quantitative description of fluid flow and heat transfer in fixed beds are necessary for the modeling of these devices. Accurate modeling of these fixed beds is complicated, especially in low tube to particle diameter ratios (N), in the range of 3-8, due to the presence of wall effects across the entire radius of the bed. With new methods such as computational fluid dynamics (CFD) it is possible to get a detailed view of the flow behavior in these beds.

1.1 Fixed Beds

Fixed or packed beds are widely used in the chemical industry. They facilitate a large variety of processes, ranging from ammonia synthesis to oxidation reactions. This large variety of processes results in a large variety of different types of fixed bed reactors. The main characteristics of these reactors are the height to diameter scale and the tube to particle diameter ratio (N).

In large fixed bed reactors with high tube to particle diameter ratios (50-500) the wall effects can usually be neglected, since the flow and heat effects of the wall will influence a relatively small part of the reactor. Reactions taking place in these types of reactors can almost be considered to be adiabatic. Often when heat transfer is of importance, the bed will be divided in several ‘pancakes’ in between which heat is added to or taken from the system. Most established models predict behavior in these beds accurately enough.

Fast heat transfer rates may be desired for reactions with extreme thermodynamics. A dysfunctional heat transfer method may result in undesired processes, deactivation of the packing or thermal runaway.

In fixed bed reactors facilitating faster heat transfer in these extremely exo- or endothermic processes is usually achieved by designing the reactor as a tube and shell reactor with narrow tubes. The internals of the narrow tubes have a very low N, in the

range 3-8. The low N causes wall effects to be present across the entire bed. These type of reactors are used for, e.g. partial oxidation reactions, ammoxidation reactions or Lurgi syntheses.

The small tube to particle ratio beds require a more accurate description of flow behavior and heat transfer for modeling. The constant velocity (plug flow) profile, or single axial velocity component with radial variation across the tube diameter, that are usually used in fixed bed reactor design are oversimplified. To be able to model small N beds more accurately, a better insight into the flow behavior is desired.

Current heat transfer models for fixed bed heat transfer lump several heat transfer mechanisms into each effective parameter, causing models to be not descriptive enough. In the literature no consensus concerning heat transfer behavior in fixed beds can be reached (Li and Finlayson, 1977; Tsotsas and Schlünder, 1990; Vortmeyer and Haidegger, 1991; Freiwald and Patterson, 1992).

1.2 Modeling of Fixed Beds

1.2.1 Earlier Problems in Modeling of Fixed Beds

As was mentioned before a large deficiency in the modeling of packed beds in industry is the assumption of plug flow. It is already generally accepted that the void fraction in unstructured beds is large near the wall and fluid flow is channeled in these areas causing radial inhomogenities in the overall flow profiles (Kalthoff and Vortmeyer, 1980; Haidegger et al., 1989; Lerou and Froment, 1977; Froment and Bischoff, 1979; Papageorgiou and Froment, 1995). These radial distributions of the axial flow have been measured by different groups outside the bed (Morales et al., 1951; Price, 1968; Schuster and Vortmeyer, 1981; Ziolkowska and Ziolkowski, 1993; Daszkowski, 1991). Direct measurements of gas flow inside the bed have not been possible yet.

Other groups measured radial profiles below the packing, averaging to get a general velocity profile by repacking a $3 < N < 11$ column several times. The measured results

were extrapolated using an extended Brinkman equation to get radial flow profiles in the bed (Bey and Eigenberger, 1997).

McGreavy et al. (1984) used Laser Doppler Velocimetry (LDV) in low N (6.5) packed beds. To be able to access the internals of the packed bed several optical access arrangements were made, these arrangements disturbed the continuity of the packing. They showed (McGreavy et al., 1986) that flow profiles in the bed were different from profiles above the bed; they found a region in the beginning of the bed where flow development took place and a region near the bed exit where flow degradation took place. This indicates that measurement of flow profiles outside (above or below) the bed is inadequate.

Recently the group of Vortmeyer reported velocity measurements taken inside a packed bed using LDV (Giese et al., 1998). Their setup consisted of all glass particles in a glass tube with a tube to particle ratio of approximately 9 using an organic mixture with a refraction index similar to the glass as a fluid. In these measurements the focus was on low Reynolds numbers, <100, and velocities were averaged to get superficial velocities.

The main focus of these groups has been the behavior of the superficial velocity and the porosity of the bed. Most groups use a number of different packing materials to find the effects of the packing on radial distributions of superficial velocities.

Thompson and Fogler (1997) used a network-model to model flow in a packed bed. The smallest element in a network model was created in a Delauney tessellation using basically one element per void in the packing. The different beds were established using a computer simulation method for creating a random bed. Computer simulation and experimental data were compared using a N = 12 bed of approximately 7500 particles. The computer simulation treated the bed as a porous medium, neglecting specifics in the flow profile. It was, however, not a homogeneous porous bed, the porosity was established using the computer generated random packed bed.

1.2.2 Computational Fluid Dynamics

Computational Fluid Dynamics (CFD) is a method that is becoming more and more popular in the modeling of flow systems in many fields, including reaction engineering (Harris et al., 1996; Ranade, 1995). CFD makes it possible to numerically solve flow and energy balances in complicated geometries. The results show specific flow and heat transfer patterns that are hard to obtain with conventional modeling methods.

The CFD approach uses Navier Stokes equations and energy balances over control volumes, small volumes within the geometry at a defined location representing the reactor internals. The size and number of control volumes (mesh density) is user determined and will influence the accuracy of the solutions to a degree. After boundary conditions have been introduced in the system the flow and energy balances are solved numerically. An iteration process decreases the error in the solution until a satisfactory result has been reached.

By using CFD in the simulation of fixed bed reactors a detailed description of the flow behavior within the bed can be established, which can then be used in more accurate modeling. The simulation requires that a model of the desired geometry be made.

CFD studies towards heat transfer and flow behavior in fixed bed reactors have been performed previously. The earliest CFD fixed bed simulations used two-dimensional models. Dalman et al. (1986) investigated in an axisymmetric radial plane, this limited the packing possibilities severely but gave a first insight in flow patterns in fixed beds. This study showed that eddies formed in between the spheres which led to a region of poor heat transfer. The effect of Re and Pr numbers on this process were also investigated, and showed an increasing problem with heat transfer as the Reynolds number increased. Lloyd and Boehm (1994) did a very similar two-dimensional study; they used a commercial FE package FIDAP and 8 instead of 2 spheres in line. In this study the influence of the sphere spacing on the drag coefficients was investigated. It was also found that heat transfer from the spheres decreased with decreased sphere spacing.

Three-dimensional models have also been researched earlier; a 3-sphere model (Derkx and Dixon, 1996) was one of the first models in this area. This study focused on obtaining Nu_w numbers. An 8 sphere model followed (Logtenberg and Dixon, 1998a; 1998b) the packing was modeled as two layers of four spheres. Effective heat transfer parameters estimated from these CFD results matched theoretical model predictions reasonably well (Dixon and Creswell, 1979). This study was limited by the absence of contact points between the spheres and the wall and amongst the spheres themselves. Another point for improvement in this model was the small number of spheres, which resulted in less than realistic flow patterns.

Most recently, a 10-sphere model incorporating contact points between the particles and between the particles and the wall (Logtenberg et al., 1999) was developed. The 10-sphere model showed flow behavior and heat transfer behavior that could not be described using conventional fixed bed models. By using three-dimensional models for these simulations the packing need not be symmetrical, this way the true effects of the presence of the wall are shown, as they would be in a low N tube.

1.2.3 Other Modeling Techniques

Another method that has been used to describe flow patterns in fixed beds is Magnetic Resonance Imaging (MRI). This method shows flow patterns in complicated geometries similar to CFD modeling. The advantage of MRI over CFD is that the measurements are experimental measurements whereas the CFD data is generated through modeling. Therefore MRI need not be validated against experimental results. The disadvantage of the MRI compared to CFD is that it requires experimental setup and does not give any information on heat transfer; also it can only be done with fluids that are susceptible for the method.

The method has been reported in literature on many occasions and can be used as an experimental comparison against CFD results. Several groups have done MRI research in packed beds, (Kutsovsky et al. 1996; Sederman et al., 1997; Park and Gibbs, 1999).

Results of these studies are contained in velocity distribution plots that are easily comparable with CFD data. Generally the packed beds used for MRI have a considerably higher tube to particle ratio, which will result in less pronounced wall effects. Also in general the MRI experiments are conducted at low Reynolds numbers, most are $Re < 100$.

Qualitatively the MRI results show generally accepted flow concepts such as flow increase in bed voids, as well as not homogeneous velocity distribution in different pores (Sederman et al., 1997). The larger tube to particle ratio also allows for a statistical view of the velocity distribution over the column cross section. When averaged over a long evolution time the data approached Gaussian behavior (Park and Gibbs, 1999). With a tube to particle ratio of 6.7 and Reynolds numbers ranging from 14.9 to 44.8 the velocity profile is roughly parabolic with the maximum being near the center of the tube. Also negative velocities or reversed flow within the bed are shown (Kutsovsky et al., 1996).

1.3 Validation of Computational Fluid Dynamics Results

When CFD data is to be used, as data for modeling, it is imperative it is checked to be viable and reliable data. All the data that is produced by the CFD simulations are numerically determined and are dependent on system defined boundary conditions and user defined solution parameters. It is assumed that the theoretical model that is the background for CFD is viable for what it is describing and that this could be scaled up to macroscopic models.

In this thesis a direct comparison between CFD-generated data and experimental data will be made. Heat transfer experiments have been conducted in a heated wall tube with a well defined packing of spheres. An identical geometric model of this experimental setup has been created for CFD simulations. A series of experiments has been performed with identical boundary conditions both in the experimental setup and as a CFD simulation.

Data gathered in the experimental setup consisted of radial temperature profiles at several bed heights. The CFD data was reduced to give a similar temperature profile at

the same bed heights. The data was directly compared in a temperature versus radial coordinate plot.

2. Computational Fluid Dynamics

The application field for CFD as a modeling tool is constantly expanding. Improvements in computer hardware, computational speed and memory size, as well as improvements in software capabilities make CFD a feasible and accessible tool in a large range of applications.

2.1 History of Computational Fluid Dynamics

The relatively young field of CFD is fast growing due to increasing computer capabilities and a growing field of applications. It is an established research tool in mechanical and civil engineering where it is used for stress calculations in solid structures. It has also been used in for example the automobile and airplane industry to replace expensive wind tunnel testing of new designs. Recently CFD has been introduced in the field of chemical engineering with the introduction of specific fluid mixing programs and the option to solve for chemical reactions (Bode, 1994; Harris et al., 1996; Ranade, 1995).

Commercially available CFD codes use one of three basic spatial discretization methods, finite difference (FD), finite volume (FV) or finite element (FE). The first CFD codes written used FD or FV methods and have been used over a variety of flow problems. The major disadvantage of the FD method is that it is limited to structured grids, which are hard to apply to complex geometries. A structured grid is defined by the way nodes are placed in the grid. In a structured grid every node is an intersection of three lines with specific x, y and z coordinate, this limits the adaptability of the grid and all cells in these grids are rectangular. The elements in a structured grid are based on cubes that can undergo limited deformation to fit the geometry.

The FV and FE methods support both structured and unstructured grids and therefore can be applied to a more complex geometry. An unstructured grid is a three dimensional

structure of tetrahedral cells which is interpolated from a triangular surface mesh. The mesh creation of an unstructured mesh is less directly influenced by the user but adapts more easily to a complex geometry.

2.2 Theory

Solutions in CFD are obtained by numerically solving a number of balances over a large number of control volumes or elements. The numerical solution is obtained by supplying boundary conditions to the model boundaries and iteration of an initially guessed solution.

The balances, dealing with fluid flow, are based on the Navier Stokes equations for conservation of mass (continuity) and momentum. These equations are modified per case to solve a specific problem.

The control volumes or elements, the mesh, are designed to fill a large-scale geometry, described in a CAD file. The density of these elements in the overall geometry is determined by the user and affects the final solution. Too coarse a mesh will result in an oversimplified flow profile, possibly obscuring essential flow characteristics. Too fine a mesh will unnecessarily increase iteration time.

After boundary conditions are set on the large-scale geometry the CFD code will iterate the entire mesh using the balances and the boundary conditions to find a converging numerical solution for the specific case.

2.2.1 Mesh Topology

One of the most important parts of CFD modeling is the construction of the mesh topology. The mesh establishes the accuracy of the simulation. It has to be chosen with enough detail to describe the processes accurately and with a degree of coarseness that enables solution within an acceptable amount of time. When an optimal density has been found, refining this will increase the model size without displaying more flow detail.

When it is coarsened the mesh will obscure, possibly essential, parts of the flow detail. The mesh determines a large part of creating an acceptable simulation.

2.2.1.1 Mesh density

Previously to this validation study a number of preliminary studies towards CFD simulations of packed beds have been done (Derkx and Dixon, 1996; Logtenberg and Dixon, 1998a; 1998b; Logtenberg et al., 1999). In the earlier studies the mesh density was investigated extensively. From experience from these previous studies an optimal mesh density was chosen. For the present work a short study was done to find the optimal node density, for the type of geometry used here, in a limited size model. This study focused mainly on maintaining a 3D topology that described the physical model accurately and was able to handle the flow specifics of the packed bed geometry. Also, mesh densities were varied to establish the optimal mesh density, describing the flow characteristics and limiting the calculation times.

2.2.1.2 Mesh variations

Most meshes created besides the ones needed to do the CFD validation were focused on one aspect of the mesh geometry. Initially meshes were made similar to a 10-sphere geometry as was created for a previous study with the commercial CFD package ANSYS (Logtenberg et al., 1999). These were created to focus on sphere-sphere contact points and sphere-wall contact points. The study of the 10-sphere geometry in Fluent was also made to compare the results from the different commercial codes.

When actual contact points are created, both surfaces that are contacting have one common node. In surface mesh creation this can be defined and does not pose any problems. The 3D mesh can be created relatively easily by merging a number of nodes on the contacting surfaces. When, however, a solution is iterated convergence problems occur with the fluid elements around the contact point. In a laminar case the solution

parameters can be adjusted to get a converging solution, in a turbulent case this becomes impossible.

After it was found that, with actual contact points as they were designed with the 10-sphere geometry, a turbulent solution of the model used for the CFD validation could not be established, a number of models were created to make a comparison between several sizes of gaps between the spheres in the packing. Eventually, the appropriate gaps, facilitating both a turbulent flow solution as well as sufficient stagnant fluid film around the contact point for heat transfer, were implemented.

2.2.2 Fluid Flow Fundamentals

For iteration CFD solvers use generalized fluid flow and energy balances based on the Navier Stokes equations. The balances are generalized so the user can influence which elements are added in the balance and which are not. The number of balances to be solved is also user defined; it can be advantageous to not solve all balances initially.

The generalized balances that are used by the Fluent commercial CFD package are the Navier Stokes equations for conservation of mass and momentum, when it is set to calculate laminar flow without heat transfer. Additional equations are solved for heat transfer, species mixing or reaction or κ and ε for turbulent cases. The basic equations and background of these balances are stated in the Fluent UNS User's Guide.

2.2.2.1 Navier Stokes Equations

The general equation for conservation of mass, or the continuity equation, is defined as follows:

$$\frac{\partial \rho}{\partial t} + \frac{\partial (\rho u_i)}{\partial x_i} = S_m \qquad (1)$$

The source term S_m contains the mass added through phase changes or user defined sources. In general, and in the performed simulations, the source term was equal to zero.

The equation for conservation of momentum in direction i and in a non-accelerating reference frame is given by:

$$\frac{\partial(\rho u_i)}{\partial t} + \frac{\partial(\rho u_i u_j)}{\partial x_j} = -\frac{\partial p}{\partial x_i} + \frac{\partial \tau_{ij}}{\partial x_j} + \rho g_i + F_i \qquad (2)$$

In this balance p is the static pressure, τ_{ij} is the stress tensor, ρg_i is the gravitational body force. F_i is an external body forces component; it can include forces from interaction between phases, centrifugal forces, Coriolis forces and user-defined sources. For the performed simulation it was zero.

The stress tensor τ_{ij} for a Newtonian fluid is defined by:

$$\tau_{ij} = \left[\mu\left(\frac{\partial u_i}{\partial x_j} + \frac{\partial u_j}{\partial x_i}\right)\right] - \frac{2}{3}\mu\frac{\partial u_l}{\partial x_l}\delta_{ij} \qquad (3)$$

Here μ is the molecular viscosity; the second term on the right hand side of the equation is the effect of volume dilation.

2.2.2.2 Turbulence Models

For turbulent cases the standard κ-ε model was used for the CFD simulation. The κ-ε model is a semi-empirical model; its equations are derived from the Reynolds-Averaged Navier-Stokes equations. The major assumptions in this model are that the flow is fully turbulent and the effects of molecular viscosity are negligible, therefore it can only be used for fully turbulent flows.

Several other turbulent models were available, a Renormalization Group (RNG) κ-ε model and a Reynolds Stress Model, results for these different models were compared and it was shown there were no significant differences in the results.

With Reynolds averaging the solution variables in the Navier Stokes equations are decomposed into the mean, $\overline{u}_i$, and fluctuating, u_i', components. When this is applied to the standard Navier Stokes equation (2), the result is:

$$\frac{\partial(\rho u_i)}{\partial t}+\frac{\partial(\rho u_i u_j)}{\partial x_j}=-\frac{\partial p}{\partial x_i}+\frac{\partial}{\partial x_j}\left[\mu\left(\frac{\partial u_i}{\partial x_j}+\frac{\partial u_j}{\partial x_i}\right)-\left(\frac{2}{3}\mu\frac{\partial u_l}{\partial x_l}\right)\right]+\frac{\partial\left(-\rho\overline{u_i' u_j'}\right)}{\partial x_j} \quad (4)$$

The velocities and other solution variables are now represented with time-averaged values, the effects of turbulence are represented by the 'Reynolds stresses', $\left(-\rho\overline{u_i' u_j'}\right)$, which are modeled by the Boussinesq hypothesis:

$$-\rho\overline{u_i' u_j'}=\mu_t\left(\frac{\partial u_i}{\partial x_j}+\frac{\partial u_j}{\partial x_i}\right)-\frac{2}{3}\left(\rho\kappa+\mu_t\frac{\partial u_i}{\partial x_i}\right)\delta_{ij} \quad (5)$$

The turbulent viscosity, μ_t, is defined with κ, the turbulent kinetic energy and ε, its rate of dissipation. The κ-ε turbulent model was developed and described by Launder and Spalding (1972).

$$\mu_t=\rho C_\mu\frac{\kappa^2}{\varepsilon} \quad (6)$$

The turbulent kinetic energy and its dissipation rate are taken from the adapted transport equations:

$$\frac{\partial(\rho\kappa)}{\partial t}+\frac{\partial(\rho u_i\kappa)}{\partial x_i}=\frac{\partial}{\partial x_i}\left[\left(\mu+\frac{\mu_t}{\sigma_\kappa}\right)\frac{\partial\kappa}{\partial x_i}\right]+G_\kappa+G_b-\rho\varepsilon \quad (7)$$

and

$$\frac{\partial(\rho\varepsilon)}{\partial t}+\frac{\partial(\rho u_i\varepsilon)}{\partial x_i}=\frac{\partial}{\partial x_i}\left[\left(\mu+\frac{\mu_t}{\sigma_\varepsilon}\right)\frac{\partial\varepsilon}{\partial x_i}\right]+C_{1\varepsilon}\frac{\varepsilon}{\kappa}\{G_\kappa+(1-C_{3\varepsilon})G_b\}-C_{2\varepsilon}\rho\frac{\varepsilon^2}{\kappa} \quad (8)$$

In these equations, G_κ is the generation of turbulent kinetic energy, κ, due to turbulent stress, and is defined by

$$G_\kappa=-\rho\overline{u_i' u_j'}\frac{\partial u_j}{\partial x_i} \quad (9)$$

G_b is the generation of turbulent kinetic energy, κ, due to buoyancy,

$$G_b=\beta g_i\frac{\mu_t}{Pr_t}\frac{\partial T}{\partial x_i} \quad (10)$$

Here, Pr_t is the turbulent Prandtl number for temperature or enthalpy, β is the thermal expansion coefficient,

$$\beta = -\frac{1}{\rho}\left(\frac{\partial \rho}{\partial T}\right)_p \qquad (11)$$

The model constants, $C_{1\varepsilon}$, $C_{2\varepsilon}$, C_μ, σ_κ and σ_ε were used with the default settings, these are,

$C_{1\varepsilon}$=1.44, $C_{2\varepsilon}$=1.92, C_μ=0.09, σ_κ=1.0, σ_ε=1.3 and Pr_t=0.85.

The default values have been established from experimental work with air and water and were found to work well for a wide range of wall bounded and free shear flows (Launder and Spalding, 1972). The simulation results for turbulent cases, discussed for this project, have been determined using these default values.

In a system with both heat and mass transfer an extra turbulent factor, k_t, is included, see equation (11), it is derived from an adapted energy equation, as were ε and κ. The turbulent heat transfer is dictated by turbulent viscosity, μ_t, and the turbulent Prandtl number, Pr_t.

Other effects that can be included in the turbulent model are buoyancy and compressibility effects.

2.2.2.3 Energy Equations

The energy equation in Fluent UNS is solved in the form of a transport equation for static temperature. The temperature equation is obtained from the enthalpy equation, which is only solved in special cases, by taking the temperature as a dependent variable. The enthalpy equation is defined as,

$$\frac{\partial(\rho h)}{\partial t} + \frac{\partial(\rho u_i h)}{\partial x_i} = \frac{\partial}{\partial x_i}\left(k + k_t\right)\frac{\partial T}{\partial x_i} - \frac{\partial \sum_j h_j J_j}{\partial x_i} + \frac{Dp}{Dt} + \left(\tau_{ik}\right)_{eff}\frac{\partial u_i}{\partial x_k} + S_h \qquad (12)$$

In this equation S_h includes heat of chemical reaction, any inter-phase exchange of heat, and any other user defined volumetric heat sources. k_t is defined as the conductivity due to turbulent transport,

$$k_t = \frac{c_p \mu_t}{Pr_t} \quad (13)$$

and the enthalpy h is defined as,

$$h = \sum_j m_j h_j \quad (14)$$

where m_j is the mass of species j and,

$$h_j = \int_{T_{ref}}^{T} c_{p,j} dT \quad (15)$$

Another part of the heat transfer equations is the heat transfer through solid particles within the mesh. In our study, the packed bed, this is of course an important factor. The balances for solid elements need not use flow parts, and are defined by,

$$\frac{\partial(\rho h)}{\partial t} = \frac{\partial}{\partial x_i}\left(k \frac{\partial T}{\partial x_i} \right) + \dot{q} \quad (16)$$

The last term q is the volumetric heat source, h, the sensible enthalpy is defined as,

$$h = \int_{T_{ref}}^{T} c_p dT \quad (17)$$

which is consistent with equation (14) since $c_p = \sum_j m_j c_{p,j}$.

2.2.3 Numerical Solutions

The governing partial differential equations for the conservation of momentum and scalars such as mass, energy and turbulence are solved in the integral form. Fluent UNS uses a control-volume based technique, which consists of three basic steps.

- Division of the domain into discrete control volumes using the computational grid.

- Integration of the governing equations on the control volumes to create an algebraic equation for unknowns such as pressure, velocity and scalars.
- Solution of the discretized equations.

The governing equations are solved sequentially. The fact that these equations are coupled makes it necessary to perform several iterations of the solution loop before convergence can be reached. The solution loop consists of 7 steps that are performed in order.

- The momentum equations for all directions are each solved using the current pressure values (initially the boundary condition is used), in order to update the velocity field.
- The obtained velocities may not satisfy the continuity equation locally. Using the continuity equation and the linearized momentum equation a 'Poisson-type' equation for pressure correction is derived. Using this pressure correction the pressure and velocities are corrected to achieve continuity.
- κ and ε equations are solved with corrected velocity field.
- All other equations (e.g. energy, species conservation etc.) are solved using the corrected values of the variables.
- Fluid properties are updated
- Any additional inter-phase source terms are updated.
- A check for convergence is performed.

These seven steps are continued until in the last step the convergence criteria are met.

2.3 CFD Solver and Additional Programs

To be able to conduct our CFD simulations we used a commercially available code, Fluent UNS. This code is written by Fluent Inc. and uses unstructured meshes. The CFD package consists of a number of different modules in which different parts of the process take place.

The first step, mesh creation, is done with GeoMesh, a meshing program designed and supplied by ICEM Technologies. GeoMesh creates a triangular surface mesh (see Figure 1a), which is interpolated to a tetrahedral 3D mesh by T-Grid, Fluent's 3D meshing program. These 3D meshes (see Figure 1b) are imported in Fluent UNS to impose boundary conditions, iterate and post-process the data.

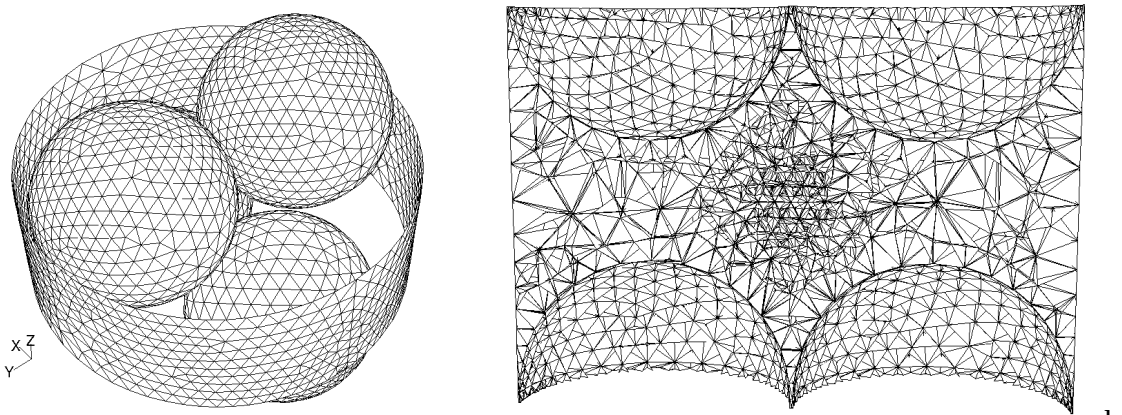

a b

Figure 1. Typical examples of a) the surface mesh on a number of spheres and a section of the cylinder and b) a section of the 3D interior mesh.

2.3.1 Surface mesh creation with GeoMesh

As was stated before, the creation of the mesh is the most important step in performing CFD, it determines the accuracy of the simulation. The GeoMesh program is the first step in mesh creation, it creates the surface mesh. The node distribution on the surface determines the eventual mesh density, and therefore is of vital importance to the simulation accuracy.

The surface mesh creation in GeoMesh consists of two major steps. In the first step the geometry of the model is established, a CAD program is used to determine dimensions. The second step is the creation of the surface mesh using the CAD geometry to place the surface mesh on.

The surface mesh consists of three major building blocks, nodes, edges and surfaces. These are hierarchical, a surface is made up of edges and an edge is made up of nodes. Several surfaces are stuck together to form the entire surface mesh.

2.3.1.1 CAD geometry design

In this phase of the model design the major topological entities are defined. The outer wall to the model is established as well as the internal structure, solid particles and fluid regions. Several entities, such as cylinders or spheres, are ready made parts that can be added to the geometry.

Before exporting the fundamental geometry it is important all curves are defined as so-called B-Spline curves, these are mathematical descriptions of the specific curves. This conversion is necessary to be able to have the surface mesh form to the exact contours of the created geometry.

2.3.1.2 Surface mesh creation

To be able to create the surface mesh the CAD geometry is imported in a separate program, P-Cube. At this time the type of mesh is determined, 2D (when a 2D mesh is created the surface mesh is also the final mesh) or 3D, and structured or unstructured. The surface mesh of a structured 3D mesh is a square mesh whereas the surface mesh of an unstructured mesh is a triangular mesh. The cubic volume mesh in the structured case causes a very ordered 3D node distribution whereas in the unstructured case the node distribution is more chaotic due to the tetrahedral mesh structure.

Another important decision that needs to be made is in what way the mesh needs to be built; there are two major methods. The first method is the top down method where surface sections are defined first and the details are added successively, edges and number of nodes per edge. The bottom up method begins with the definition of nodes.

When the mesh has areas that need to be very precisely determined the bottom up method is preferable. In this method nodes can be placed at the designated points. From these precisely placed nodes edges can be created and the edges can be combined to form surfaces. The top down method is usually preferable in simple geometries and structured meshes.

After incorporating all the essential geometric features the edges are ‘rubber-banded’ where necessary. The process of rubber-banding stretches edges to fit to the local geometric features. The next step is associating the mesh surfaces with the geometric surface, with this process not just the edge but the whole surface is fit to the local geometric features. For these two processes it is essential that the CAD surfaces are defined as B-Spline surfaces, see section 2.3.1.1.

Now before the mesh is created one more important aspect has to be determined, the mesh density. The surface mesh density is determined by the node distribution on the edges. The user defines the number of nodes on each edge in the geometry, these distributions are fully user defined. Node distribution can be dense in one part of an edge and coarse in another part. In the case of a structured mesh node distributions are only defined on master edges, usually two edges per surface; the opposite ‘slave’ edges will have the same distribution as the master edge.

With a node distribution determined on all the edges P-Cube can interpolate the surface mesh. For structured meshes interpolation is fairly easy, when the node distribution is determined the surface mesh is already determined. In an unstructured mesh the node distribution on the edges is used to create a triangular mesh with as gradual as possible a gradient of surface element size.

Before the surface mesh is finished one more step needs to be taken. All the surfaces that were created and meshed need to be labeled. In this step the walls can be numbered and therewith differentiated in later steps, fluid inlets and exits are defined. Also continuous boundaries can be defined when the geometry created is only part of a total geometry.

2.3.2 Mesh creation with T-Grid

The T-Grid program uses the surface mesh to interpolate the three dimensional mesh. This process consists of two basic steps, the initialization and the refinement.

In the initialization step surface nodes are connected through the model internals, a 3D mesh is created that is fine in constrained spaces but very coarse in large open spaces. The initial mesh can then be refined to user specifications. Usually a number of refinement processes are used to create an optimal mesh. Part of the refinement operation is a check for mesh consistency. Not only are more elements created also the interconnections between elements are updated. The consistency check makes sure all elements are connected to their neighboring elements in the desired order.

The refinement is the final part of mesh creation. It is also the last step in which mesh density can be influenced. The influence on the mesh density is constrained however by the surface mesh density, this part of the mesh can only be altered in the surface meshing program.

2.3.3 Solving the CFD problem with Fluent UNS

When a mesh is completed with its density and all other complications resolved, the actual computational part of CFD can be started. At this point the completed geometry can be imported in the solver and the CFD simulation is started.

Again a series of steps are to be performed; first, the boundary conditions on the system need to be set, next the process' iteration parameters need to be set. With the boundary conditions defined the simulation is performed. The final step in obtaining the desired data is the post-processing of the data in which the desired data sets are taken from the simulation data

2.3.3.1 Imposing boundary conditions

The boundary conditions determine the flow and thermal variables on the boundaries of the physical model. There are a number of classifications of boundary conditions:

- Flow inlet and exit boundaries: pressure inlet, velocity inlet, inlet vent, intake fan, pressure outlet, outflow, outlet fan, exhaust fan.
- Wall, repeating, and pole boundaries: wall, symmetry, periodic, axis
- Internal cell zones: fluid, solid
- Internal face boundaries: fan, radiator, porous jump, wall, interior

In our model we use a velocity inlet at the flow inlet of the column, this boundary condition defines a flow velocity at the inlet of the column. The flow exit boundary is defined as a pressure outlet; the outlet pressure is defined as atmospheric pressure. The column and packing exterior are defined as wall boundaries. The wall boundaries separate the fluid zone, air, in between the particles from the solid zones, nylon 66, inside the particles; they also constrain the fluid zone to within the column. Internal face boundaries are not used in our model.

With the determination of the boundary conditions the physical model has been defined and a numerical solution can be provided. It is now necessary to determine how the solution will be established. This can be done by setting the iteration parameters.

2.3.3.2 Setting iteration parameters

There are two main iteration parameters to be set before commencing with the simulation. The underrelaxation factor determines the solution adjustment for each iteration; the residual cut off value determines when the iteration process can be terminated.

The underrelaxation factor is an arbitrary number that determines the solution adjustment between two iterations; a high factor will result in a large adjustment and will result in a fast convergence, if the system is stable. In a less stable or particularly nonlinear system, for example in some turbulent flow or high-Rayleigh-number natural-

convection cases, a high underrelaxation may lead to divergence, an increase in error. It is therefore necessary to adjust the underrelaxation factor specifically to the system for which a solution is to be found. Lowering the underrelaxation factor in these unstable systems will lead to a smaller step change between the iterations, leading to less adjustment in each step. This slows down the iterations process but decreases the chance for divergence of the residual values.

The second parameter, the residual value, determines when a solution is converged. The residual value (a difference between the current and the former solution value) is taken as a measure for convergence. In an infinite precision process the residuals will go to zero as the process converges. On actual computers the residuals decay to a certain small value ('round-off') and then stop changing. This decay may be up to six orders of magnitude for single precision computations. By setting the upper limit of the residual values the 'cut-off' value for convergence is set. When the set value is reached the process is considered to have reached its 'round-off' value and the iteration process is stopped.

Besides adjusting these two major parameters there are other tricks to have a simulation converge. When convergence of, for example, turbulence elements in the flow balances or energy balances is problematic, using the flow solution as an initial guess can be helpful. To do this first only the velocity elements in the balances are iterated, the result of this initial run is then used as a starting point for the iteration of the complete balances. In this way the initial guess for the final solution is better and will help in getting a simulation to converge.

2.3.3.3 Post-processing the simulation data

When the simulation has converged the last data set is stored as a final solution. This data set has a record of the status of all elements in the model, temperature, densities, pressures, flow aspects etc. To be able to interpret the data it needs to be ordered and reduced to comprehensible sizes. This displaying of the data is called post-processing and

makes it possible to compare the different simulations with each other and with external data.

There are as many ways of displaying the data as there are data points so it is important to select the data representation that is required for the desired data comparison. Some of the standard options available are contour plots and velocity vector plots.

Contour plots will give a plot in the defined data point collection, this can be a plane or a volume, of contours of another variable. For example a plane can be defined as a constant x coordinate plane (y-z plane), we can then make a contour plot showing temperature contours in this plane. In the same plane a velocity contour plot can be made showing absolute velocities of the fluid in the defined plane. Other variables that can be used for contour plots are, magnitude of velocity components, turbulence components, pressure etc.

Velocity vector plots can be made to get an insight into the flow patterns in the overall geometry or detailed at specific locations. The density and magnification of the velocity vectors in the specified field can be manually changed to get a most optimal picture. The field density has a maximum limitation, the amount of elements in the model. In Figure 2 a small section of the grid is shown, Figure 3 shows the velocity vector plot that corresponds with this piece of the mesh.

Besides these qualitative data export methods it is also possible to export the numerical data in many different forms. Direct export of selected data sets is facilitated for a number of external applications; also it is possible to export data in ASCII format for further calculation.

Another method for exporting the numerical data is the two-dimensional plot function in which two data sets can be plotted against each other. This function is useful when for example radial velocity or temperature profiles need to be compared. From different simulations identical plots can be created and a direct comparison of the numerical data is possible.

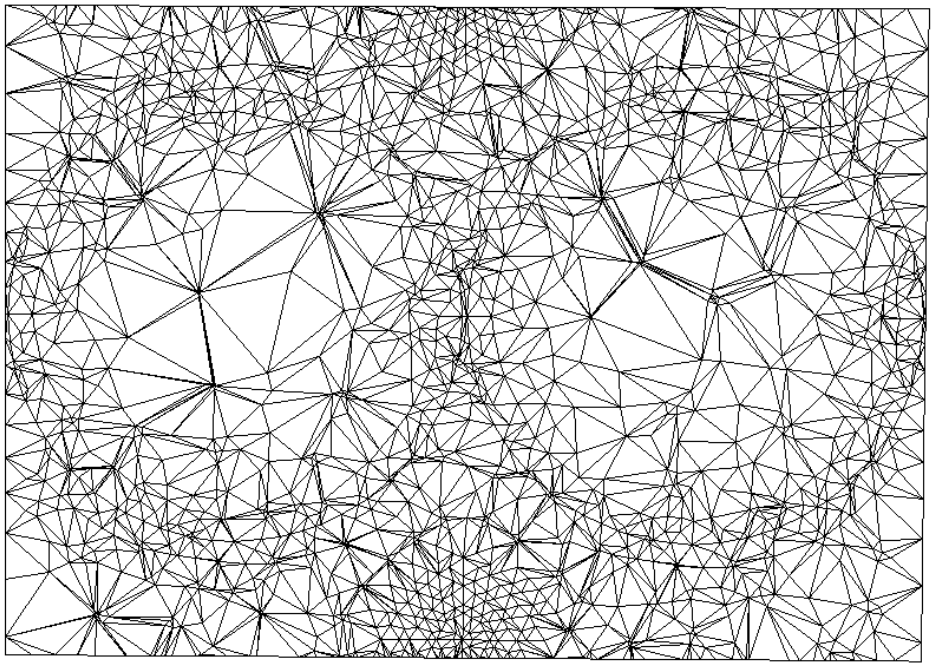

Figure 2. A section of 3D grid as it is obtained from P-Cube.

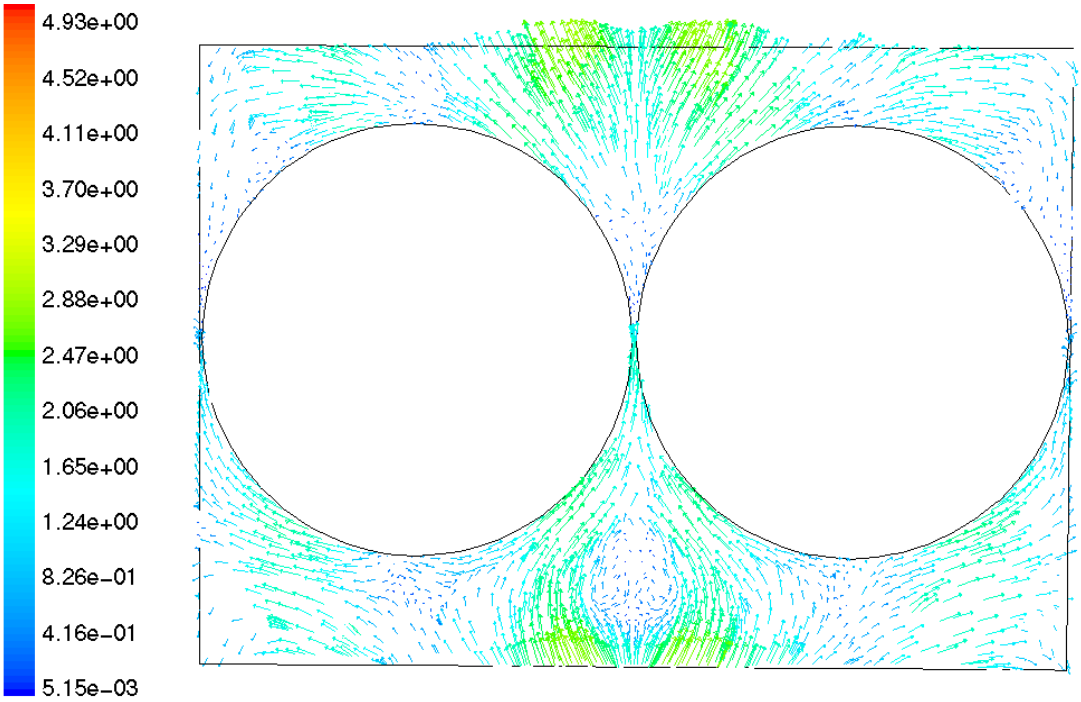

Figure 3. Velocity vector plot as obtained from Fluent UNS.

3. CFD in Fixed Bed Reactors

3.1 Introduction

Modeling of fixed bed reactors is traditionally done using pilot plant setups to determine case-specific parameters for designing and up-scaling. A major disadvantage for this type of approach is that for each design new experiments have to be done.

Many models have been developed trying to describe fixed bed reactors. All these models use a large amount of averaging to be able to describe the entire fixed bed reactor. In averaging over the entire bed many processes are lumped into a small number of parameters, which therewith lose all physical meaning. Usually for large N (tube to particle ratio) beds this averaging is an accurate enough way of modeling. For low N beds however this averaging in modeling is unacceptable.

By using CFD to thoroughly describe the flow and heat transfer processes in a fixed bed reactor we intend to create fixed bed models using physical processes such as radial and axial flow. This approach will lead to a model that is based on physical concepts that are represented by parameters. By using the detailed flow description CFD provides, it can be determined which flow aspects can be neglected and which should be adopted in a better descriptive model.

To be able to realize this model it is necessary to verify CFD results for low N beds for accuracy before using these results in modeling. For verification a low N experimental setup in which simple heat transfer is measured is used. These experimental results are then compared with CFD results from an identical geometry to show that the results produced by CFD are accurate. A direct qualitative and quantitative comparison between radial temperature profiles of both experiments and CFD simulations is made to show that the results obtained from both these measurement techniques are identical.

3.2 Computational Fluid Dynamics Models

A number of different models were used to optimize the CFD model for the verification calculations. The main model that was used was a detailed CAD copy of the experimental setup. Other models that were used in optimizing the simulations were a one-sphere model in which the fundamentals of heat transfer were compared with the CFD simulations and a detail of the experimental setup to optimize parts of the mesh.

As was discussed in Chapter 2 the creation of the mesh is very important. A substantial amount of research was conducted to find out which modeling approach would give the best simulation of the experiments and still be numerically solvable.

3.2.1 Validation against Theoretical Models

As a first introduction to Fluent a simple model was created. The model represented one sphere in a box as shown in Figure 4. The front of the box is the flow inlet; the red plane in the rear is the flow exit.

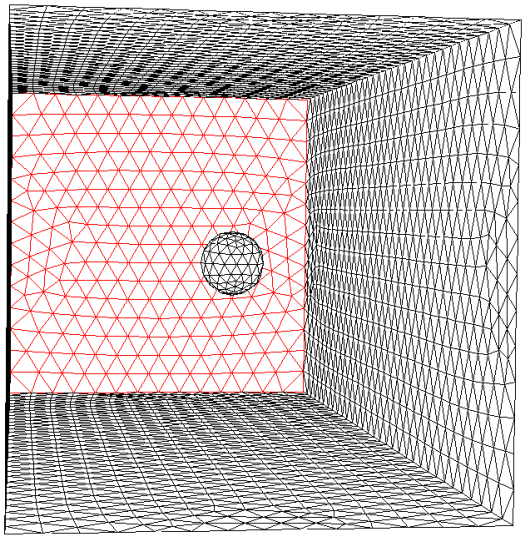

Figure 4. One sphere in a box geometry used for validation of CFD against theoretical models.

The sphere in the box was designed with the same dimensions as the spheres used in the validation model. With this model it was tried to fit CFD data to generally accepted theoretical models. The theoretical model assumes one sphere in an infinite fluid. In the CFD model the infinite fluid was limited in a box with a square flow inlet plane of 7 sphere diameters; the length of the box was 16 sphere diameters. This limitation was necessary to keep the model reasonable in size with a mesh density comparable to the validation model.

A series of runs was conducted at a number of flow velocities. In all these runs the centrally located sphere had a defined temperature of 400 K. The box wall temperature was set at 300 K to create a 100 K temperature difference between the sphere and the fluid at infinite distance. The air that flowed through the box was defined at 300 K at the entrance. The heat flux through the sphere wall was recorded after the simulation had converged.

With this data the heat transfer coefficient, h, could be determined.

$$q = h \cdot \left(T_{sphere} - T_{ambient}\right) \qquad (18)$$

When the heat transfer coefficient, h, has been determined it can be used to find the Nusselt number for the particle, which is defined as:

$$Nu_p = \frac{h \cdot d_p}{k_{air}} \qquad (19)$$

In this k_{air} is the conductivity of the fluid, 0.0242 W/m·K in our case, this is the conductivity of air at standard conditions and d_p is the particle diameter, two inches or 50.8 mm in our case.

The Nusselt number is empirically correlated as:

$$Nu_p = 2 + 0.6 \cdot Re^a \cdot Pr^b \qquad (20)$$

where a and b are case specific powers, in our case a = ½ and b = 1/3 (Ranz and Marshall, 1952).

The Nusselt number will, when there are no-flow conditions, end up to be 2, because the Reynolds number defined as $\rho vd/\mu$ will reduce to 0.

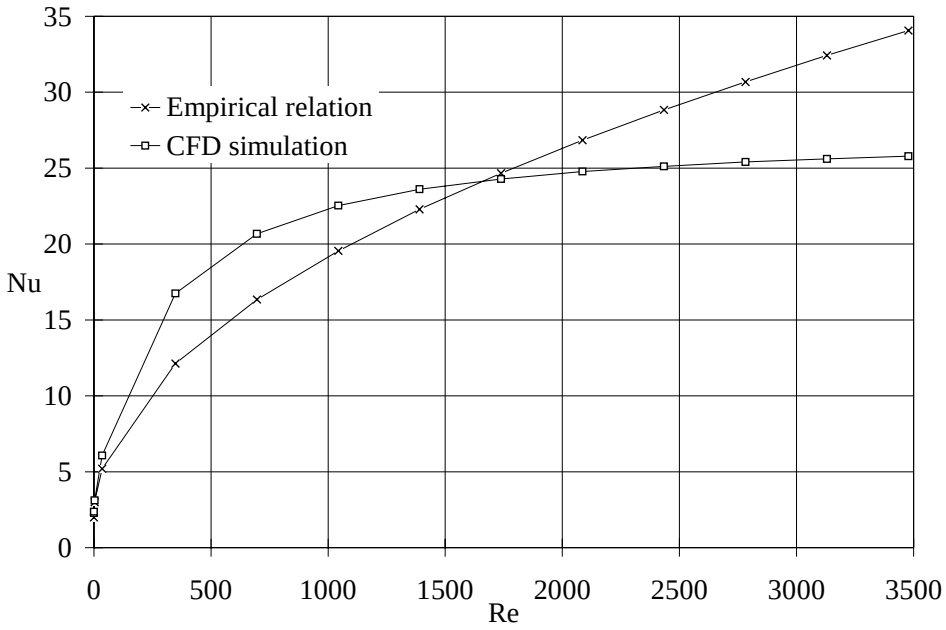

Figure 5. Nusselt number versus Reynolds number for the 48,467-element mesh.

Instead of doing one simulation at zero flow conditions a series of simulations was done at reducing flow rates to see if the value that is established at zero flow and the value it approaches at low flow conditions are similar. It was found that as the flow and the Reynolds number approached 0 the Nu_p value approached 2.29. Figure 5 shows the behavior of the empirical relation and the CFD simulations over a large range of Reynolds numbers. Figure 6 shows a closer look at the behavior at lower Reynolds numbers. The fact that the sphere is located in a box instead of in an infinite fluid may explain the deviation at a Reynolds number of 0. In this no-flow case the box in which the sphere is located might be a constraining factor on the heat transfer where this is not the case when fluid flow is present. When the Nusselt number is calculated for a particle in a spherical box according to the math by Carslaw and Jaeger (1959), it can be expressed as $Nu = \frac{2}{1 - R/R_{box}}$ at Re = 0. In our model the wall is located at 7 sphere radii, R_{box} = 7 R, resulting in a Nusselt number of 2.33 instead of 2 at a Reynolds number

of 0, which is in good agreement with the found Nusselt number of 2.29. Substantial deviation between CFD simulation and theory occurs over a range of higher Reynolds numbers, 100 < Re < 1500, which was covered experimentally.

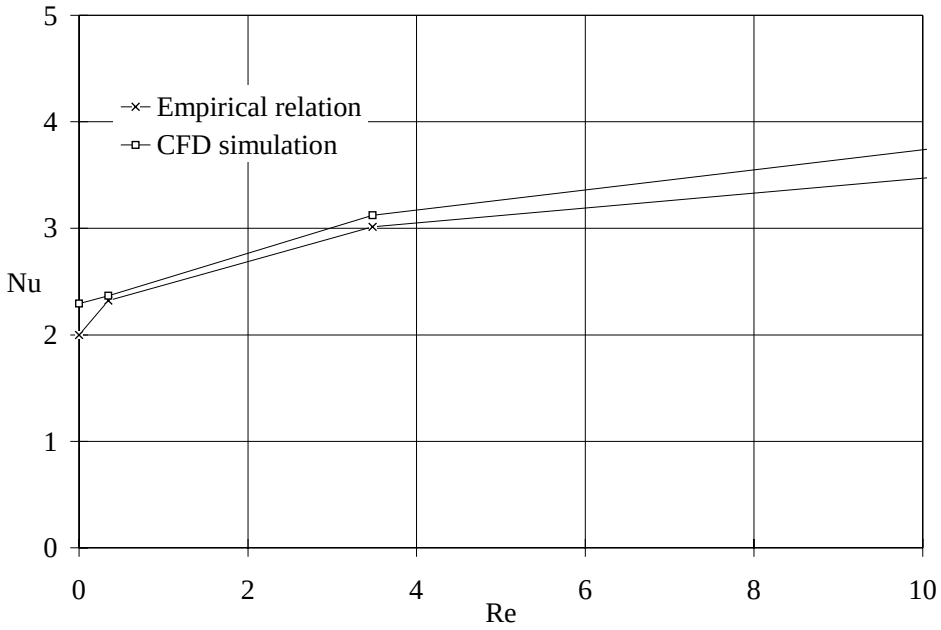

Figure 6. Close up of the low Reynolds number region of Nusselt number versus Reynolds number for the 48,467-element mesh.

Also some experiments were conducted with adapted mesh grids to determine the influence of mesh density on the outcome of the simulation. Two other meshes were created. The original mesh had a total number of cells of 48,467; a coarser mesh was made with only 7,216 cells and a finer mesh with a total of 232,593 cells. The results for these additional meshes are shown in Figure 7, all these simulations show a good agreement to the empirical relation at low Reynolds numbers with deviations at a Reynolds number of 0 and at higher Reynolds numbers. A complete overview of all simulations with these specific meshes can be found in Table 7 in appendix 1.

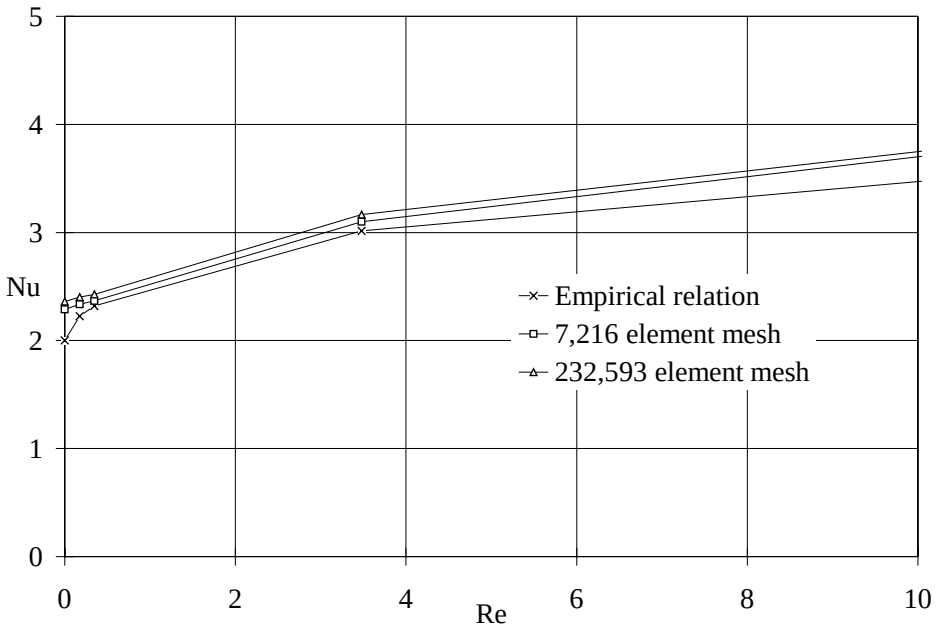

Figure 7. Nusselt number versus Reynolds number for the 232,593 and 7,216 element meshes.

3.2.2 Validation against ANSYS CFD code

To check the validity of the Fluent UNS simulation results against another commercial CFD code, as well as to get acquainted with CFD modeling in general the first complicated model was an identical copy of the model used in earlier research by Logtenberg, as was reported in Logtenberg et al. (1999).

The used model consists of 10 touching spheres in a tube in a 1, 4, 4, 1 axial setup with a resulting N of 2.43. Channeling through this geometry, which is common in tube to particle ratios between 2 and 3, was eliminated by the specific 1, 4, 4, 1 setup in which the top and bottom layer of one single sphere block the central opening in the layer of 4 spheres, therewith prohibiting the fluid to bypass the packing. The model topology is shown in Figure 8, the gray areas in this figure depict the location of the flow inlet at the bottom and the column exit at the top.

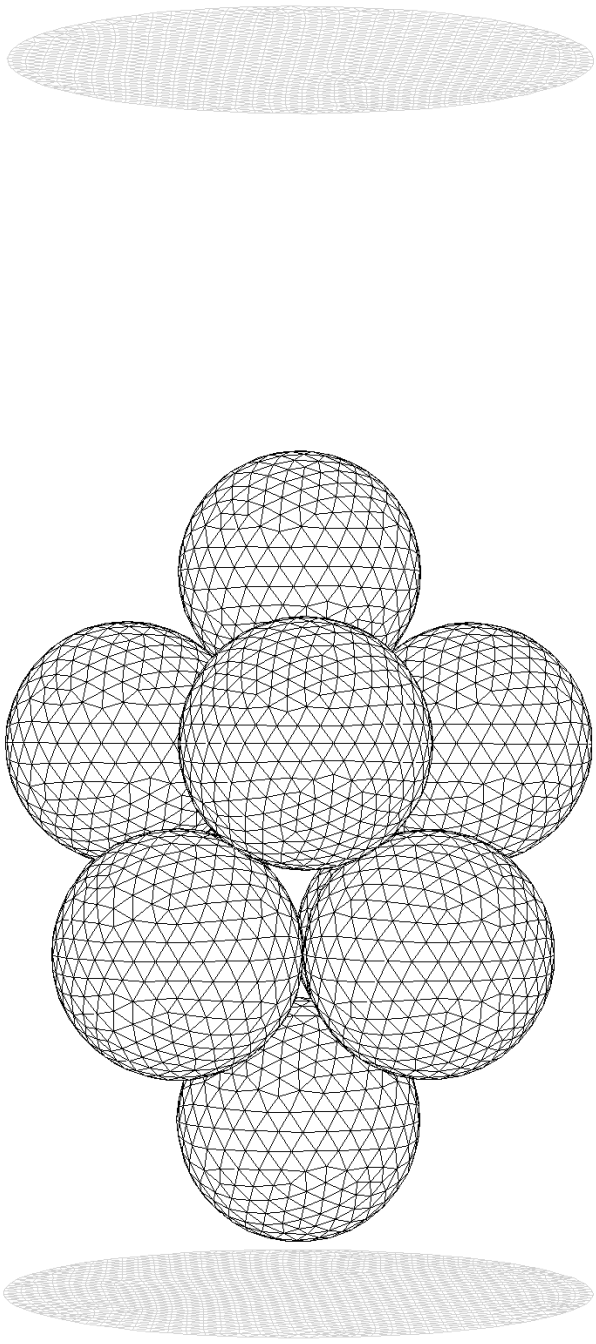

Figure 8. Topology of the 10-sphere mesh as created for the Fluent UNS simulations.

A number of different mesh adaptations were used for modeling with this geometry. The initial mesh, used for the laminar simulations, was used for qualitative comparison with the ANSYS results. The adaptations were created with differing node distributions in an attempt to be able to solve a turbulent problem.

Results from both models were similar yet not identical. The most important difference between the two models was the fact that the ANSYS model simulated contact points with small no-flow zones. At the point where a sphere would touch the wall or another sphere, a small spherical volume was defined with the physical properties of the fluid in which there was no flow. This eliminated convergence problems in fluid cells with very high skewness. In the Fluent UNS model actual contact points were modeled.

Another reason for slightly differing results may be found in the mesh building process, the programs use different processes to create 3D meshes and use an automated mesh generator for the larger part of the process. Since the 3D meshes are different the resulting plots will not be identical. When however the mesh density is large enough the exact distribution of elements should not influence the general final outcome.

The resemblance between the two different simulations was enough to assume a satisfactory comparison and to conclude that both CFD codes will generate the same solution when confronted with the same problem. A velocity vector plot from the Fluent UNS simulation is shown in Figure 9. The flow characteristics near the wall are shown in Figure 9a where the column wall is on the right hand side of the picture. The flow near the center of the bed is shown in Figure 9b. Similar pictures for the ANSYS calculations can be found in Logtenberg et al. (1999) and Logtenberg (1997).

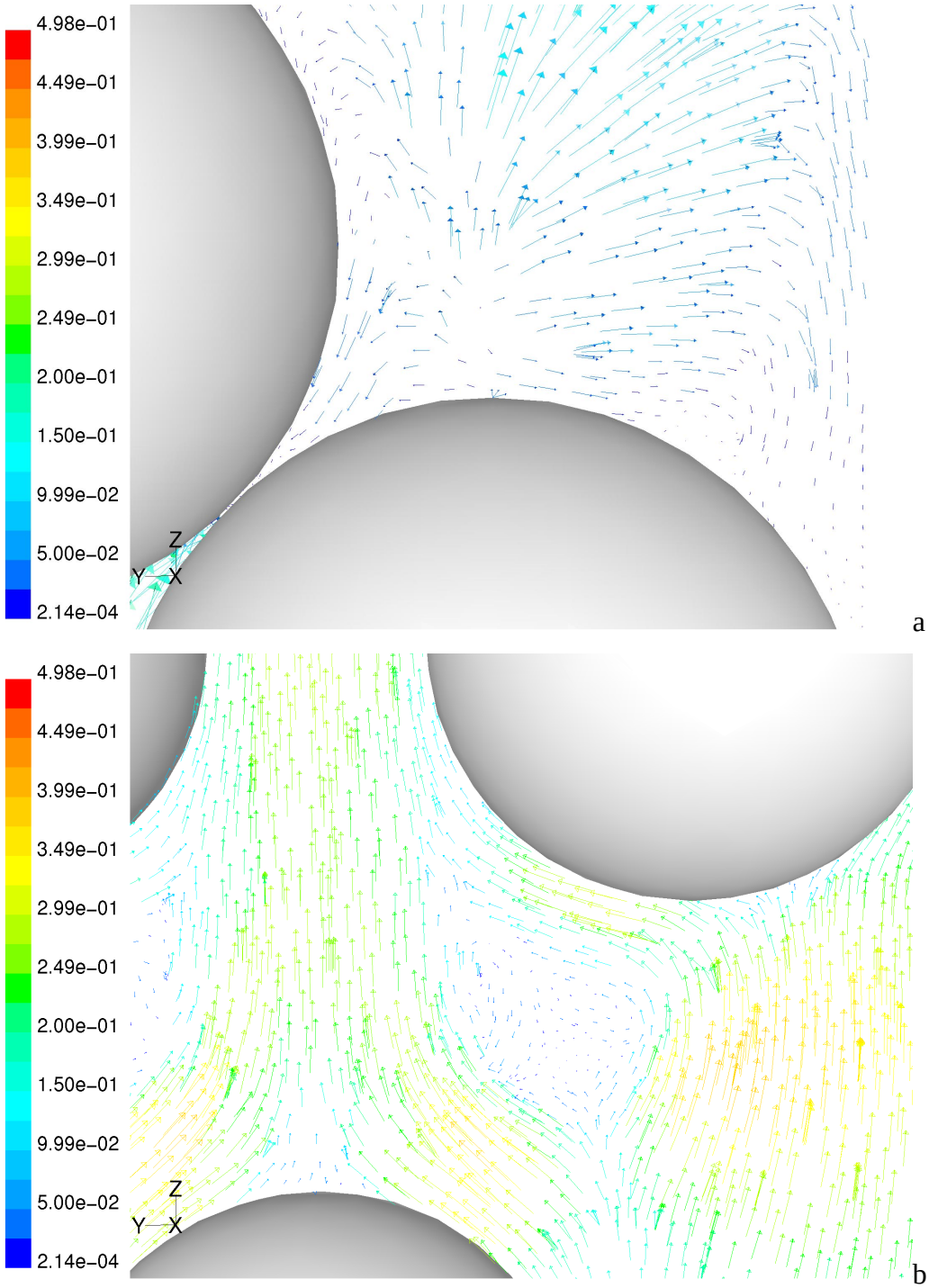

Figure 9. Velocity vector plots for the 10-sphere geometry at Re = 338. The velocity vectors are colored by velocity magnitude (m/s).

3.3 The 44-sphere model

To validate the CFD simulation data for use in more general terms we also wanted to test the results against experimental measurements. For this specific purpose a 44-sphere model with a tube to particle ratio of exactly 2 was designed. This specific model was chosen for a number of reasons.

First the CAD model had to be made identical to an experimental setup so direct comparison of data sets could be made. Therefore the packing of the spheres in the tube had to be predictable. The tube to particle ratio of 2 has a very predictable and repeatable structure and was ideal for our purpose.

An added bonus of this specific geometry lies in the fact that its radial heat transfer Péclet number, Pe_r, has similar values to these of systems with higher tube to particle ratios, $N > 6$. Low N systems usually have a relatively large Péclet number. As the Péclet number is the ratio of (RePr) to k_r/k_f, a high Péclet number is a sign of fluid bypassing, resulting in lower k_r/k_f. Low-N systems tend to form regular packing arrangements allowing for large gaps in the packing to appear. The specific $N = 2$ system also has a regular packing structure but the bypassing area is reduced to a minimum, also the layers of spheres are separated enough for the flow to get incorporated in the packing. Behavior of the sphere packing in low-N sphere packed beds is regular; in the specific cases of $N = 2$ and $N = 3$ the packing is arranged in such a way that most ‘holes’ in the packing are blocked resulting in relatively low Pe_r (Dixon, 1997).

So the twofold advantage, highly structured geometry and heat transfer properties of industrially realistic systems, make this system the ideal choice.

3.3.1 Model Development

The creation of this model has undergone a number of stages. All of the stages of this model were based upon the physical measurements of the original model, which was an identical copy of the experimental setup used in the experimental portion of this project.

3.3.1.1 Original Model

The CAD design of the original 44-sphere model was done in inches to facilitate direct usage of the physical parameters. The tube length was slightly larger at the bottom of the column to mimic a distributor effect. A distributor is present in the experimental setup, in the CFD model a flat inlet velocity profile was defined at the column entrance. The sphere locations were mathematically determined using simple geometric relations.

The surface mesh was created using a bottom up technique where first critical nodes were established from which all edges and faces were created. Critical nodes in this model are the contact points between spheres and the contact points between the spheres and the wall. All the wall-sphere contact points were defined; sphere-sphere contact points were only defined within one layer of two spheres at a common axial coordinate. The surfaces of the spheres were defined using four faces sharing common nodes in the contact points and common edges along the circumference and equator of the sphere. The sphere-wall-contact-point nodes were also shared by the faces that made up the wall structure.

The tube wall was also created with the bottom up technique using the defined sphere-wall-contact-point nodes. The wall was built up from wall pieces stretched between these nodes.

Initially the surface mesh density was defined with a uniform node distribution over all edges. This resulted in problems with 3D mesh creation as well as irresolvable problems with convergence in the simulations. These problems were resolved by refining the surface mesh around the contact points.

The important aspects of this original model are the division of the tube-wall in two sections, a calming section that is not heated and a heating section that is heated, and the incorporation of common nodes between touching wall segments.

3.3.1.2 Calming Section Heating Modeling

When the calming section is modeled with the mathematical accuracy of a CFD simulation it can be perfectly insulated from the attached heated wall section. In the experimental setup this insulation is not perfect and the wall in the calming section is slightly heated through conduction. To be able to make a direct comparison between physical experiments and CFD simulations this conduction had to be modeled.

Initially it was tried to program a User Defined Function using the ambient temperature of the entering fluid and the maximum temperature of the heated wall to describe an axial temperature profile along the calming section wall. This profile would be modeled after a mathematical fit to experimental data to describe the temperature profile from the experimental section exactly.

The User Defined Function option in the specific version of Fluent UNS used for this project, 4.2.8, turned out to be flawed and could not be used. To be able to model the conduction into the calming section another solution had to be created. Since the tube-wall in the model was already built up from small wall pieces, these pieces were individualized in the surface-meshing program. This process allowed different boundary conditions to be set for each wall segment. With the calming section wall now divided in 5 axial sections a rough model for wall conduction could be constructed which improved the accuracy of the simulation results dramatically.

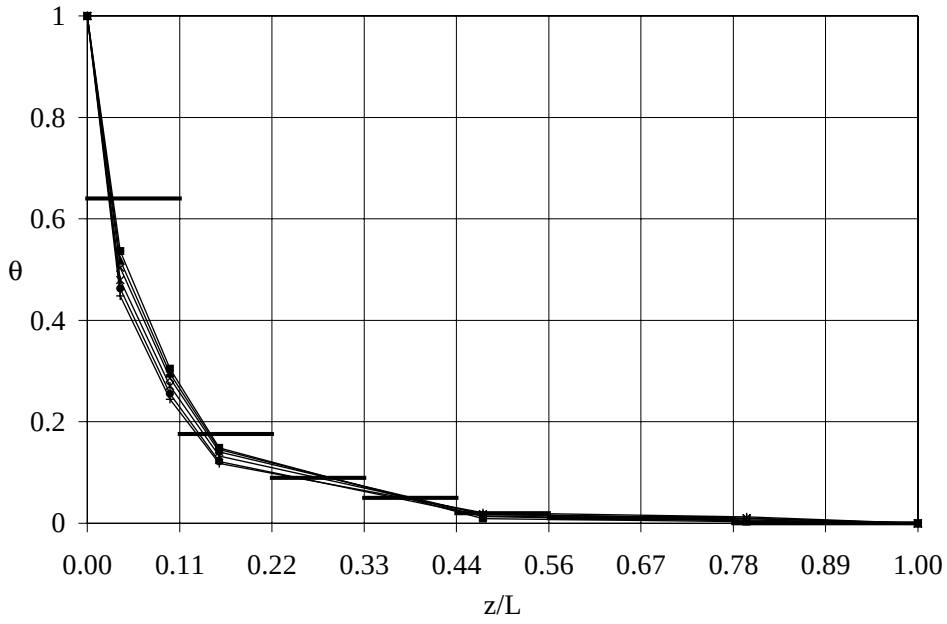

Figure 10. Measured temperature profiles on the calming section wall at several Reynolds numbers and the step function imposed on the 9 calming section wall segments.

In the final model where the contact points were modeled differently the calming section had to be remodeled as well. Since it was still not possible to use the User Defined Function the calming section was divided in axial sections. In this model there were 9 sections to facilitate a more accurate modeling of the temperature profile, see Figure 10.

3.3.1.3 Redesigned contact points

Besides the temperature profile in the calming section there was another problem with the original model. As the contact points between touching objects were modeled with common nodes on walls of different entities, the fluid elements around these contact points were using two nodes on either wall to define their volume. When these fluid elements were created they turned out very skewed, meaning that some of their surfaces were much larger than others within the one tetrahedron.

This skewed mesh around the contact points did not seem to create any problems in creating laminar solutions, but when a turbulent model was used to simulate the specific case convergence was unachievable. It turned out that the flow velocities especially in the fluid elements around the contact points were increasing dramatically, a very typical result for cells that are too skewed. In CFD it is generally accepted that turbulent models are less stable due to the introduction of additional aspects as Reynolds stresses.

To be able to do CFD simulations at higher Reynolds numbers, which would require using a turbulent model, the model had to be fundamentally changed. The fluid elements around the contact points needed to be less skewed, which can only be accomplished by creating a gap between the different entities in the geometry. This gap had to be designed carefully. Too small a gap would not solve the original problem. Too large a gap would drastically influence the flow patterns in the system and therewith the heat transfer mechanism. A considerable part of the heat transfer into the bed is facilitated by a low velocity (stagnant fluid) area around the contact points. This area allows the bed internals to warm up which in turn provide additional heating of the fluid.

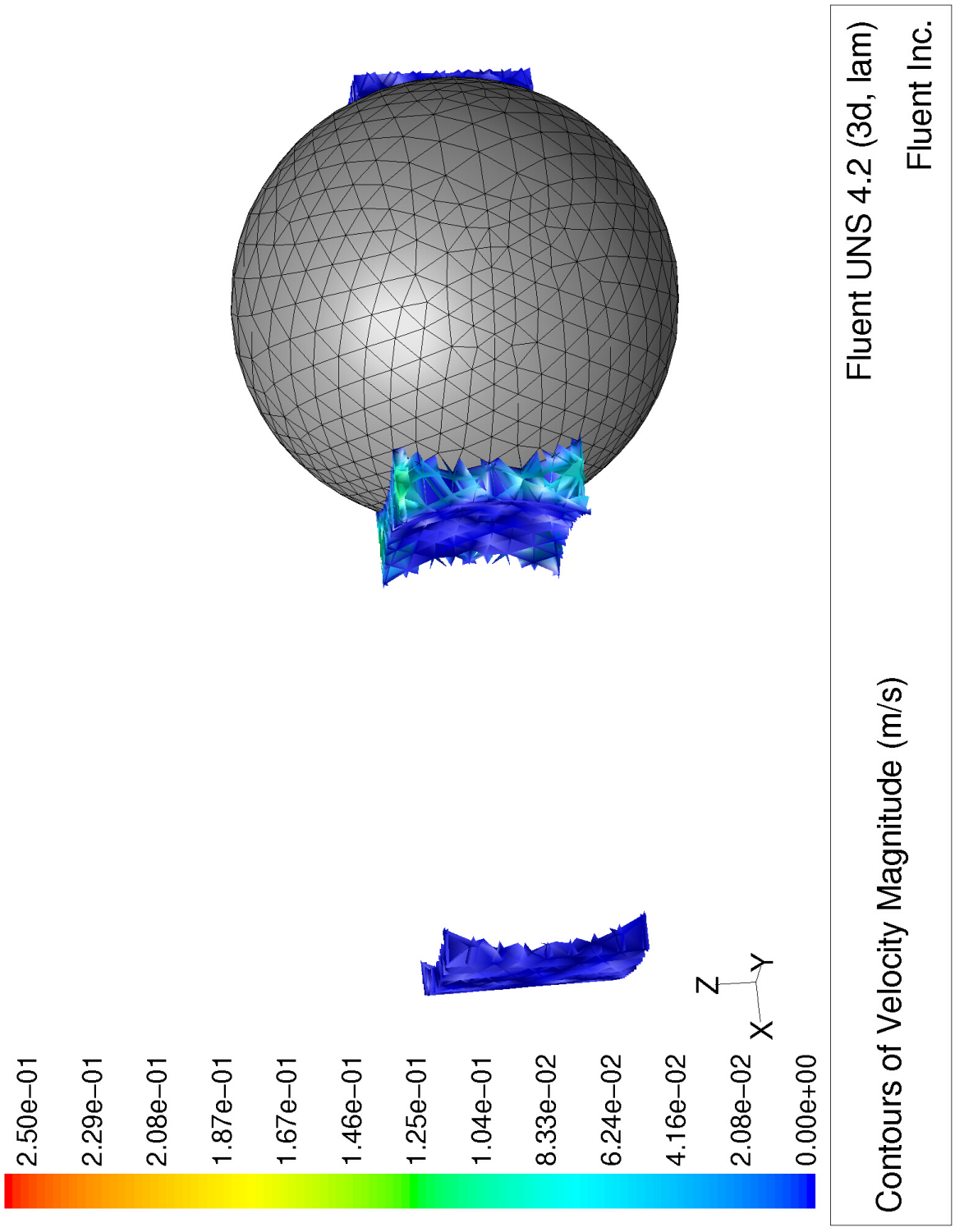

Figure 11. Selected elements around the sphere contact points for mesh comparison.

To design the optimal gap size a number of different models were created with a limited number, and differing sizes of spheres allowing for different gap sizes. The maximal sphere size that would allow for a turbulent model to be solved turned out to be 99.5% of the original sphere size. Other models were created with sphere sizes of 99%, 97% and 95%. These models were compared using velocity distribution histograms of fluid elements near the contact points. The fluid elements for comparison were selected by limiting the fluid zone to an area 0.5 cm in z and y direction from the contact point along the entire x-axis of the column (Figure 11). In the 5 different geometries air was flowed through the bed at a Reynolds number of about 20. Velocity magnitude data was taken from the different geometries and compared. This comparison allowed us to relate the fluid flow composition in the contact point area of the different geometries.

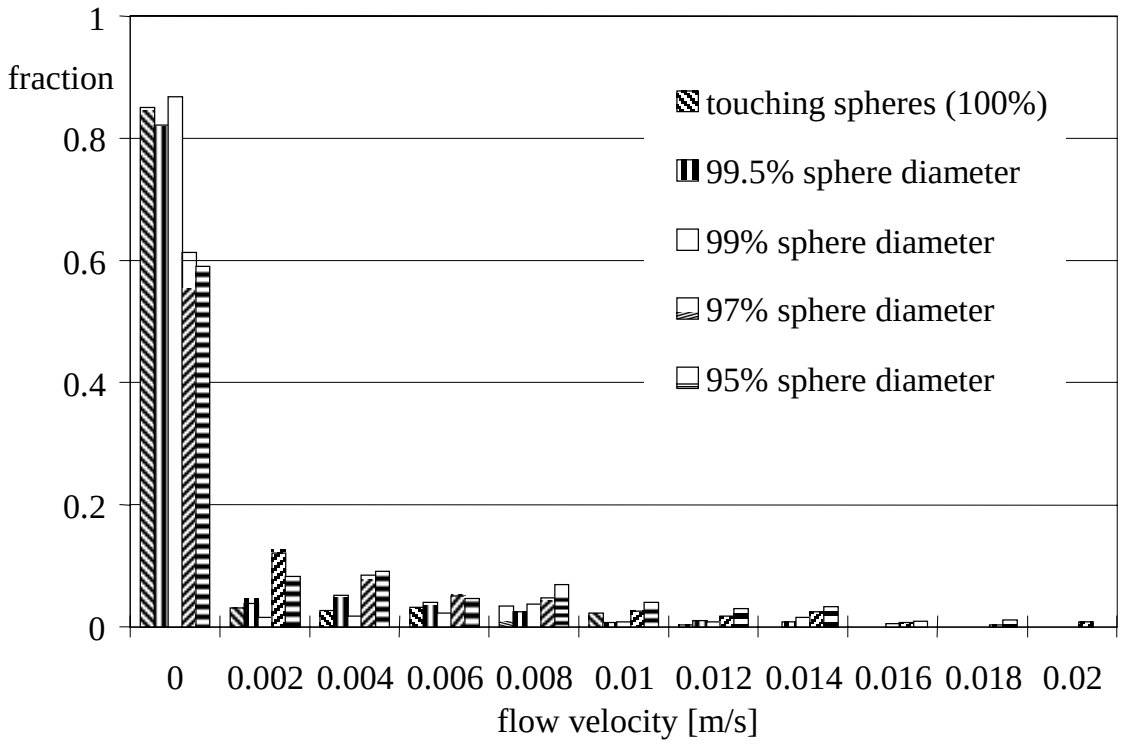

Figure 12. Velocity histograms for comparison of the different gap sizes, v_{in} = 0.01 m/s.

It was shown that when the gaps were larger (the 95% and 97% sphere sizes) the velocity distribution tended to move to higher velocities. Both the 99.5% and 99% sphere size models showed negligible difference from the touching model's velocity distribution (see Figure 12). For further study it was decided to create a full size model with 99% spheres. This was chosen because this model allowed for easier construction and faster convergence than the 99.5% spheres model.

3.3.2 Definitive Model

Eventually all model adaptations were integrated in the final model. In this model the heated calming section was divided in 9 segments on which the temperature distribution was determined empirically. Also it was redesigned to incorporate the small gaps between the spheres to allow for turbulent solution.

The model is shown in Figure 13. In this figure the three views of the model give a better insight into its three dimensional structure. Figure 13a shows a side view along the x axis, giving a clear picture of the build up of the packing. This view clearly shows the structure of the N = 2 packing. Figure 13b is a top view of the model, emphasizing the tube to particle ratio of 2 as well as the structure of this specific packing. Since the structure of the packing is so well defined only two layers of spheres can be identified, the top view also shows how each layer of spheres blocks the bypass created by the previous layer of spheres. Figure 13c is a detail of the 3D mesh showing the detail of the elements in the fluid phase. This figure is similar to the interior mesh shown in Figure 1b. It is different from Figure 2 in that it only shows the 3D mesh in the fluid region. Figure 2 shows a cut along the same plane though the interior mesh of both the fluid region and the spheres, Figure 13 as well as Figure 1b do not show the 3D mesh inside the solid particles.

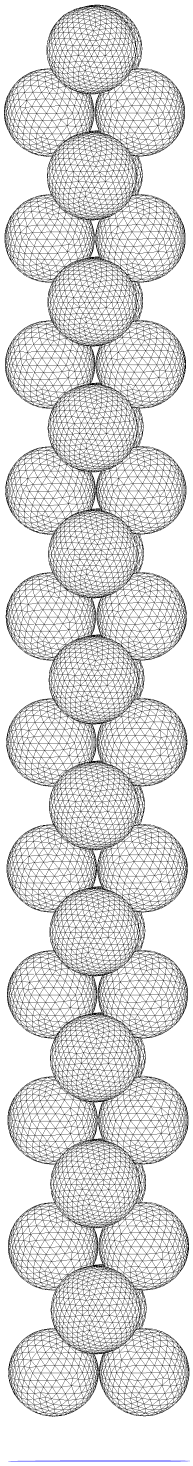

a

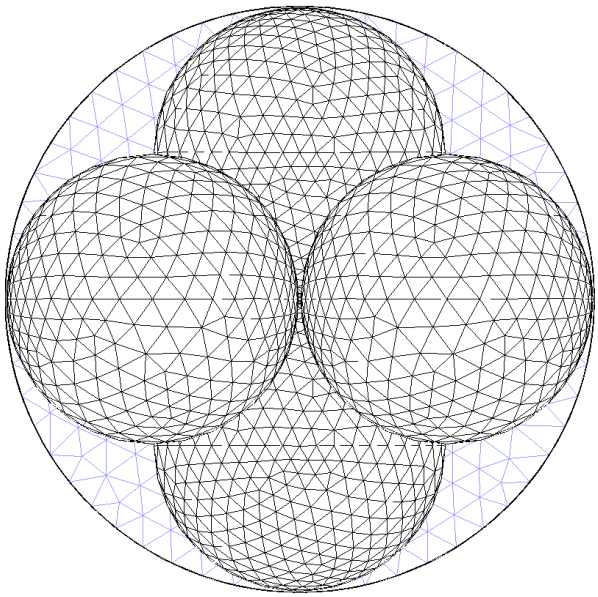

b

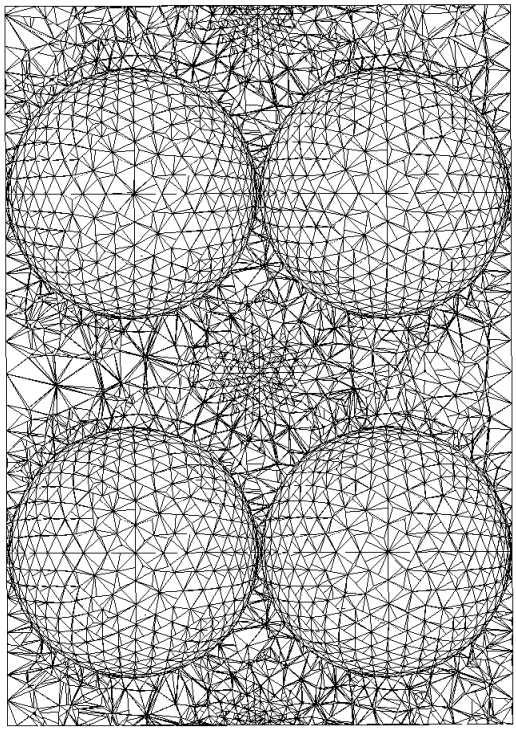

c

Figure 13. CFD 44-sphere model used for validation purposes.

3.3.3 Simulations

For the simulations with the 44-sphere model the boundary conditions were set equal to the boundary conditions for the physical experiments. The inlet velocity of the column was determined through the Reynolds numbers calculated for the measurements. The outlet pressure of the CFD model was set to atmospheric pressure, as is the case in the experimental setup, which has an open-end tube. The wall temperature was set to 383 K, the inlet temperature of the air was set to 298 K, which were approximations of the average temperatures in the experimental setup.

A new material had to be defined for the Nylon spheres. Several specifications for the specific material were found in different sources (Mark, 1978, Kirk & Othmer Encyclopedia of Chemical Technology; Mark 1985, Encyclopedia of Polymer Science and Engineering). Eventually values were taken from work done earlier with these specific materials. A polymer was created with a density of 1300 kg/m^3, a heat capacity of 1000 J/kg·K and a heat transfer coefficient of 0.242 W/m·K (Melanson, 1985).

3.3.3.1 Solution model settings

A number of these solution model settings are very logical, such as the use of a three-dimensional model and inclusion of heat transfer. But all these are options that can be either turned off or on depending on the simulation detail desired. Sometimes it is desirable to not solve an entire model, for time issues or convergence problems. All our runs were performed with three-dimensional models and included heat transfer.

Other aspects of the model that can be chosen are of large influence on the specific balances that are to be solved. The simulation can be either laminar or turbulent, this model aspect requires a few more settings to be taken care of, such as turbulent model parameters. For the specific turbulent runs a standard κ-ε model was used, as described in Chapter 2, with initial guesses of both κ and ε of 1, the default value.

Finally the underrelaxation factors and the residual cut-off values are set. Underrelaxation factors were set slightly below their default values to ensure stable convergence. Residual values were kept at their default values, $1 \cdot 10^{-6}$ for the energy residual, $1 \cdot 10^{-3}$ for all others, continuity, velocities and turbulence factors. The residual cut-off value for the energy balance is lower because it tends to be less stable than the other balances; the lower residual cut-off ensures that the energy solution has the same accuracy as the other values. The velocity inlet values were used as an initial guess for the entire fluid.

3.3.3.1.1 Solution accuracy

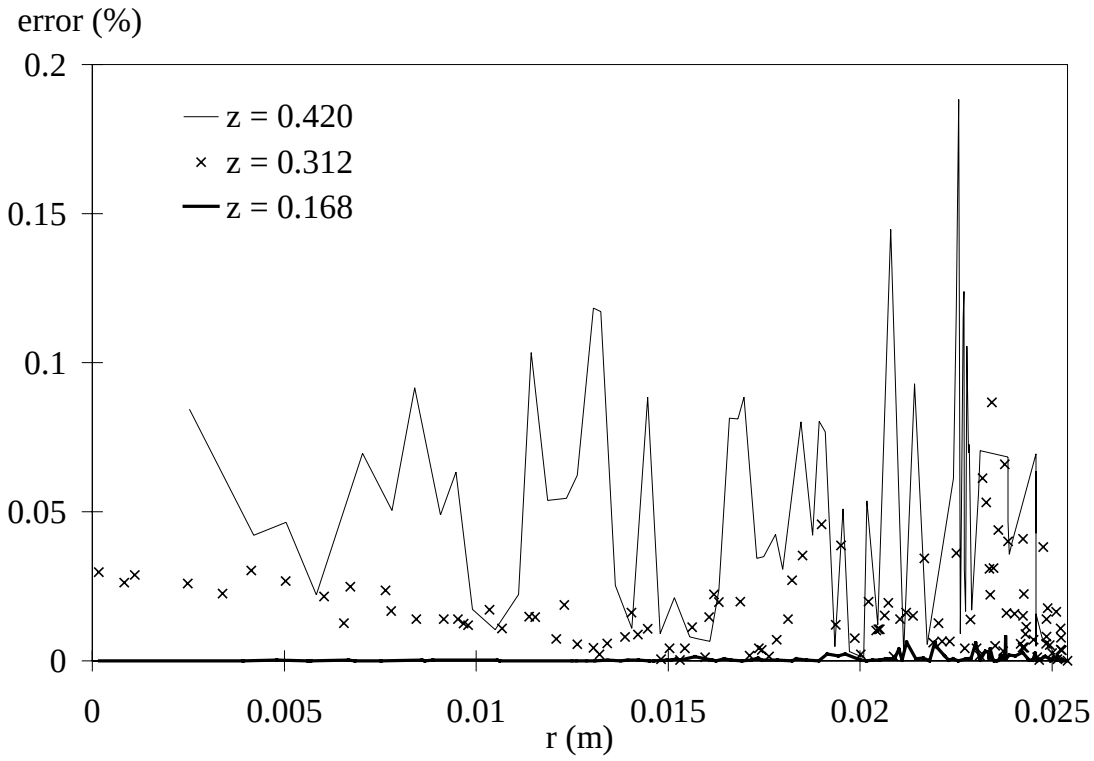

Figure 14. Percentile difference between default solution and round-off solution at Re = 1477.

When default settings for residual cut-off values are used it is important to verify if these settings allow the iteration process to reach an accurate enough answer. As was discussed in paragraph 2.3.3.2 the iteration process will, when allowed, continue to eventually reach a 'round-off' value. When we compare the results from two runs, one using default residual cut-off values and one which is allowed to reach the round-off value, the maximum difference between the two results is about 0.22% with an average difference of approximately 0.05%. In Figure 14 the difference percentage for a number of radial temperature profiles is plotted.

3.3.3.2 Boundary conditions

With all materials and models defined the boundary conditions were set. Only a few boundary conditions are required. The inlet velocity needs to be determined as does the outlet pressure and the wall temperature.

The outlet pressure was set at atmospheric pressure. In the experimental setup the air outlet of the column is open to the atmosphere. The wall temperature of the heated section was set at 383 K, which was the average measured temperature for the tube wall. The wall temperature profile on the calming section was determined by averaging experimentally acquired temperature data of the calming section wall over the 9 separately modeled wall sections. The temperature was then implemented as a step function on the 9 wall segments, see Figure 10. The air inlet temperature was set at room temperature, 298 K. The inlet velocity for each run was determined by the Reynolds number of the specific experimental run, through the definition for the Reynolds number. The other constants in this calculation were the density of air, 1.225 kg/m^3, the viscosity of air, $1.7894 \cdot 10^{-5}$ kg/ms and the particle diameter, $2.54 \cdot 10^{-2}$ m. Density and viscosity of air and therewith the Reynolds numbers were evaluated at the inlet conditions, 298 K and 1 atmosphere.

The initial state of all fluid elements was set to the conditions at the air inlet. Wall temperatures were constant at the mentioned boundary condition values.

3.4 Post Processing

Once a simulation has been satisfactorily completed it is necessary to obtain the desired information from the flood of data. The mesh for the final model contains over 400,000 elements. For all the fluid elements there is a wealth of data available, fluid temperature, pressure, density, viscosity, turbulence properties as the turbulent kinetic energy, the turbulent kinetic energy rate of dissipation and Reynolds stresses, x, y and z components of fluid flow velocity and a number of derived units such as vorticity and helicity. For the elements in the solid regions of the model (inside the packing) the amount of data is considerably reduced by the fact that there is no flow.

To be able to do a direct comparison of the CFD results with experimental data the data from the simulations needs to be in the same format as the experimental data, radial temperature profiles.

3.4.1 Creating data sets

To be able to export the radial temperature profiles from the CFD simulation, data sets had to be created. First an ‘Iso-Surface’ is created, this is a surface defined as a plane with one constant aspect, in our case this was a constant axial position. In this surface all elements are included that intersect this specific axial position. When the axial planes intersect part of the solid bed some elements have to be excluded, since we are only interested in the fluid temperatures.

The Iso-Clip operation is used to exclude the elements that are part of the sphere packing. The axial plane is selected and limited to one specific zone index. Zone indexes determine the element type, whether it is fluid or packing.

3.4.2 Exporting data

With the Iso-surfaces created we can now reduce the data to one axial plane, as we did with the experimental setup, where a radial temperature profile is collected at a specific axial position, see Chapter 4.

The radial profiles are exported as two-dimensional plots of the fluid temperature versus the radial position. The X-Y plot option in Fluent allows the user to define variables along the x and y axes of a plot as well as the domain from which the data had to be taken. By using the Iso-surfaces created earlier as a domain for creating the X-Y plot and using the temperature and radial coordinate for the variables the wanted data sets are created.

A number of data sets are plotted, temperature versus radial coordinate and then exported as text files. These text files are imported in a spreadsheet program (Excel) where they are combined with their respective experimental counterpart. In the spreadsheet the different data sets are made dimensionless for easier comparison. The graphs created are used in the comparison graphs as presented in Chapter 5.

Other ways of data export from Fluent include more visually or qualitative views of temperature distribution or flow profile. These types of data visualization are mostly used for qualitative analysis of heat and mass transfer principles.

A velocity vector plot is created by reducing the model to a two dimensional plane. This limits the data displayed to one plane so the data that needs to be shown is not obscured by elements in front of the plane of view. The resulting data set consists of all the elements that intersect the defined plane. Velocity vectors are displayed at the center of the projection of each element on the defined plane that is included in the data set. The vectors that are displayed are also projections of the three dimensional vectors of the fluid flow in each element. The three dimensional nature of the vectors can be seen by managing the plot in the program, this effect is lost however in the two dimensional display of the plot. The most important aspect of the velocity vector plots is that we are able to show flow characteristics in the bed, see Figure 15.

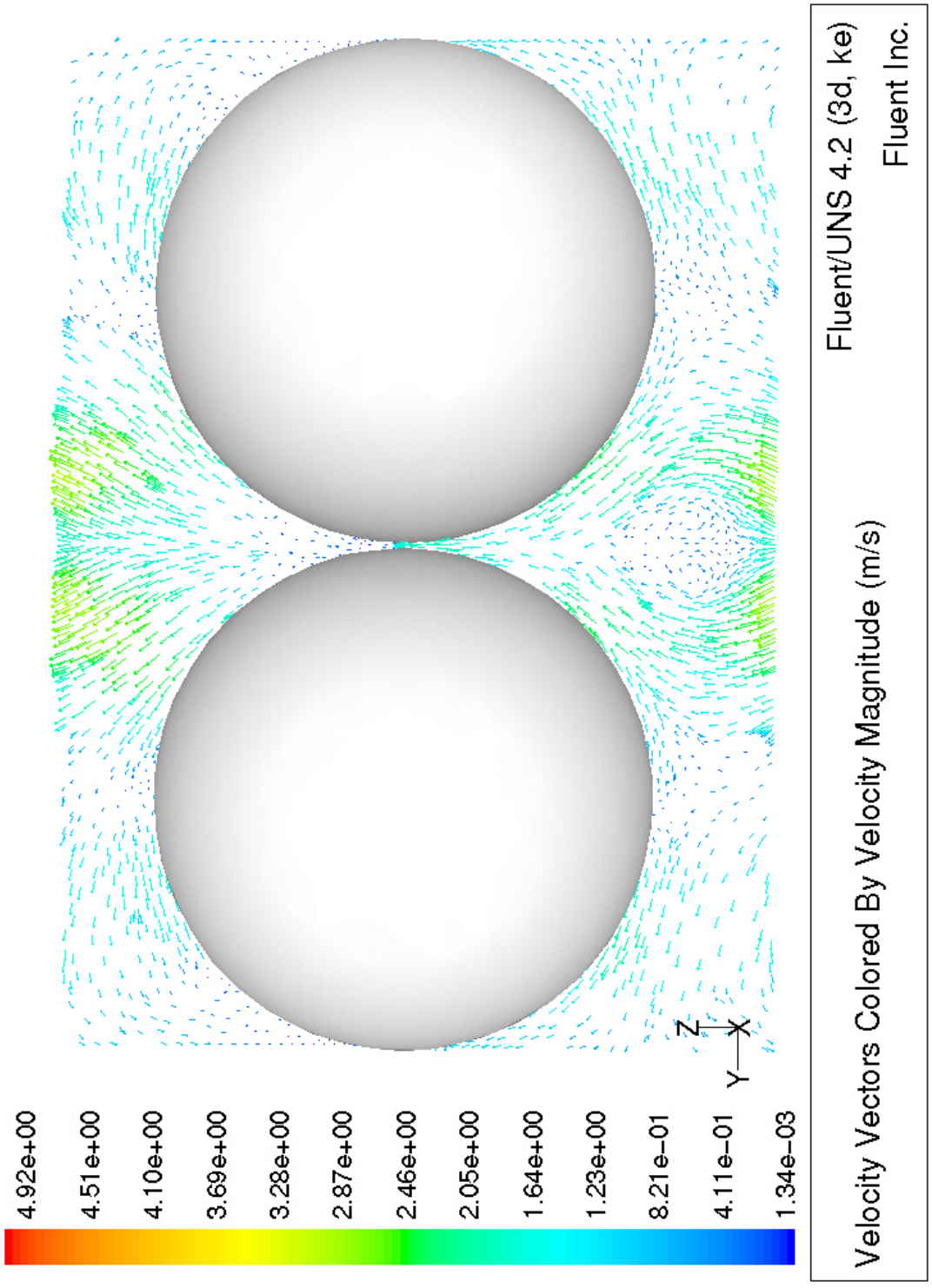

Figure 15. Velocity vector plot for a 2 layer section over the entire bed diameter in the x = 0 plane at Re = 1922, legend shows velocity in m/s.

When we take a closer look at these velocity vector profiles they will give us specific information about flow behavior near the contact points or in between layers of spheres in the bed. The contact point between two spheres in one layer of the packing, just below the spheres we can see in the top part of the picture, is located near the bottom of the picture and can be identified by a small circle in Figure 16. When we look closely at the flow profile near a sphere-sphere contact point we can identify two important flow aspects. First we see small eddies forming just downstream from the contact point (overall flow in these pictures is from the bottom to the top). The eddies are formed in the wake of the contact point. This is one of the few areas in the closely packed bed where there is enough room for eddies to form. Secondly the flow magnitude in the contact point area is very low due to the close proximity to the solid particles; this aspect is what facilitates the modeling of heat transfer near the wall-sphere contact points. The flow in the small spaces is very slow, almost stagnant; this facilitates conduction from the hot wall through the stagnant fluid to the bed. Both these aspects are intuitive but are hard to show experimentally.

When we now look at the same plane but in a bed void instead of close to the packing, Figure 17, we can see that there is a considerable amount of radial flow. Figure 17 ranges from the center of the column at the left hand side of the picture to the wall at the right hand side of the picture. Radial flow causes convective heat transfer within the bed increasing the overall heat transfer. The convective heat transfer is accomplished through transport of fluid from the center of the bed into an imaginary layer close to the wall, where most of the heat transfer takes place due to the strong temperature difference between the wall and the fluid, and the transport from this layer to the center of the bed. Another aspect shown in Figure 17 is the downward flow along the wall; this back mixing also increases the total heat transfer. This last aspect of downward flow along the wall has also been shown in studies done with Magnetic Resonance Imaging in packed beds (Kutsovsky et al., 1996).

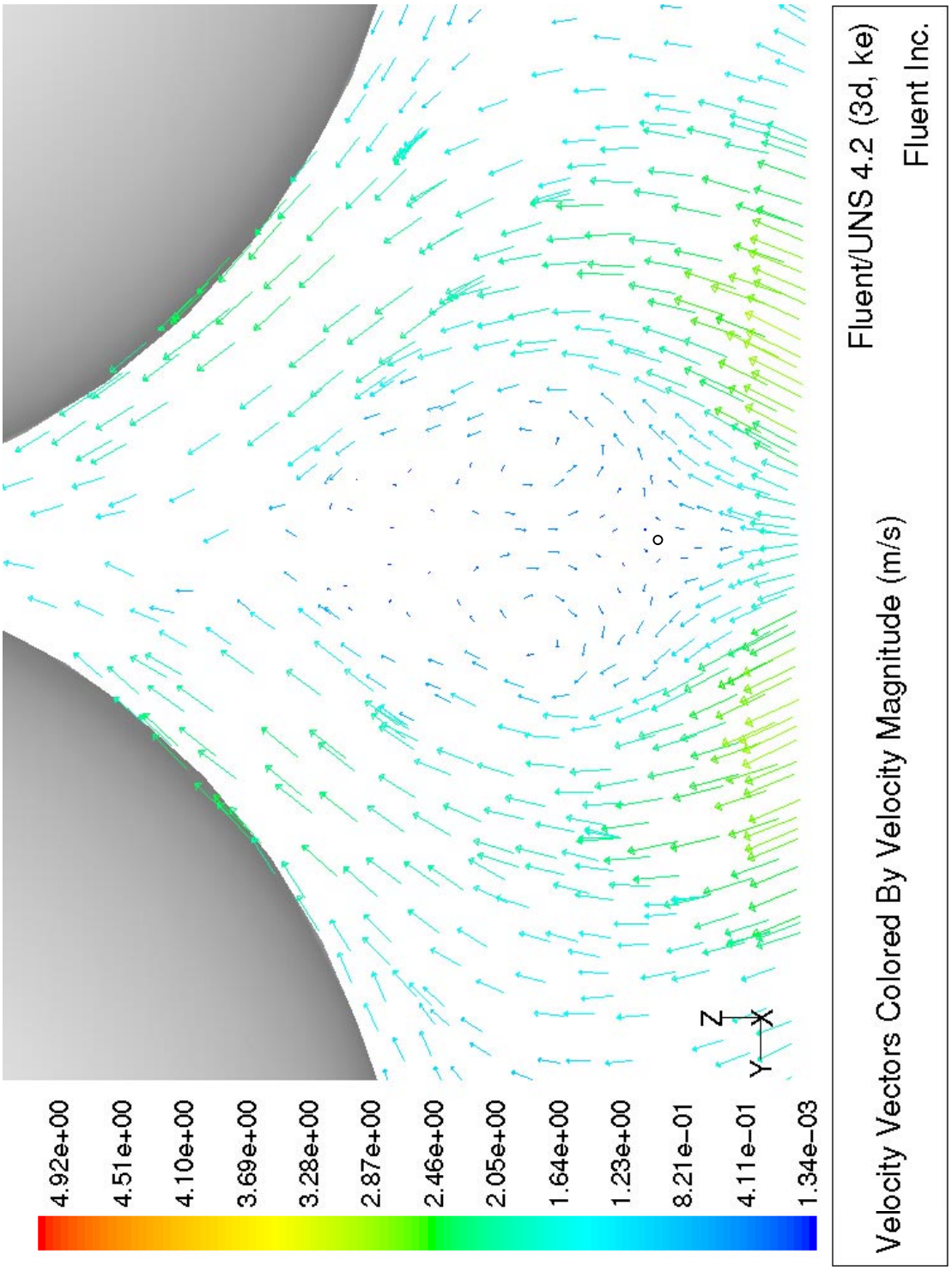

Figure 16. Velocity vector profile at a sphere-sphere contact point, in the x = 0 plane at Re = 1922, legend shows velocity in m/s.

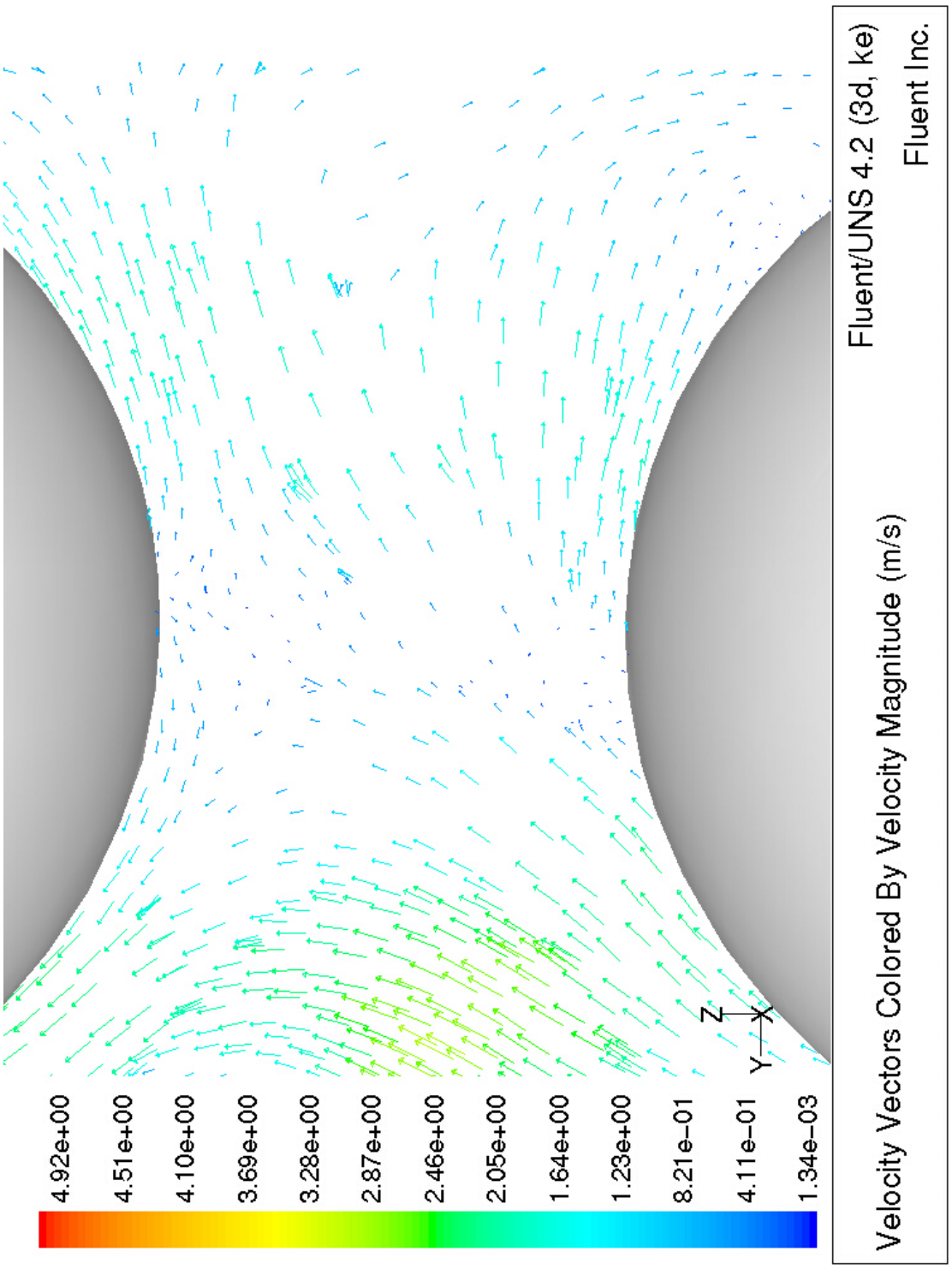

Figure 17. Velocity vector plot in x = 0 plane between two sphere layers at Re = 1922, legend shows velocity in m/s.

4. Experimental Methods

To be able to use CFD results such as velocity distributions and temperature profiles in modeling specific and general fluid flows the CFD results produced need to be validated against experimental results. When we show that for a specific type of geometry CFD results and experimental results agree we can then use the CFD results as data in the general modeling of these geometries. The CFD model that was used was based on an experimental setup available in the laboratory. A series of experiments were conducted in this setup. The collected data was then compared with the CFD results.

4.1 Experimental Setup

The experimental setup used is a single tube, heated wall, packed bed setup as is shown in Figure 18. The packed bed consisted of 44 nylon-66 spheres with a diameter of one inch. The column (single tube) in which they were packed has an inner diameter of two inches. The column consists of two main parts. The bottom part is a nylon tube, 6 inches in length that was not directly heated; this part is referred to as the calming section. In the calming section a steady flow profile in the bed was established. The second part of the column is directly downstream from the calming section, the heated section. The double copper walls in the heated section were heated with steam flowing in between the double wall and were maintained at a constant temperature, heating the airflow inside the column. The 44-sphere packed bed fills the entire calming section and part of the heated section leaving room after the packing for installation of a thermocouple cross for measuring gas temperatures above the bed. The wall of the column is fitted with a number of thermocouples to verify the constant heated wall temperature as well as to establish the axial temperature profile in the calming section. In the double wall of the heated section thermocouples were located at axial positions, 76.2, 228.6 and 381 mm from the calming section heated section interface. In the calming

section wall thermocouples were installed in drilled holes at axial positions, -6.35, -15.9, -25.4, -76.2 and –127 mm from the section interface. All thermocouples were K type thermocouples.

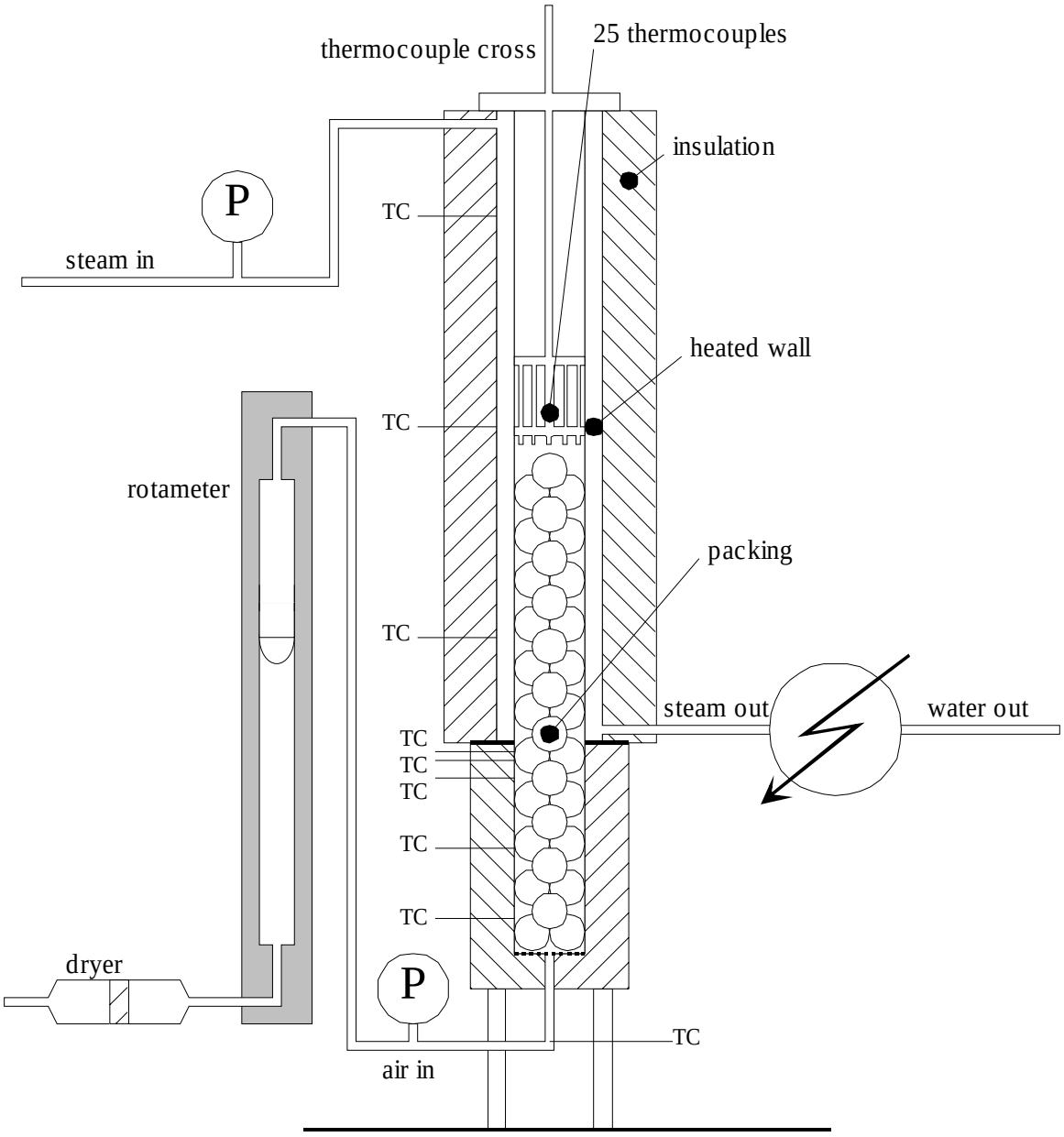

Figure 18. The experimental setup used for the collection of temperature profiles.

Temperature measurements were taken at a series of particle Reynolds numbers and bed lengths. Besides the axial temperature profile of the column the temperature of the air is also measured at the column inlet. In the air stream a radial temperature profile is measured using a thermocouple-cross, depicted in Figure 19. The thermocouple-cross is inserted in the column approximately 5 mm above the top layer of the bed to measure the radial temperature profile in the gas flow.

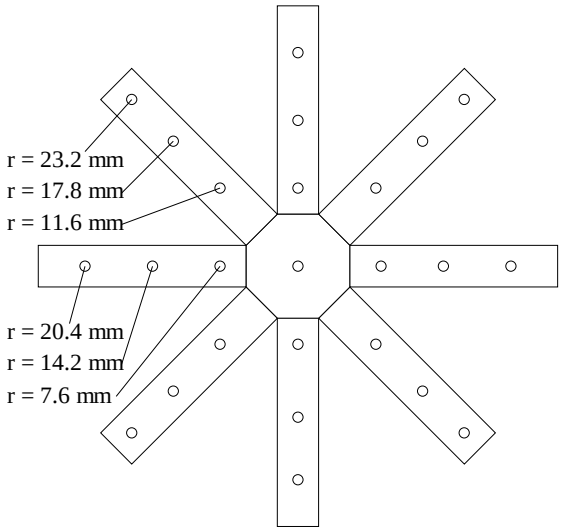

Figure 19. The thermocouple-cross with exact positioning of all 25 thermocouples used for establishing radial temperature profiles in the gas flow.

The steam used for heating the wall of the heated section was drawn from an in-house system, and its quality and pressure were not constant at all times. Most experiments were performed when backpressure of the steam was more than twice the required pressure of 5 psi. The pressurized air that flowed through the column was also drawn from an in-house system. The humidity of the pressurized air depended on external conditions. The humidity of the air influenced the maximum flow velocity since at very humid conditions the sudden expansion of the air within the rotameter caused condensation.

4.2 Experimental Procedure

The experimental procedure for gathering experimental data has been established during previous studies and has also been described in detail (Dixon, 1997). During this project the experimental procedure has not been changed significantly.

A measurement consists of establishing and recording a steady state temperature profile for a combination of a specific bed length, Reynolds number and angle of thermocouple cross. A total of four thermocouple-cross positions are used for measurement. Besides the initial position, measurements are taken at 15, 30 and 45-degree angles from the initial orientation. By rotating the thermocouple cross a good spread of data points covering the entire radial plane is ensured, giving a full picture of the angular spread of the radial temperature profile.

When all four angles have been recorded the Reynolds number is varied by changing the flow velocity of the air through the column. A complete series consists of 15 Reynolds numbers ranging from the lowest possible flow at a particle Reynolds number of 373 to the largest possible flow at a particle Reynolds number of 1922.

Table 1. Overview of all the Reynolds numbers at which experimental measurements were taken.

Reynolds numbers														
373	468	564	664	769	879	986	1097	1221	1346	1477	1624	1724	1833	1922

The upper and lower limits on the Reynolds number range were imposed by the experimental setup. The lower limit at a Reynolds number of 373 was the lowest steady flow that could be established. The upper limit at a Reynolds number of 1922 was the highest flow at which no flooding of the flow controller would occur. The flooding in the flow controller is caused by the moisture contained in the airflow that condenses at sudden expansion.

When measurements have been taken at all four angles and at all 15 Reynolds numbers the setup is shut down temporarily to cool down and adjust the bed length. The

cool down period is required to be able to handle the setup for removal of part of the bed. To be able to take measurements at several bed lengths part of the packing needs to be removed to be able to lower the thermocouple cross further. At the new bed length the entire series of Reynolds numbers with all respective angles are then measured etc. The collection of bed lengths is given in Table 2.

Table 2. Overview of all bed lengths at which experimental measurements were taken.

Bed lengths [m]								
0.420	0.384	0.348	0.312	0.276	0.240	0.204	0.168	0.132

The bed length was adjusted by removing 2 layers of spheres, 4 spheres in total, at a time. The initial bed consisted of 44 spheres resulting in a total bed length of 0.420 m. With each bed length adjustment the total bed length reduced, down to 0.132 m at the shortest bed with 12 spheres. The shortest bed ends 0.028 m before the heated section starts.

Before measurements can be taken it is important that the setup reaches steady state. First the steam supply to the heated wall section is opened and a steady flow of steam is supplied at a pressure of approximately 5 psi. Next the airflow is set to the desired velocity corresponding with the desired Reynolds number and the system is allowed to reach steady state. During this time the temperatures being recorded by the thermocouples in the thermocouple cross are plotted against time. The behavior of the temperature in time indicates whether steady state has been reached. A measurement was taken at steady state, when temperatures did not change for a period of 5 minutes. Usually a ten to fifteen minute time period is enough for the system to reach steady state. This period is longer, approximately 25 to 30 minutes, at start up when the column has to be heated from room temperature.

4.2.1 Data collection

All thermocouples are connected to a computer system for data collection. The thermocouples are connected to two Keithley Mtherm20 thermocouple boards, which read the signals from the thermocouples and connect to a Keithley Metrabus MDB64 interface unit in the computer system where the temperature data is recorded.

A program written in Turbo Pascal 7.0 has been specifically designed for these experiments. The program works specifically with the Keithley Metrabus MDB64 interface card connected to the Keithley Mtherm20 thermocouple boards. The program performs in three separate modes, stabilizing, steady state- and transient measurement. The third option of transient measurement was not used in this work. When operating in the stabilizing mode three graphs are shown, a radial temperature profile, a wall temperature profile and an average radial as well as wall temperature as a function of time. This mode of operation is used to determine whether or not the system has reached steady state. When the plot of temperatures versus time shows a constant value for approximately 5 minutes steady state is reached and a steady state measurement can be taken in the steady state measurement mode. In this mode all temperatures measured at that time are recorded in a file as well as displayed on the screen in a radial temperature profile and a wall temperature profile.

When a steady state measurement is taken the data is stored in a file named by the user. Whenever a new series of measurements is taken a new file can be created by simply defining a new filename. Each file that is created starts with a header, which contains the positions of the thermocouple in the column and in the thermocouple cross, it will also contain specifics of the experiment as defined by the user, the column radius, the particle diameter and the bed length. Additionally the temperatures of all the thermocouples will be added to the file each time a steady state measurement is performed.

The computer data collection setup as well as the data collection program was created by O.R. Derkx and are described in detail in his Thesis (O.R. Derkx, 1995).

4.2.2 Data recovery

When temperature profiles need to be made from the collected data the data files need to be imported in a graphing program. Microsoft Excel was used for reorganizing the data and plotting the radial temperature profiles. The data files as they were collected from the experiments contained 60 separate measurements each containing 34 recorded temperatures, 1 at the air inlet measuring the inlet air temperature, 8 along the column establishing an axial temperature profile and 25 in the thermocouple cross. The data file contained all 4 angular measurements at all 15 Reynolds numbers for a specific bed length. Each time the bed length was altered a new data file was created. The data from each file was reorganized to form a single graph for each combination of Reynolds number and bed length, therewith combining the 4 angular measurements and creating a radial profile with 100 data points.

To be able to compare the experimental data with the CFD data all data was plotted using dimensionless positions and temperature. Especially the temperatures needed to be made dimensionless since inlet temperatures in the experimental setup were determined by external conditions. Wall temperatures also may have fluctuated from experiment to experiment depending on the pressure and quality of the steam used.

5. Results and Discussion

5.1 Direct Comparison of Results

For the representation of the data the radial temperature distribution in the tube was chosen. This was chosen as a method of comparing the CFD results with the experimental data since the radial temperature distribution is of importance to bed operation in the chemical industry, it is also dependent on both internal processes that we model, heat transfer and flow profile and finally it is relatively easy to measure in the experimental setup.

5.1.1 Qualitative Features of CFD Results

The data produced by a CFD simulation are numerous but the commercial code allows the user to qualitatively interpret the results of the simulation fairly easily. When quantitative comparison is desired the data need to be exported and reduced. For creation of the specific data sets, see paragraph 3.4.1.

As can be seen in Figure 20 and Figure 21 the amount of data points for a CFD radial profile is large, approximately, 950 data points. The overall radial pattern shows a typical temperature profile for flow through a packed column, a lower temperature near the middle of the column increasing towards the column wall, with a steeper increase (temperature jump) near the wall.

Another aspect of the data is an increasing spread or experimental error towards larger radii. This can be explained by the fact that a radial profile collects data with differing angular coordinates but the same radial coordinates at one radial position. Since there is no angular symmetry data can be collected above a sphere or just above a bed void leading to differing temperatures. The increase in spread is due to the larger number of elements at larger radii resulting in a larger experimental spread.

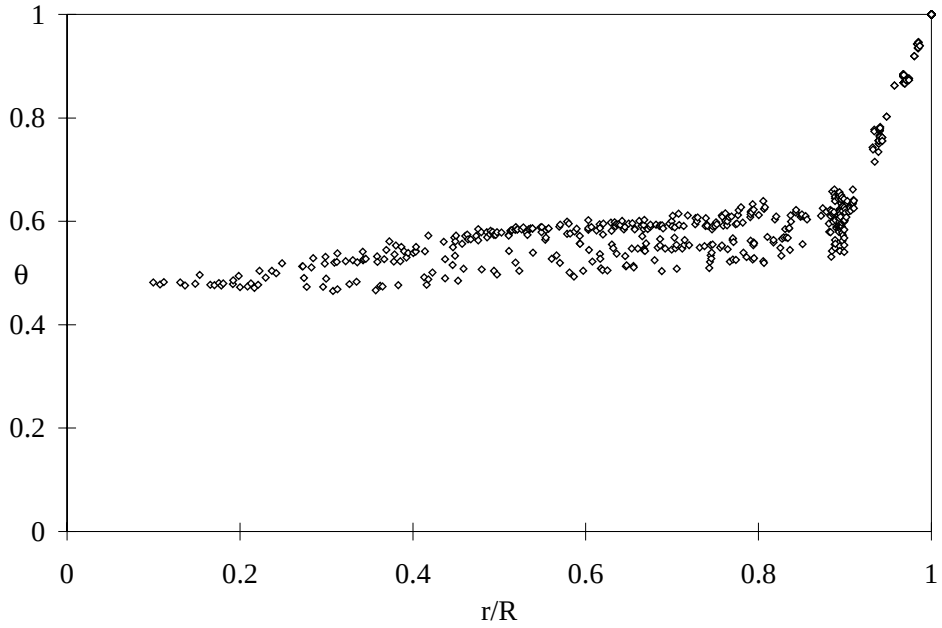

Figure 20. Temperature profile plot of CFD data at Re = 1724, z = 0.420.

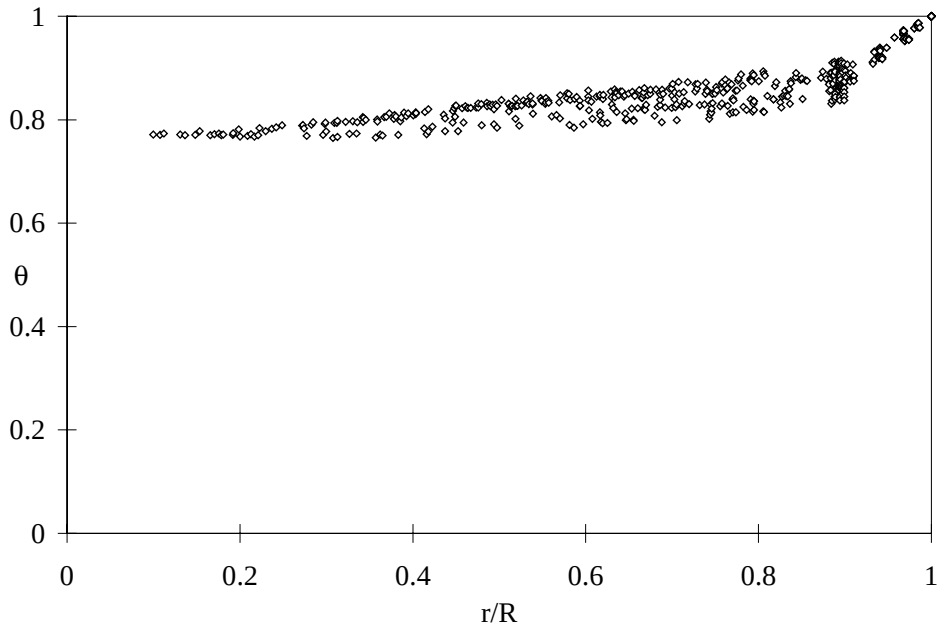

Figure 21. Temperature profile plot of CFD data at Re = 564, z = 0.420.

5.1.2 Qualitative Features of Experimental Results

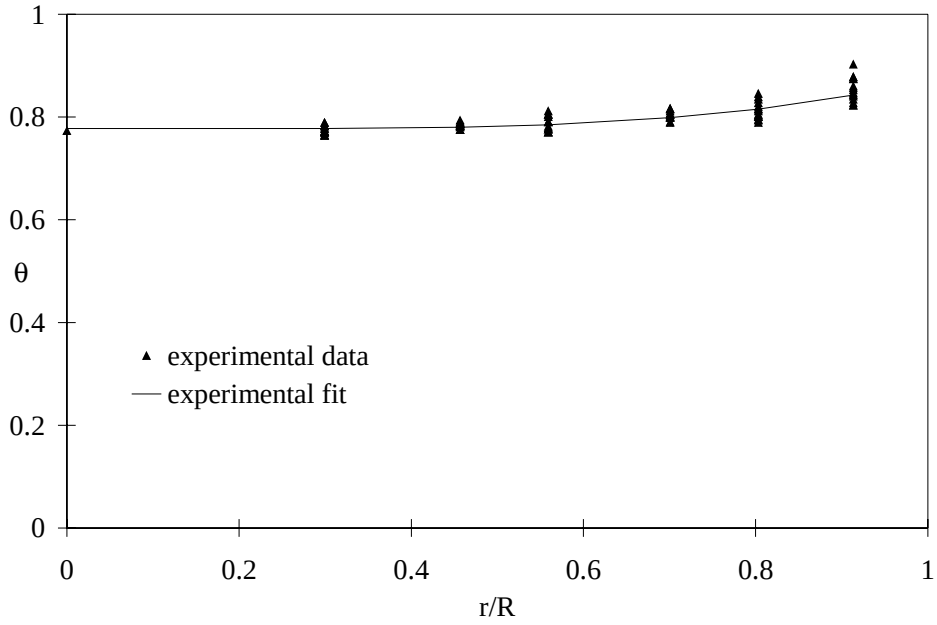

Figure 22. Experimental data with polynomial fit at Re = 879, z = 0.420.

Figure 22 shows an isolated experimental measurement. In this graph it can be clearly seen that experimental data are only collected at a certain number of radial positions, those where the thermocouples are located in the thermocouple cross. This results in a less detailed radial profile than continuous but still gives a good overview of the actual temperature profile. When we plot the CFD data with the experimental data we can see that both profiles show a similar increase in angular spread at larger radii, see Figure 23. In the upcoming graphs where experimental data and CFD data are compared both datasets are plotted in one graph.

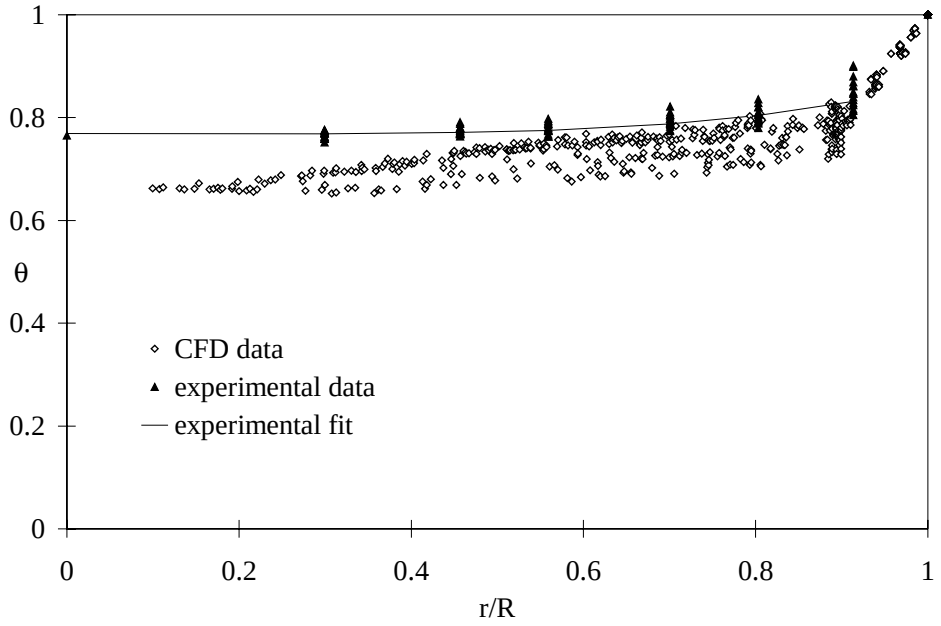

Figure 23. Comparison of angular data spread in CFD data and experimental data. Re = 986, z = 0.420.

5.1.2.1 The effect of overall flow velocity

To find the effect of the overall flow velocity we look at a number of radial temperature profiles from experiments at an axial position of z = 0.240 but at different Reynolds numbers. As the superficial gas velocity, and therewith the Reynolds number, increases the gas phase temperature decreases. At the lowest Reynolds number of 373, the superficial gas velocity or inlet velocity is only 0.216 m/s. At the highest Reynolds number of 1922 the superficial gas velocity is 1.116 m/s.

From Figure 24 we see that when the Reynolds number increases the overall temperature profile is lower. This is an expected feature, as the fluid flow velocity is increased the residence time is decreased therefore the exposure to the heated wall is decreased. With decreased exposure to the hot surface the fluid will have a lower resulting temperature.

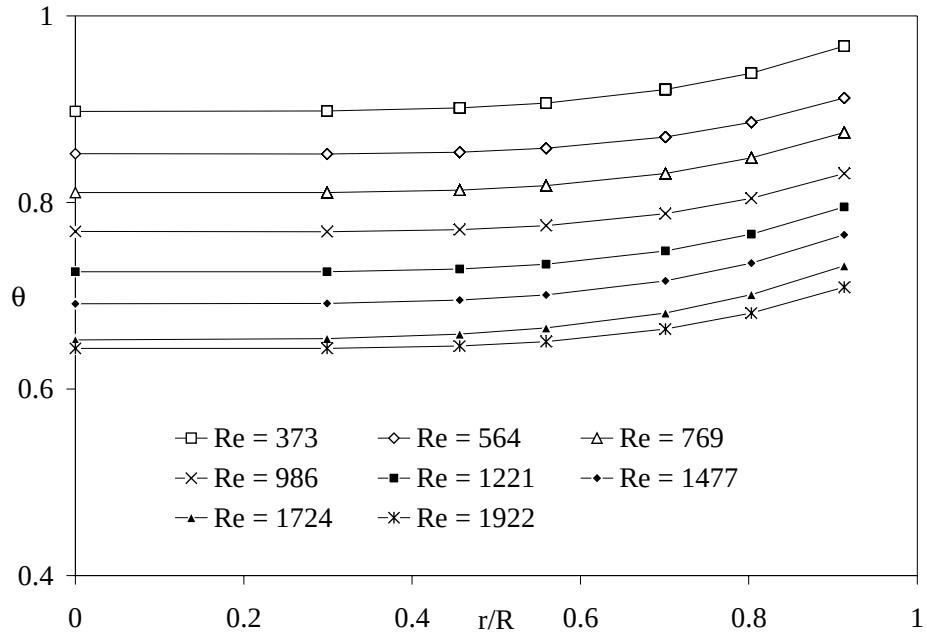

Figure 24. Influence of flow velocity on temperature profile for experimental data at z = 0.240 for average values of experimental measurements.

Also as the fluid flow increases the difference in overall temperature between the different measurements decreases. As the residence time decreases the difference in effective heat transfer will decrease asymptotically, reaching zero at infinite flow velocities, resulting in smaller differences in the overall temperature.

5.1.2.2 The effect of axial position

In Figure 25 the experimental fits for the entire range of bed depths in the heated section are plotted. It is obvious that the temperature profile increases as the axial coordinate increases. A higher axial coordinate denotes a position further downstream in the bed; since the residence time is larger, the overall temperature is higher.

Another aspect that becomes clearer from looking at temperature profiles at different bed depths than it does from a series at different Reynolds numbers is the change in

profile shape. As the fluid enters the heated section there is a large difference between the temperature at the center of the column, which is at the inlet temperature, and the temperature at the wall, which is closer to the wall temperature. As the fluid progresses through the column it warms up with the fluid close to the wall getting at the wall temperature and the difference between the center region temperature and wall region temperature decreasing. So as we get further downstream in the bed the entire profile is higher and flatter.

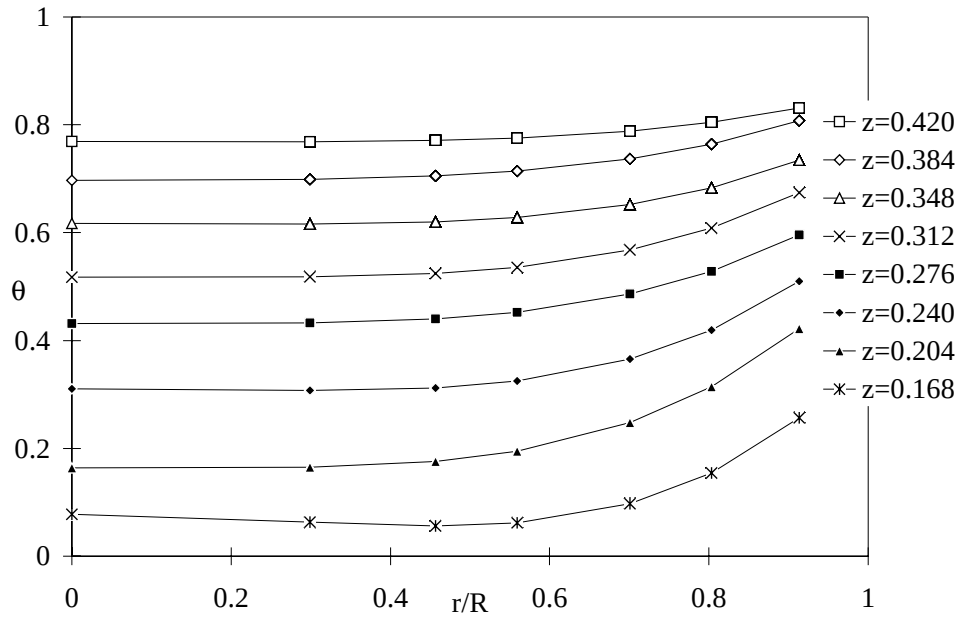

Figure 25. Influence of bed depth on temperature profile for experimental data at Re = 986.

5.1.3 Comparison of CFD Results to Experimental Data

When the CFD results and the experimental data for the same conditions are plotted dimensionless axes are used. In this way, small temperature differences in inlet temperature and wall temperature in the experiments can be compensated for.

In this section comparisons are made between radial temperature profiles at several different Reynolds numbers. Initially, comparisons were made between experimental radial temperature profiles and CFD radial profiles at different axial positions in the packed bed. Most of these comparisons had to be eliminated because of fundamental differences in data acquisition technique between the experimental and CFD cases. To be able to measure a radial temperature profile in the experimental setup part of the packed bed had to be removed. In the CFD model only a model with a complete 44-sphere bed was available. The entire bed was present when a radial profile at a shorter bed length was collected. In bed positions at lower axial coordinates, for CFD, the temperature profile was established using the fluid elements at the specified axial position; the effects of the flow profile around the packing have a considerable influence on the resulting radial temperature profile. Also in this axial plane not all elements are fluid elements since the packing is still present limiting the domain of the data collection.

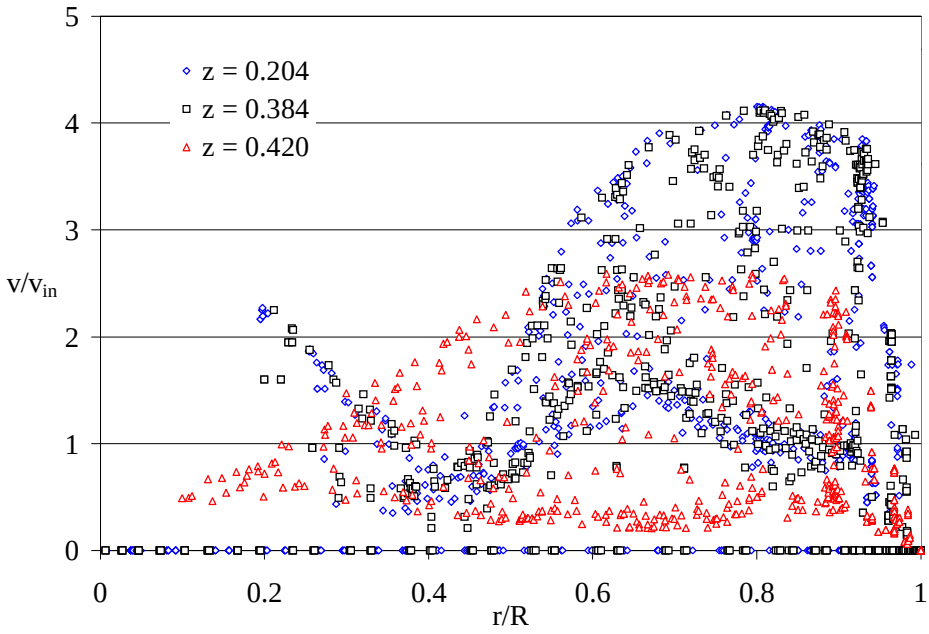

Figure 25. Plot of dimensionless velocities versus radial coordinate for different axial positions at Re = 1922, v_{in}= 1.116 m/s.

The major reason for this difference can be seen in the CFD results. When flow profiles over the complete radius at axial positions in the bed and just above the bed are compared the flow characteristics are distinctly different (see Figure 26). The packing located above the position at which the flow profile is looked at influences the specifics of the flow profile. Since in the overall heat transfer in low tube to particle packed beds convection plays an important role these differences in flow characteristics cause considerable differences in quality of the radial temperature profiles.

For interpretation of a complete series of bed depths at a Reynolds number of 986 please refer to appendix 4. In this appendix it can also be seen that all radial temperature profiles from CFD at lower bed depths have a characteristically different shape than the CFD temperature profile established with data above the packing. In the presented series the CFD simulations give a good quantitative indication of the experimental temperature profiles and their dependence on axial position, there is however a slight deviation from the expected profile shape at smaller radii. This effect becomes more prominent at larger bed lengths. These deviations at different bed lengths are caused by the different flow profile at lower bed lengths.

In the direct comparison of the experiments we look for similarity in qualitative description of the temperature profile, or the curve shape, as well as a similarity in quantitative results, or curve positioning.

A number of examples have been chosen to cover the Reynolds number range of 373 to 1922, see Table 1 in section 4.2. Also a comparison is made between using a turbulent or laminar model at lower Reynolds numbers. At lower Reynolds numbers a number of different simulations are eligible for comparison with experimental data. Simulations with the touching spheres geometry could only be conducted with the laminar model, turbulent simulations in this geometry did not converge. The laminar model is an acceptable condition for the lower Reynolds number cases. Additionally, for these low Re cases, simulations in the final geometry (99% spheres) with both laminar and turbulent models were used for comparison to find influences of the geometry and the flow model used.

5.1.3.1 Low Reynolds numbers

For these low Reynolds number comparisons a Reynolds number of 373, the lowest at which any experiments could be conducted, was chosen. In Figure 27 through Figure 29 the three different cases are given. The experimental fits given in the three different graphs are the same curve since only one experiment at these conditions was conducted.

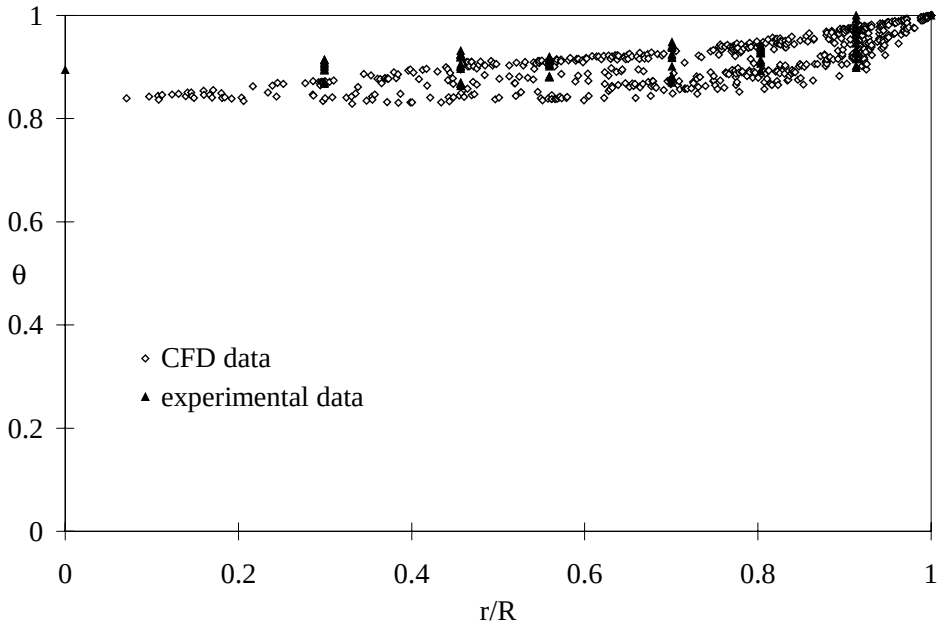

Figure 27. Comparison of experimental data and CFD for the model with touching spheres, at laminar conditions, Re = 373, z = 0.420.

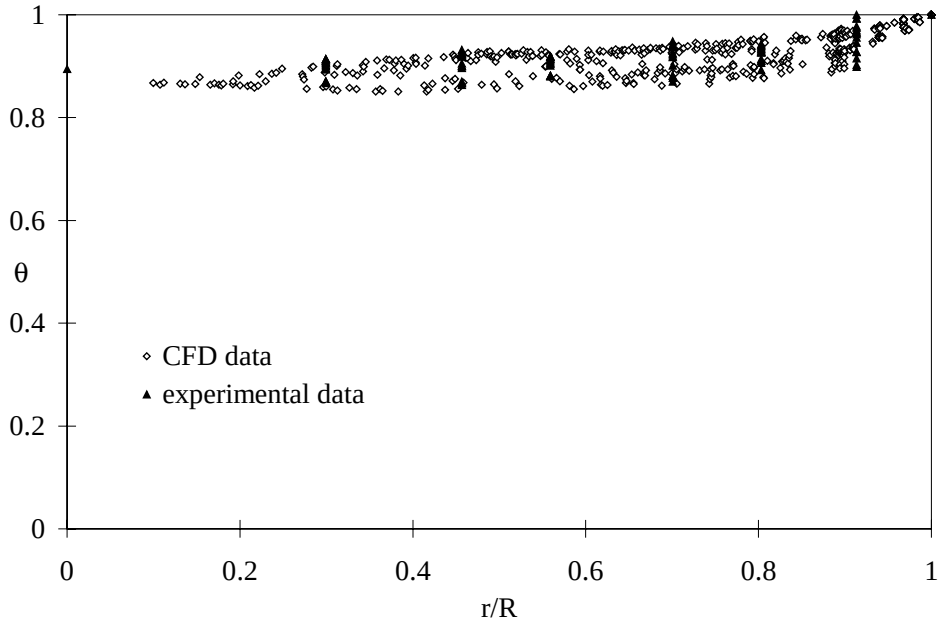

Figure 28. Comparison of experimental data and CFD for the 99% near-miss model, at laminar conditions, Re = 373, z = 0.420.

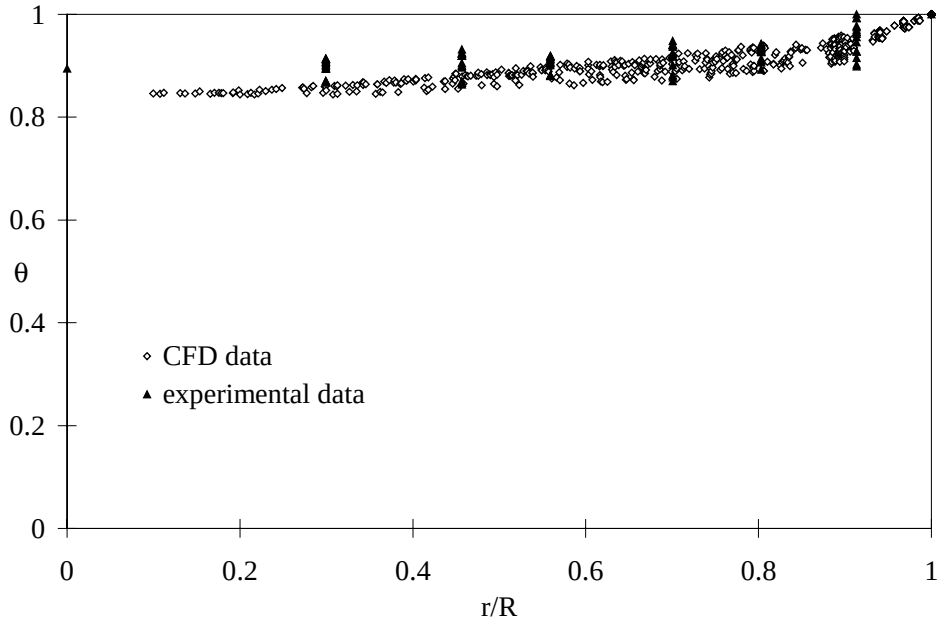

Figure 29. Comparison of experimental data and CFD for the 99% near-miss model, at turbulent conditions, Re = 373, z = 0.420.

All three graphs (Figure 27 through Figure 29) show a good qualitative similarity between the CFD and experimental data. When we compare the three graphs above, the CFD results do not change much for each of these simulations. The main difference between Figure 27 and the following two is that the CFD data indicates a slightly lower average temperature in Figure 27, approximately 1 K. This can be explained by the fact that the original geometry did not allow for an axial temperature profile on the calming section wall. The simulations in the final geometry did have a heated calming section. The temperature profile on the calming section wall will pre-heat the gas flow through the bed and cause a slightly higher radial temperature profile. The difference in the profiles at lower Reynolds numbers, as shown here, is very small because the low flow speed causes the effect of pre-heating to relatively diminish. Another distinct difference between the laminar and turbulent graphs is that the laminar cases seem to show more spread; this may be due to less mixing in gas phase compared with the turbulent flow.

In all three cases the overall temperature profile indicated by the CFD simulation is slightly lower than for the experimental data. This difference is due to systematic error in experimental data collection as well as CFD modeling assumptions that become more apparent at higher Reynolds numbers. The difference between laminar and turbulent models in the final model is very small, showing that at lower Reynolds numbers both models will predict the same heat transfer behavior.

5.1.3.2 High Reynolds numbers

At higher Reynolds numbers the preferred method of simulation is in the 99% near-miss geometry with the turbulent model. A laminar simulation in the touching spheres geometry was attempted but this did not lead to a converged solution. The touching spheres geometry only supports laminar model simulation, which is not appropriate for flow at higher Reynolds numbers.

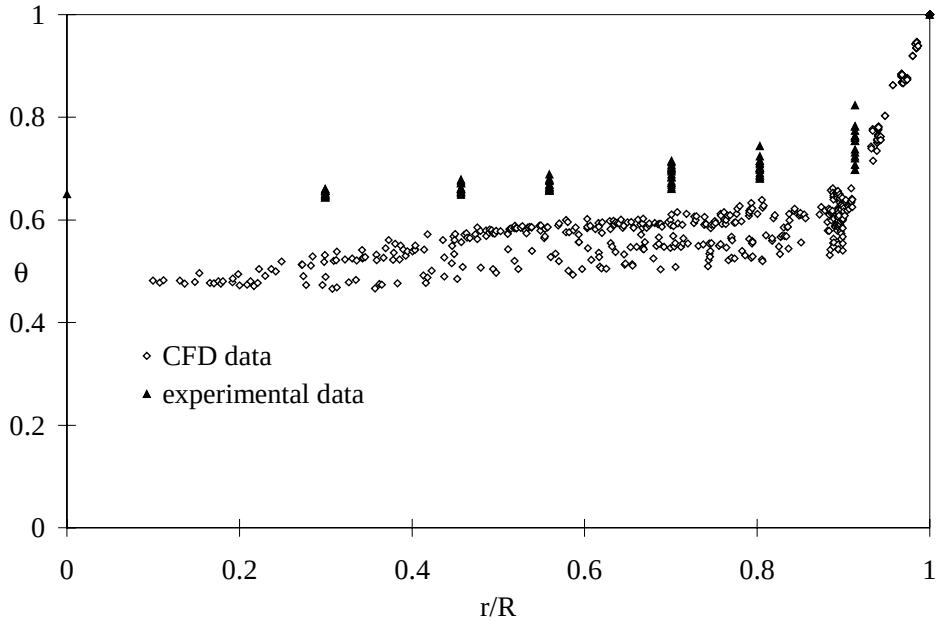

Figure 30. Comparison of experimental data and CFD results for the 99% near-miss model, at turbulent conditions, Re = 1724, z = 0.420.

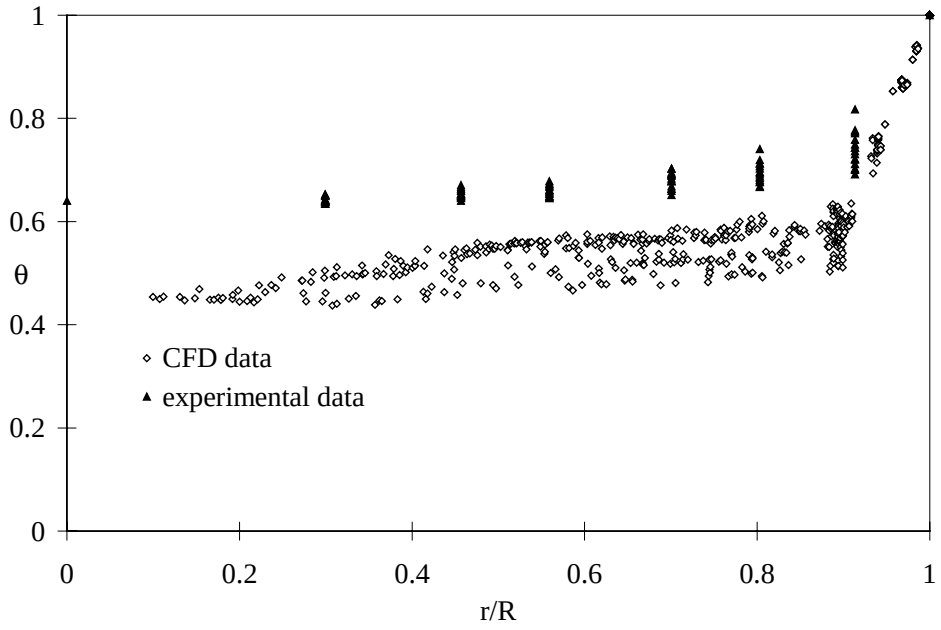

Figure 31. Comparison of experimental data and CFD results for the 99% near-miss model, at turbulent conditions, Re = 1922, z = 0.420.

As was shown in the low Reynolds number range and is shown again at higher Reynolds numbers in Figure 30 and Figure 31, the qualitative agreement between experimental and CFD data is good. Also, it can be seen that the CFD predicts a lower overall temperature profile than the experimental data shows.

An aspect that is very apparent in the CFD simulation data at higher Reynolds numbers is the temperature jump near the wall. Since at higher flow velocities there is less chance for the energy to penetrate the bed this effect is expected to be larger at higher Reynolds numbers.

When we directly compare the temperature profiles of the Re = 1922 and the Re = 1724 run there are no obvious differences. The overall temperature in the Re = 1724 is slightly higher as at the lower flow velocity there is more opportunity for the fluid to be heated by the wall. This effect becomes clearer when we compare several different Reynolds numbers

5.1.3.3 The effect of pre-heating in the calming section

As was mentioned in the paragraphs above, the temperature profiles of the CFD simulations and the experimental data seem to have a systematic offset. This difference was initially attributed to modeling problems with the axial temperature profile in the calming section wall.

When we look at the radial gas phase temperature profiles measured at z = 0.132, approximately 3 centimeters below the start of the heated wall section, we can see how the preheated wall section affects the temperature profile in the fluid phase. In Figure 32 and Figure 33 it is shown that at these low axial positions the CFD simulation already predicts a lower overall temperature profile than the experimental values indicate, especially at the lower Reynolds number.

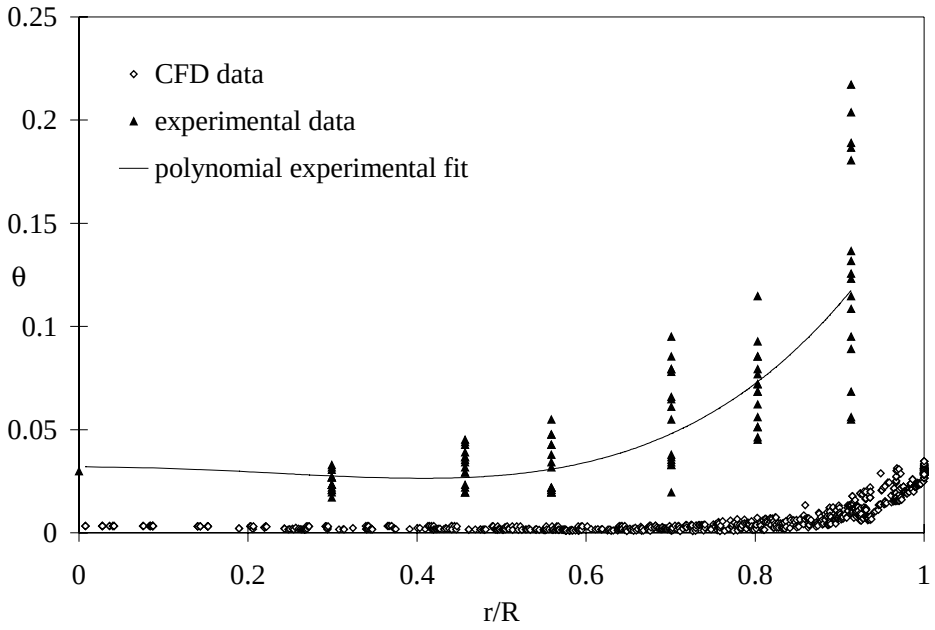

Figure 32. Comparison of experimental data and CFD results, at Re = 373, z = 0.132.

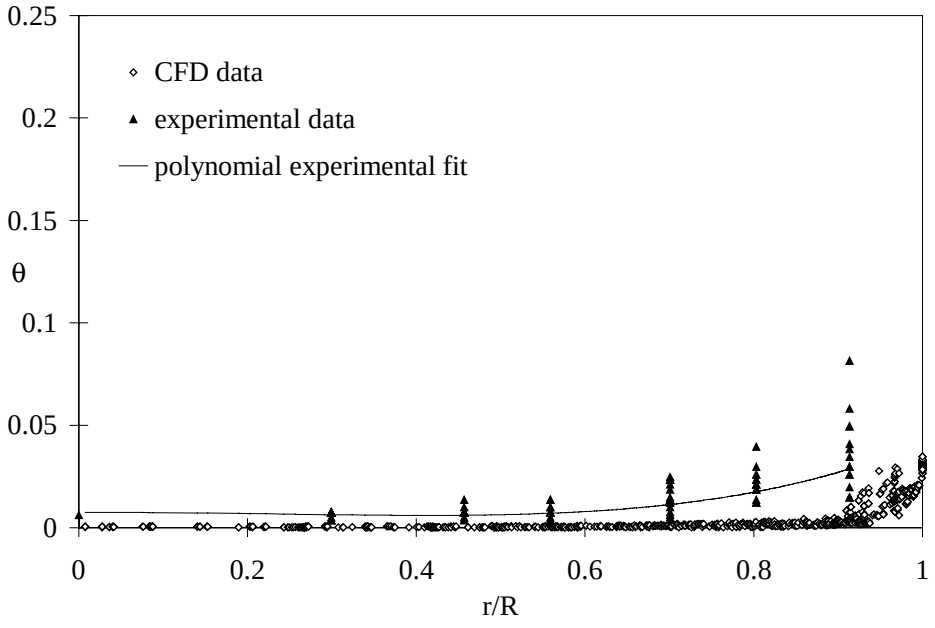

Figure 33. Comparison of experimental data and CFD results, at Re = 1922, z = 0.132.

From comparing these low axial position profiles it can be concluded that the pre-heating that should be accomplished in the calming section is not adequately represented in the CFD simulation. This will affect the temperature profile development along the remainder of the heated section. Aspects such as flow rate and the relative amount of pre-heating will have different effects on the development of the temperature profile at higher axial positions.

Even though the CFD simulation profile for the run at Re = 1922 seems to be a reasonable description of the experimental data, this small difference can be of considerable importance because the residence time in the heated section is so much smaller than in the Re = 373 run. Also, the large difference in the pre-heating section profiles at Re = 373 will be relatively more reduced, since the gas phase at a lower temperature in the CFD simulation will experience a larger driving force in the heated section and therefore heat up more, and will approach the experimental data more closely by the end of the heated section.

This may be illustrated in previously shown Figure 29 and Figure 31, where the temperature profile comparisons were plotted at the highest measured axial position. It can be seen that the differences in these profiles are differently distributed than they were in the calming section temperature profiles of Figure 32 and Figure 33. In the Re = 1922 case the short residence time in the heated section has caused the small temperature difference present in the calming section to be considerably enlarged at the end of the bed. In the Re = 373 case the longer residence time resulted in both profiles being relatively high (close to $\theta = 1$). All temperature profiles close to $\theta = 1$ are flat and close together. This indicates that even though the experimental result and the CFD prediction are close together the fit of the CFD results to the experimental data may be only as good as the one at higher Reynolds numbers, shown in Figure 31.

Another aspect of the pre-heating of the fluid phase in the calming section can be seen in the difference between temperature profiles for measurements at different Reynolds numbers.

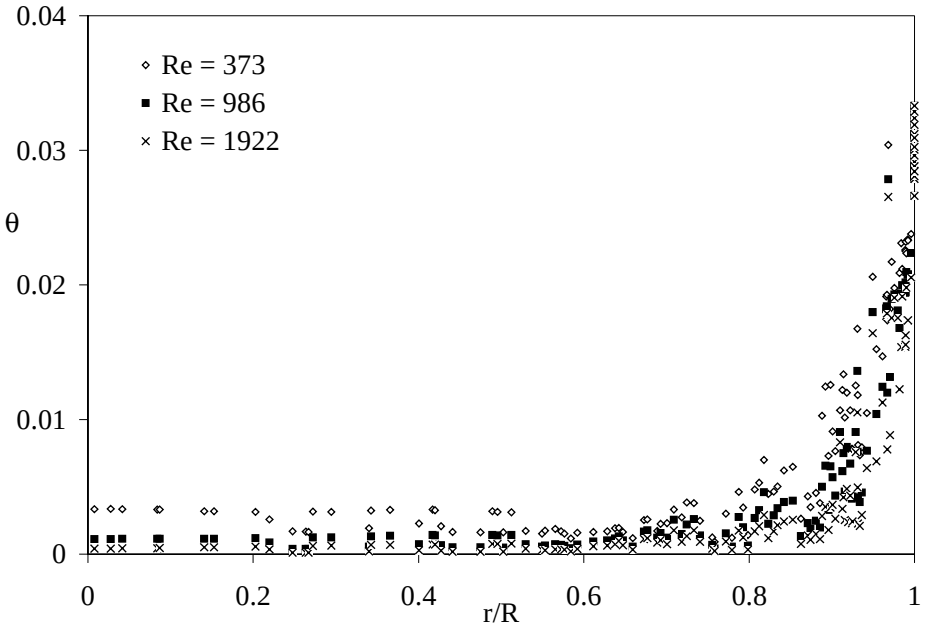

Figure 34. Temperature profiles of CFD simulations for three different Reynolds numbers at z = 0.132.

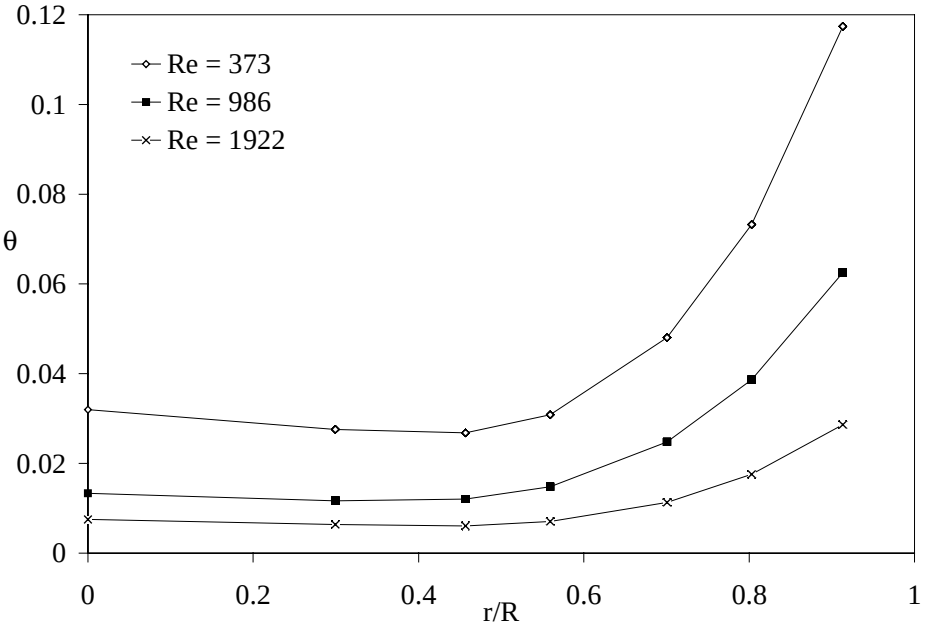

Figure 35. Temperature profiles of experiments for three different Reynolds numbers at z = 0.132.

When we compare the temperature profiles in the calming section obtained experimentally (Figure 35) with the profiles obtained through CFD simulation (Figure 34) there is a considerable and obvious difference.

As the Reynolds number increases the temperature profile tends to flatten. A flatter radial temperature profile in the calming section means there is less effective pre-heating of the fluid phase. This effect is a lot more prominent in the experimental data than it is in the CFD simulations.

The relatively high temperatures of the Re = 373 temperature profile of the experiments indicates that the effect of pre-heating in the calming section is fairly strong. The lower temperature profiles of the CFD simulations show that, even though pre-heating was modeled, the effect is less dramatic. This indicates that the modeling of the calming section axial wall profile was not adequate.

5.2 Discussion of systematic errors

In modeling in CFD a number of assumptions are made that may all introduce a small error. Also in experimental measurement, setup specifics can introduce small errors. Most of these errors individually are usually ignored in the overall measurements or modeling. When CFD results and experimental data are compared, the addition of errors will increase the overall error leading to a misleadingly large offset between the experimental data and the CFD results.

In this section several phenomena that introduce an error in either the CFD results or the experimental measurements will be identified and discussed. One of these phenomena, the correct modeling of the gas phase pre-heating in the calming section, was already introduced in section 5.1.3.3. Eventually the added effect of these errors will be implemented in the results and the new comparisons.

5.2.1 Calming section axial temperature profile

As was discussed before the incorrect modeling of the pre-heating process may explain some of the discrepancy in the CFD predictions. Therefore several measurements were taken to get a more accurate axial temperature profile. The main question was whether in the original experimental setup the wall temperature profile was truly measured or whether the gas phase temperature profile at the wall was measured.

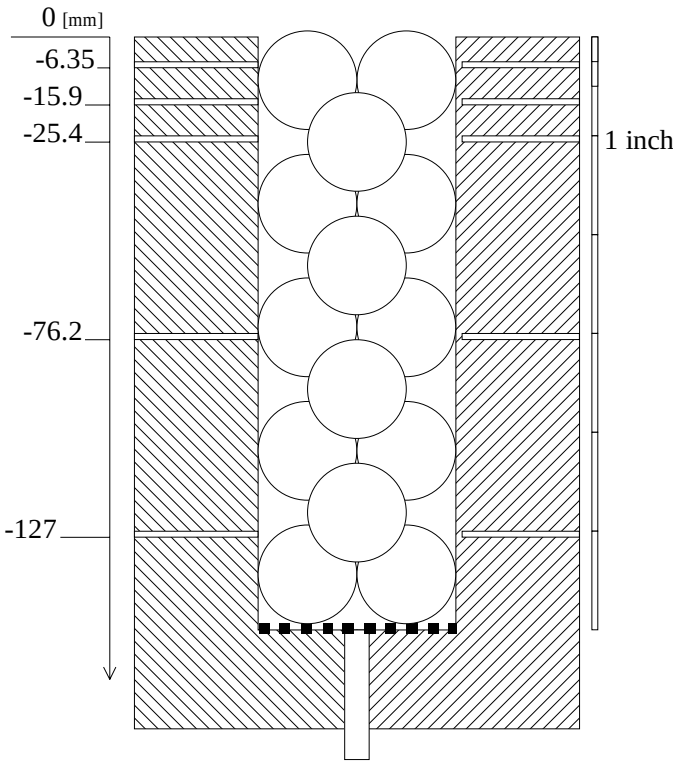

Figure 36. Calming section wall with positions of thermocouple access shafts; the left hand wall displays the original drilled holes the right hand wall the new, not quite penetrating, drilled holes.

The calming section wall axial temperature profile was established using thermocouples inserted in 5 holes drilled at different axial positions, as shown in Figure

36. The holes were drilled completely through the nylon wall of the calming section into the internal column space. The thermocouples in these holes had, over time, retracted into the holes. In the position where they were located they measured the air temperature of the stagnant air in the holes and not the wall temperature. To correct this the calming section was equipped with new-drilled holes for the thermocouples, which not quite penetrated the calming section wall. The new accesses allowed the thermocouples to be approximately 1 mm behind the inside wall interface. At this position the airflow in the column could not penetrate the thermocouple access shafts. The thermocouple tips were in contact with the wall close to the inside wall boundary resulting in a better measurement of the axial temperature profile. Figure 36 shows the two different sets of thermocouple accesses.

The newly established temperature profile was compared with experimental results from measurements done earlier (1992) on the same equipment and the profiles initially established. The axial temperature profiles on the calming section wall are presented in Table 3, here the 1992 profile refers to the axial profile established with the original drilled holes in 1992, the Initial profile was established using the original drilled holes in 1998 and the New profile was acquired using the newly drilled holes.

Table 3. Overview of the calming section wall axial temperature profiles, segment 9 at column inlet, segment 1 at heated section interface.

	1	2	3	4	5	6	7	8	9
1992 profiles	351.6	314.6	307.07	303.29	300.27	298.5	298	298	298
Initial profile	349	311.1	305.4	301.7	299.5	298.5	298	298	298
New profile	352.5	312.9	306.5	303.1	300	299	299	298	298

The temperature profile that was established in 1992 is fairly close to the profiles established with the newly drilled holes. At this point the thermocouples had been recently installed in the calming section and their location was fixed using a silicone paste. This silicone paste may have acted as a replacement wall in the thermocouple

holes. When the initial profile was established in 1998 the silicon paste had deteriorated causing the thermocouples to have been gradually moved back into the wall as well as exposing them to the airflow inside the column. This misplacement of the thermocouples and the exposure to the internal airflow resulted in a lower axial temperature profile.

After comparison the newly established temperature profile was then implemented in the CFD model and new simulations were run.

5.2.2 Experimental error due to solid conduction to the Thermocouple cross

When taking experimental measurements a thermocouple cross is lowered into the column and positioned directly above the bed. As the air flows through the bed and heats up, the thermocouples measure the gas temperature. However, the thermocouple cross itself is in contact with the heated wall and may be subject to heating through solid conduction through the nylon structure of the thermocouple cross.

To establish an estimate of the raised temperature in the thermocouple cross an experiment was developed measuring the temperature raise in the thermocouples with only conduction through the thermocouple cross. To be able to measure only the heat up of the thermocouples through conduction, all heating through the gas phase had to be eliminated without disturbing the original conditions too much. When the thermocouple cross is installed at the lower part of the heated wall section with the thermocouples just in the calming section, conduction through the nylon structure can occur without the thermocouple tips being in contact with the heated gas. In this case, however, the calming section wall is still pre-heated through contact with the heated wall. To eliminate this pre-heating of the calming section wall, and therewith the gas flowing through the column, the heated wall was placed on four 1.25 inch long aluminum struts, see Figure 37. This eliminated the contact area between the heated wall and the calming section wall. It did, however, create an open area in the column so that the total gas flow was not forced past the thermocouple cross. It was found experimentally that most of the gas flow did still

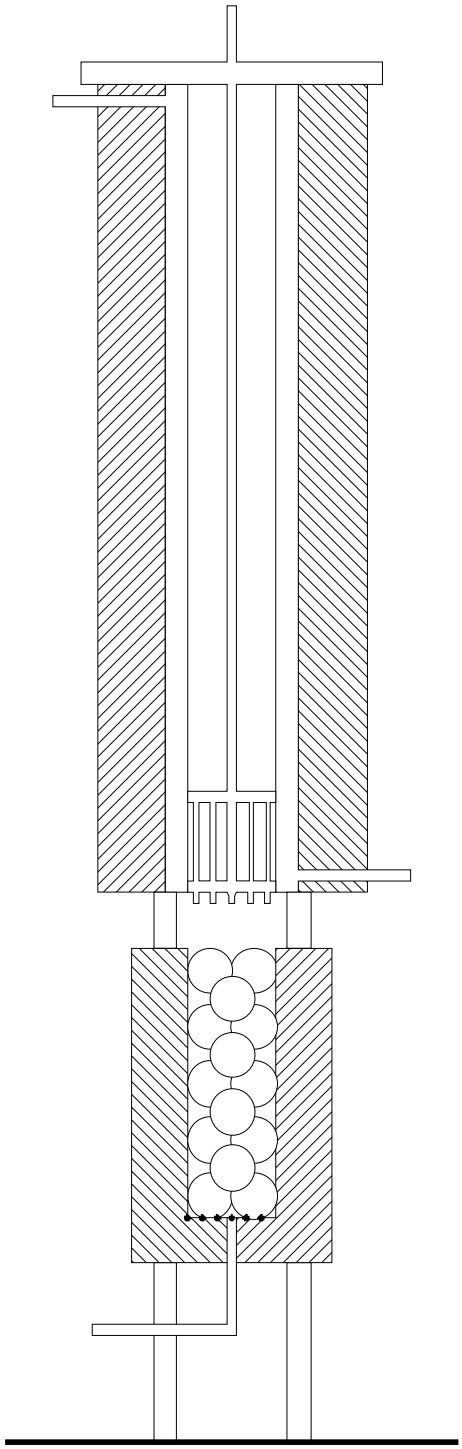

Figure 37. Experimental setup fitted with struts.

flow past the thermocouple cross through the heated column section. This condition ensured similar flow conditions at the thermocouple tips.

Steady state measurements were taken at two different Reynolds numbers (879, 1922) with both a heated column and a cold column. The difference between the cold and heated experiments shows the maximum heating through conduction through the thermocouple cross. In actual experimental conditions the temperature difference between the cross and the wall is usually lower, due to the heated gas phase, resulting in less driving force and less heating through solid conduction. Therefore this effect is more prominent at higher Reynolds numbers, since in those cases the gas phase temperature is lower.

From Figure 38 we can see that the temperature in the thermocouple cross has been raised. The dimensionless temperature was established using the wall temperature and gas inlet temperature. Therefore the θ−coordinate of each curve is directly related to the thermocouple cross heat-up through conduction. Since the heated wall and inlet temperature were approximately 100 and 25 °C respectively the 0.1 mark on the y-axis corresponds to a 7.5 °C temperature raise in the thermocouple cross.

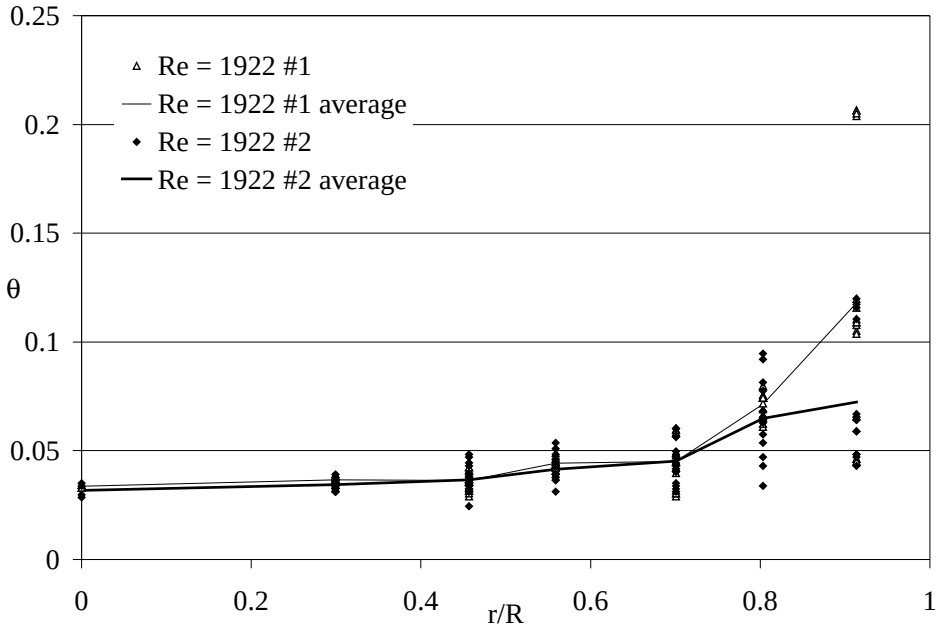

Figure 38. Experimental data from 2 separate runs at Re = 1922, combined with lines to show the average for each run.

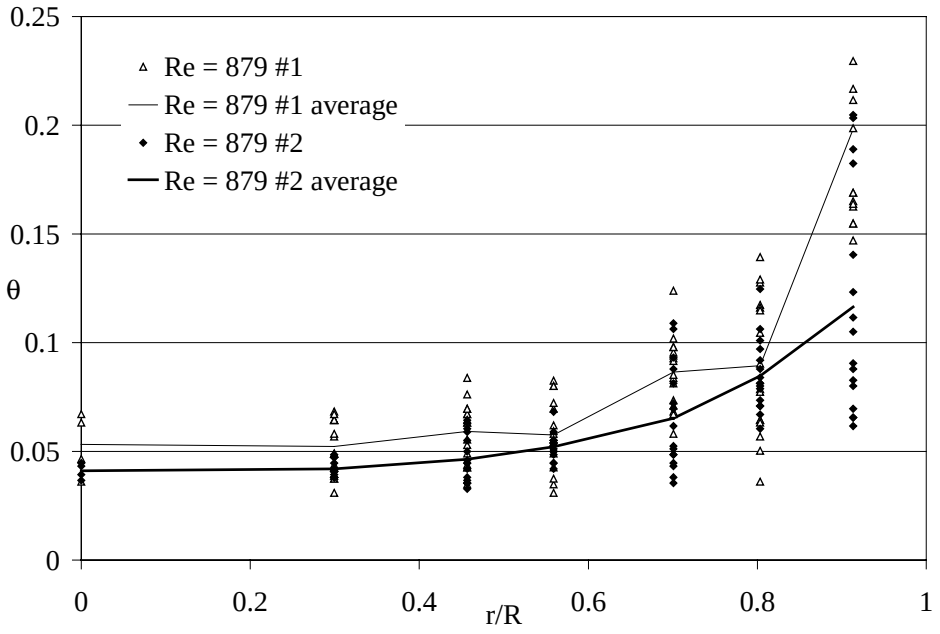

Figure 39. Experimental data from 2 separate runs at Re = 879, combined with lines to show the average for each run.

Another aspect of the heat-up through conduction becomes clear when Figure 39 is compared with Figure 38. At lower Reynolds numbers the heat-up through conduction seems to be slightly higher. As was stated before, the heat-up through conduction for the conditions of this experiment will indicate more heat-up because of the cold gas flow conditions. This also explains the higher temperatures in Figure 39; under the experimental conditions for model comparisons this additional heat-up will be less due to higher internal gas temperatures.

This effect was eventually incorporated through a lowering of the experimental data of 3 to 4 °C ranging from the center of the column to the wall. It was concluded that the already higher temperatures at the wall, under experimental conditions, would not be increased a lot more through this conduction, but the center of the column would experience the greater effect.

5.2.3 Contribution of radiation effects in experimental setup

Radiation effects were neglected in the CFD simulations since it is generally accepted that radiation effects are not a factor in heat transfer processes with temperatures lower than approximately 480 K. In our setup, however, the size of the spheres is relatively large which might make radiation a contributor to heat-up.

A calculation was done to estimate the effect of radiation. This contribution was then compared to the energy transport predicted by the CFD to find if the radiation contribution was actually negligible.

Generally radiation heat transfer can be expressed as,

$$q_r = -k_r \frac{dT}{dt} \approx -k_r \frac{T_c - T_w}{R} \qquad (21)$$

here T_c is the temperature at the center of the column, T_w is the temperature at the wall and R is the radius of the column.

The specific radiation heat transfer thermal conductivity is defined as, (Damköhler, 1937)

$$k_r = d_p \cdot \frac{0.04 \cdot e \cdot c_s}{2 - e} \left(\frac{T_c}{100} \right)^3 \qquad (22)$$

Here e is the emissivity of the nylon, approximately 0.9. The constant c_s is derived from the Stefan-Boltzman constant and is in this case 5.67.

The CFD simulation uses only conduction and convection for heat transfer into the column. Its heat flux into the column is given as,

$$q_{CFD} = -k_{CFD} \frac{T_c^{CFD} - T_w^{CFD}}{R} \qquad (23)$$

When we now combine equation (21) and (23) we can find the temperature in the center of the column if radiation were taken into account in the CFD simulation, T_c^*.

$$q = q_{CFD} + q_r = -(k_{CFD} + k_r) \frac{T_c^* - T_w^{CFD}}{R} \qquad (24)$$

For this specific calculation a Reynolds number of 1922 was chosen, at lower Reynolds numbers, the difference between T_c and T_w values will be less, resulting in less radiation contribution. The radiation heat transfer thermal conductivity, k_r, is calculated using equation (22), which is then used in equation (21) to establish the radiation heat transfer, q_r. In these equations the value of T_c cannot be directly established since it changes with the axial position in the bed, therefore an average value of 50.5 °C was used. For the CFD simulation T_c was determined similarly at 317 K. Using equation (23) k_{CFD} was calculated with values for q_{CFD} taken from the simulation. Wall temperatures in the CFD simulation were set at 383 K. In the experiment, at a Reynolds number of 1922, the wall temperature was 104 °C.

Using these values we find that the temperature in the CFD simulation should be approximately 2.5 K higher than was calculated neglecting radiation at a Reynolds number of 1922. When we do similar calculations for a Reynolds number of 373 we find

that at this low Reynolds number there is negligible additional heat up through radiation. The heat up at lower Reynolds numbers is negligible because the radiation effect, which is directly related to the temperature difference between the wall and the center of the bed, is applied to a smaller energy stream. Even though the temperature of the airflow in the column is higher at lower Reynolds numbers the flux is so much lower that the total energy flux through the column at a Reynolds number of 373 is only 27.5 % of the energy flux at a Reynolds number of 1922. The smaller radiation effect due to the smaller driving force at Re = 373 applied to a smaller energy flux results in a negligible temperature increase at low Reynolds numbers.

5.2.4 Additional heat transfer through solid-wall contact points

The experimental setup uses nylon 66 spheres with a one-inch diameter in a copper column with a two-inch inner diameter. Long-term use and production imperfections make neither of these diameters perfectly one or two inches. A number of measurements were taken to get an approximation of the actual diameters. It was established that the average diameter of the spheres was slightly larger than one inch and the diameter of the heated section of the column was slightly smaller than two inches, which was also something that was experienced experimentally when installing the packing.

The smaller column diameter and the larger sphere diameter resulted in a considerable solid-solid contact area between the wall and the spheres resulting in extra heat transfer into the bed, that was not incorporated in the CFD model. To correct this, the surface area was crudely determined and used in determining the extra heat transfer into the bed. To determine the heat transfer into the bed a modified Batchelors equation was used (Cheng et al., 1999)

$$Q = \frac{4r_{ws} \cdot (T_w - T_s)}{\left(1/k_{sw} + 1/k_{ss}\right)} \qquad (25)$$

where the subscript s refers to the sphere and w refers to the wall, r_{ws} is the radius of the contact area between the wall and the sphere, k_{sw} is the solid conductivity of the wall and k_{ss} is the solid conductivity of the spheres.

Using the diameter measurements of the spheres and the column we find an average contact radius of 1.12 mm for each sphere in the packing, since in the N = 2 packing all spheres touch the wall. There are a total of 28 spheres touching the heated wall with an average temperature difference between the wall and the sphere of 53 K (for Re = 1922). The solid conductivities are respectively k_{sw} = 202.4 W/m·K and k_{ss} = 0.242 W/m·K.

With the mentioned values for all parts of equation (25) the additional heat flux into the column due to solid-solid contact between the heated wall and the packing is 1.73 W. This is about 1.3% of the heat flux into the gas phase in the CFD simulation (136 W).

To correct for the solid-solid conduction in the CFD result the contact areas between wall and packing should be incorporated, but as was discussed in Chapter 2 this increases geometrical complexity and would make it very difficult to solve for the flow in the simulation.

To correct for this additional conduction, the CFD temperatures were increased by 0.7 K, corresponding to the percentage additional heat flux into the column.

5.2.5 Modeled gap between wall and packing

To be able to solve for turbulent flow in a CFD simulation it was necessary to introduce a small gap between the heated wall and the spheres. It was shown from comparisons of flow profiles at several gap sizes that the small gaps used in the final model did not affect the stagnant flow area around the contact points, see Figure 40. It did however make it impossible to model contact areas, as discussed in section 5.2.4. Another aspect was an increase in conduction path length through the gas, which was expected to be of relatively small influence in our specific case since the packing-fluid conductivity ratio was low at approximately 10.

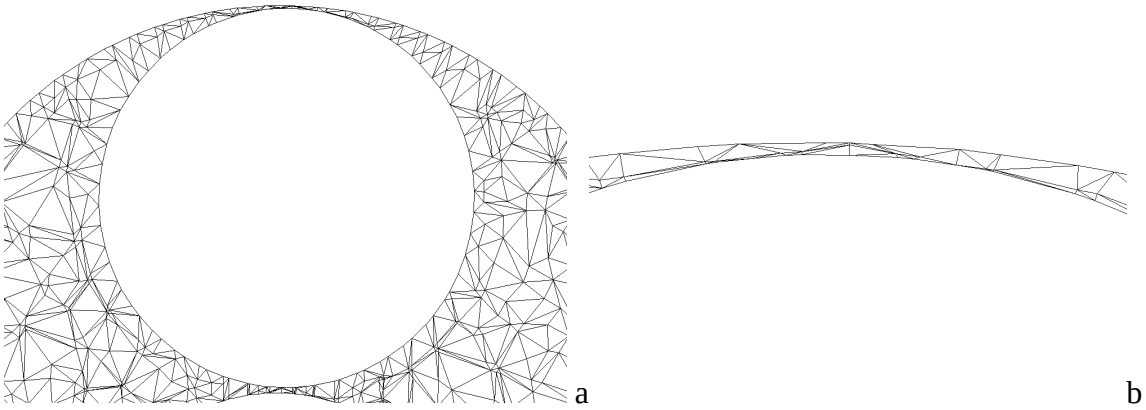

Figure 40. View of the CFD mesh at a constant axial coordinate showing the introduced gap between the sphere and the wall, a, and a close up of the area near the sphere-wall contact point, b.

When we compare radial temperature profiles we find a systematically lower temperature in the near-miss model, approximately 1.5 K at a Reynolds number of 373. Another way to compare the gap influence is directly comparing temperatures in the packing in models with different gap sizes. The trend found in this comparison shows that at the 99% near-miss model the temperature in the packing is approximately 2 K lower at a Reynolds number of 1922. Since the Reynolds number has no influence on the heat transfer through the gap, the flow pattern has not been significantly altered; the only influence of Reynolds number is the overall temperature difference over the column radius, the driving force for the heat transfer.

The introduction of the gap causes the CFD simulations to predict too low a temperature, ranging from 1.5 K at Re = 373 to 2 K at Re = 1922. To correct for this offset the CFD radial temperature profiles were increased by 1.5 to 2 K depending on the Reynolds number

5.2.6 Additionally checked aspects

In addition to the contribution of the effects discussed in sections 5.2.1 through 5.2.5 other aspects in the model and experimental setup were investigated. The additionally

investigated effects discussed in this section turned out to have a negligible effect on the final results, they are mentioned here solely for completeness.

5.2.6.1 Flow inlet effects

It was reasoned that there might be an influence of the inlet effects of the gas flow. In the experimental setup a gas is fed through a small diameter inlet to the bottom of the calming section, whereas in the CFD simulation a flat velocity profile is defined at the inlet at the bottom of the calming section.

The calming section was specifically designed to negate such effects in the flow, but the column used was originally designed for considerably larger tube to particle ratios; also the axial temperature profile on the calming section wall effectively shortens the calming section. Any jet effect in the experimental setup may cause the development of the flow profile to be delayed causing changes in heat transfer processes.

Experiments were performed with a 1.5-inch layer of 5/16-inch nylon spheres at the bottom of the calming section inlet and at a series of Reynolds numbers as shown in Table 4. This larger tube to particle ratio section (N = 6.4) disperses the flow before it reaches the preheated calming section wall. When experimental results of the two different packing methods were compared the difference in radial temperature profiles, approximately 0.1 °C, fell within the response variation of both profiles.

Table 4. Overview of all the Reynolds numbers at which flow inlet experiments were conducted.

Reynolds numbers							
373	564	796	986	1221	1477	1724	1922

From these experiments it is concluded that the flow inlet effects have negligible effect on the overall heat transfer process. At Reynolds numbers higher than 1922 there may be noticeable effects from a jet effect since development of the steady profile will occur later in the bed.

5.2.6.2 Calibration of Thermocouples

Although the thermocouples were calibrated at the time the measuring software was implemented, it was deemed necessary to recalibrate the thermocouples as the time since the initial calibration may have had an adverse effect on the thermocouples. The calming section thermocouples were determined to have an offset up to - 0.5 °C; the thermocouples in the thermocouple-cross however were determined to have an offset up to - 0.2 °C. These effects counteract each other resulting in a negligible final temperature offset.

The negative offset means the temperature indicated by the thermocouples was actually lower than the calibration temperature. The calibration was done over a temperature range, 10 to 90 °C. All thermocouples showed a consistent offset at all temperatures; the highest deviation from a constant offset was 0.2%.

5.2.6.3 Turbulence models

When solving the CFD equations a model is implemented for turbulent factors. In the Fluent software several turbulence models are available. The turbulent simulations in this work were done with the standard κ-ε model. Although unlikely, it was reasoned that choice of the turbulent model might influence the flow solution and therewith the overall heat transfer processes.

A number of runs were conducted using different turbulence models at the highest modeled Reynolds number, 1922. The available turbulent models in Fluent 4.2.8 were, the standard κ-ε model, the renormalized group κ-ε or RNG κ-ε model and the Reynolds Stress Model or RSM.

The RNG κ-ε differs only slightly from the standard κ-ε model in that it uses different techniques for determining effective viscosities. The RSM turbulent modeling does not

use κ and ε parameters to model the Reynolds stresses; it models all six stresses separately.

The results of the different turbulent models were directly compared, resulting in a maximum difference of about 0.2 K for some temperatures. It was concluded that the different turbulence models did not show structural difference in the radial temperature profiles. The standard κ-ε model was therefore used on all turbulent simulations.

5.3 Corrected comparisons

When we consider all the elements discussed in section 5.2 we can adjust our original plots, as presented in section 5.1, to obtain a corrected comparison. In this section we make similar comparisons as was done in section 5.1 and look at some additional aspects of the data.

5.3.1 Review of proposed corrections

In section 5.2 a number of aspects were mentioned resulting in a correction factor for either the CFD simulation or the experimental measurements. In Table 5 a summary of the correction factors is given for three different particle-Reynolds numbers. The method of calculation for the corrections was similar for all Reynolds numbers, the differences were caused mainly by difference in temperature difference between the wall and the center of the bed and the difference in total energy added to the system as calculated in the CFD simulation.

Table 5. Overview of the corrections on the CFD and experimental radial temperature profiles, all corrections in K.

Re	373		968		1922	
Effects	CFD	Exp	CFD	Exp	CFD	Exp
TC cross conduction	-	-2	-	-3	-	-4
Radiation	-	-	+2.1	-	+2.5	-
Solid-solid conduction	+1.6	-	+0.9	-	+0.7	-
Modeled gap	+1.5	-	+1.7	-	+2	-

5.3.2 Direct comparison of results

Now that we can implement the corrections quantified in the last section a new comparison between CFD simulations and experimental results can be made.

5.3.2.1 Low Reynolds numbers

In section 5.1.3.1 a comparison was made between CFD results and experimental data. It was then shown that a systematic difference between the experimental data and CFD simulation was present. The corrected graphs for the same runs as were shown in section 5.1.3.1 are presented now to give a better representation of the comparison.

In the corrected graphs the experimental data and the CFD simulation are in better agreement than they were before the correction. At the low Reynolds numbers the largest discrepancy was found near the center of the column, in Figure 41 and Figure 42 the temperatures in the center of the column are in perfect agreement.

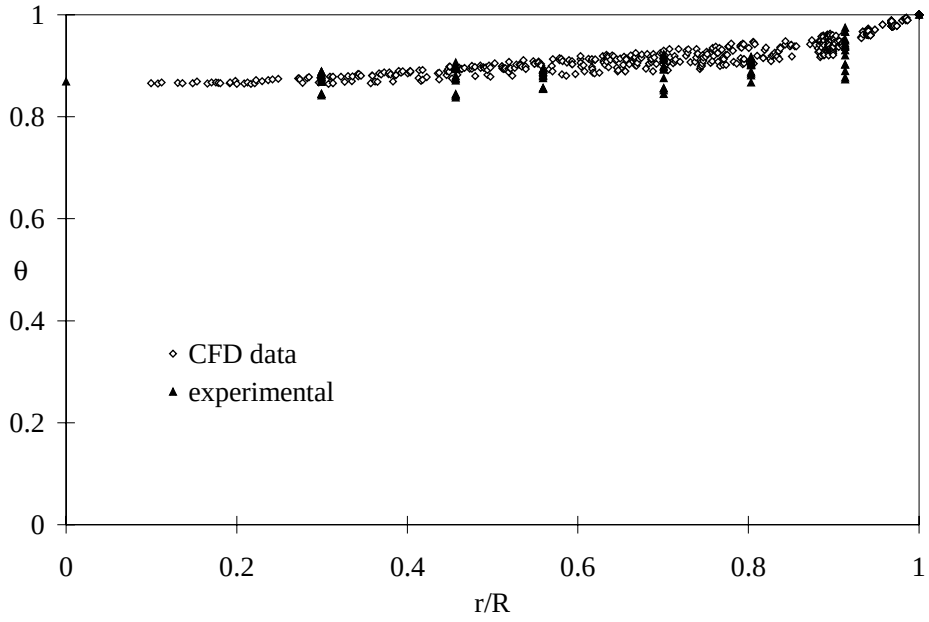

Figure 41. Comparison of corrected experimental and CFD results, at turbulent conditions, Re = 373, z = 0.420.

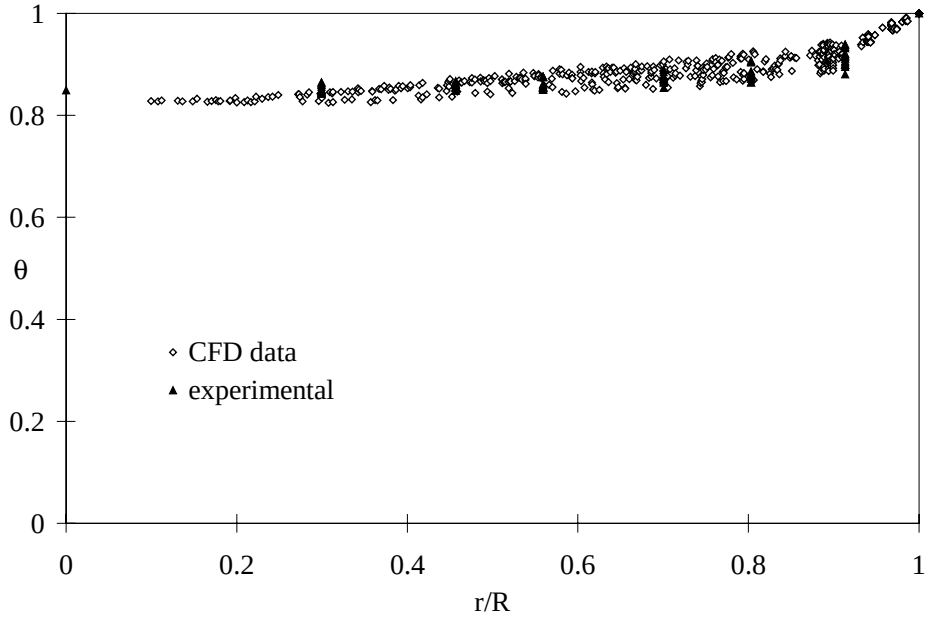

Figure 42. Comparison of corrected experimental and CFD results, at turbulent conditions, Re = 468, z = 0.420.

5.3.2.2 High Reynolds numbers

At higher Reynolds numbers the discrepancy between experimental results and CFD simulations shown previously was a lot larger. As we found in section 5.2 and is shown in Table 5 the correction for higher Reynolds numbers is larger as well. The following graphs show the corrected comparisons for the higher Reynolds numbers cases.

Especially at these higher Reynolds numbers the effects of the corrections can be seen. It is clear that when the aspects that were not included in the model are corrected for the CFD simulation gives a quantitatively as well as qualitatively good comparison.

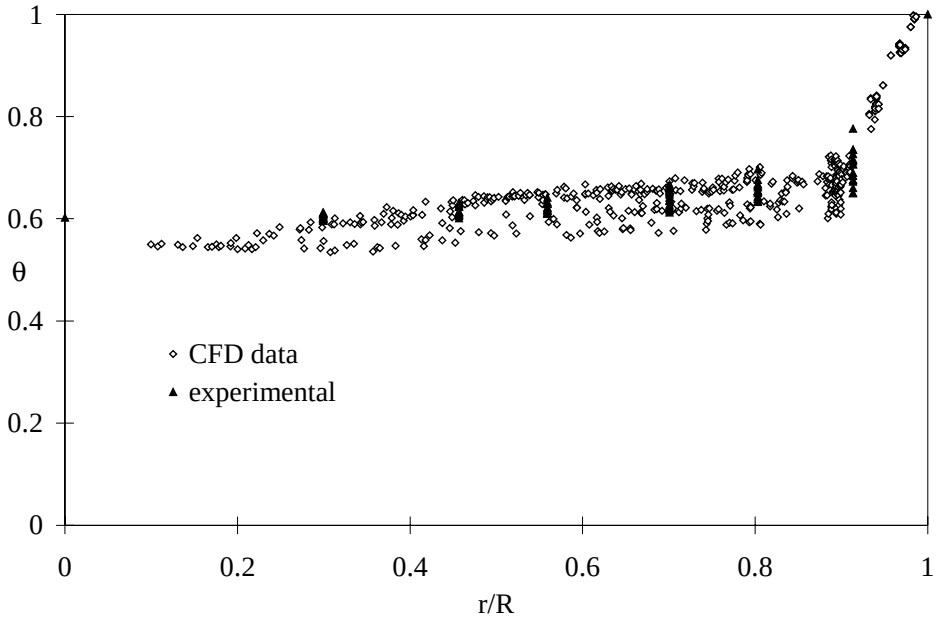

Figure 43. Comparison of corrected experimental and CFD results, at turbulent conditions, Re = 1724, z = 0.420.

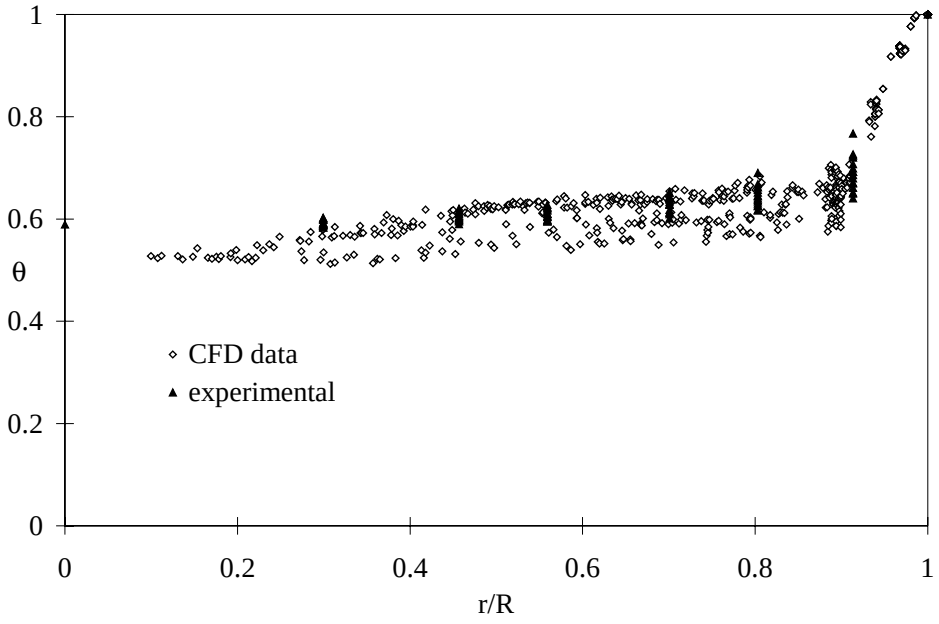

Figure 44. Comparison of corrected experimental and CFD results, at turbulent conditions, Re = 1922, z = 0.420.

6. Conclusions

Model and mesh creation in CFD is one of the most important phases of simulating. The model and mesh density determine the accuracy and flexibility of the simulations. Too dense a mesh will unnecessarily increase the solution time; too coarse a mesh will reach a solution quickly but will not show an accurate flow profile. An optimal mesh is denser in areas where the flow profile changes quickly and coarser in areas where there are no flow profile changes. In the used 44-sphere model with 1 inch diameter spheres a node spacing of 0.11 inch near the contact points and 0.26 inch away from the contact points was found to be optimal.

Solving turbulent equations puts extra demands on a CFD model and will require a more stable mesh. Skewness, the distortion of the tetrahedral mesh volumes, becomes more important and the model needs to have a lower skewness than is allowed for laminar solutions. To be able to facilitate turbulent solution of the model actual contact points had to be eliminated. Comparing several models with differing gap sizes between the spheres and the wall it was found that models with a sphere size of 99% of the original touching spheres model facilitated a turbulent solution as well as maintained the original velocity distribution around the contact points.

The CFD simulation results from the 99% near-miss model and experimental data show a good qualitative fit. When CFD simulations are corrected for the introduced gap, by adding a solid-solid conduction heat transfer contribution as well as adding a radiation contribution that was not included in the simulation and experimental results are adjusted for bias introduced due to the measurement method there is a good quantitative fit. Showing a good quantitative as well as qualitative fit between CFD simulation and experimental results it can be concluded that for the case of low N packed beds CFD simulations are a useful tool for understanding flow and heat transfer principles as well as for modeling these types of geometries.

7. Recommendations

An immediate extension of the research presented could be implementing a more accurate calming section wall temperature profile. A newer version of Fluent UNS with a capable C compiler will be able to be implemented with a User Defined Function, which can describe this temperature profile better. Other ways to improve simulation can be sought in introducing radiation in the model; this will lead to a more complicated solution but will also eliminate the need for temperature profile corrections.

Since it has been shown that CFD is a useful tool in modeling low N packed beds applications for further research may be sought in modeling chemical reactions in a fixed bed with the reported optimal mesh density. With this reaction CFD model data can be gathered for direct application into a model describing low N packed bed behavior.

Besides looking at heat transfer results, the flow field also provides a wealth of information. The flow field distributions, such as axial or radial flow, may be incorporated in packed bed flow models.

For future studies it will be necessary to create specific new models. With this study we hope to have shown that CFD simulations give an accurate description of the heat and mass transfer in small tube to particle ratio beds. The newly designed models can be founded on mesh design principles stated in this study. Also CFD generated with a well-designed model gives accurate enough data for further application.

Nomenclature

c_p =	fluid heat capacity	[J/kgK]
d_t =	tube diameter	[m]
d_p =	particle diameter	[m]
e =	emissivity	[-]
G =	mass flow rate	[kg/m^{2}s]
h =	heat transfer coefficient	[W/m^{2}K]
h_w =	wall heat transfer coefficient	[W/m^{2}K]
k_f =	fluid conductivity	[W/mK]
k_r =	radial conductivity	[W/mK]
k_{ss} =	solid conductivity of the sphere	[W/mK]
k_{sw} =	solid conductivity of the wall	[W/mK]
L =	length of the heated bed	[m]
N =	tube to particle ratio (d_t/d_p)	[-]
Nu_w =	wall heat transfer coefficient	[-]
P, p =	static pressure	[Pa]
q =	heat flux	[W/m^2]
r =	radial coordinate	[m]
r_{ws} =	radius of wall sphere contact area	[m]
R =	tube radius	[m]
T =	temperature	[K]
u =	gas velocity	[m/s]
v =	superficial gas velocity	[m/s]
x =	coordinate	[m]
z =	axial coordinate	[m]

Greek Symbols

β =	thermal expansion coefficient	$[K^{-1}]$
ε =	turbulence dissipation rate	[J/s]
κ =	turbulent kinetic energy	[J]
μ =	fluid viscosity	$[Ns/m^2]$
θ =	dimensionless temperature $(T-T_{in})/(T_{wall}-T_{in})$	[-]
ρ =	fluid density	$[kg/m^3]$

Dimensionless flow numbers

wall Nusselt number $$Nu_w = \frac{h_w d_p}{k_f}$$

Péclet number $$Pe = \frac{G c_p d_p}{k_r}$$

Prandtl number $$Pr = \frac{c_p \mu}{k_f}$$

Reynolds number $$Re_p = \frac{\rho v d_p}{\mu}$$

Abbreviations

CAD =	Computer Aided Design
CFD =	Computational Fluid Dynamics
FD =	Finite Difference
FE =	Finite Element
FV =	Finite Volume
UNS =	Unstructured

Literature references

Bode, J. (1994) Computational fluid dynamics applications in the chemical industry. *Computers & Chemical Engineering* **18** SUPPL, S247-S251

Bey, O. and Eigenberger, G. (1997) Fluid flow through catalyst filled tubes. *Chemical Engineering Science* **52**, 1365-1376.

Carslaw, H.S. and Jaeger, J.C. (1959) C*onduction of Heat in Solids.* 2nd edition, University Press, Oxford.

Cheng, G.J., Yu, A.B. and Zulli, P. (1999) Evaluation of effective thermal conductivity from the structure of a packed bed. *Chemical Engineering Science* **54**, 4199-4209.

Dalman, M.T., Merkin, J.H. and McGreavy, C. (1986) Fluid flow and heat transfer past two spheres in a cylindrical tube. *Computers & Fluids* **14**, 267-281.

Damköhler, G. (1937) *Der Chemie Ingenieur, Eucken-Jacob* Volume 3, Akadem. Verlag., Leipzig

Daszkowski, T. (1991) Strömung, stoff- und wärmetransport in schüttungsgefüllten rohrreaktoren. *Ph.D. Thesis*, Institute für Chemische Verfahrenstechnik, Universität Stuttgart.

Derkx, O.R. (1995) Wall heat transfer coefficient in a fixed bed reactor. *M.S. Thesis* Worcester Polytechnic Institute.

Derkx, O.R. and Dixon, A.G. (1996) Determination of the fixed bed wall heat transfer coefficient using computational fluid dynamics. *Numerical Heat Transfer Part A* **29**, 777-794.

Dixon, A.G. (1985) The length effect on packed bed effective heat transfer parameters. *Chemical Engineering Journal* **31**, 163-173.

Dixon, A.G. (1997) Heat transfer in fixed beds at very low (<4) tube-to-particle diameter ratio. *Industrial and Engineering Chemistry Research* **36**, 3053-3064.

Dixon, A.G. and Cresswell, D.L. (1979) Theoretical prediction of effective heat transfer parameters in packed beds. *AIChE Journal* **25**, 663-676.

Fluent UNS version 4.2.8 User's Guide Volume 2 (1997) Fluent, Inc

Freiwald, M.G. and Paterson, W.R. (1992) Accuracy of model predictions and reliability of experimental data for heat transfer in packed beds. *Chemical Engineering Science* **47**, 1545-1560.

Froment, G. and Bisschoff, K. (1979) *Chemical Reactor Analysis and Design.* Wiley, New York.

Giese, M., Rottschäfer, K. and Vortmeyer, D. (1998) Measured and modeled superficial flow profiles in packed beds with liquid flow. *AIChE Journal* **44**, 484-490.

Haidegger, E., Vortmeyer, D. and Wagner, P. (1989) Simultane lösung van energie-, stoff- und impulsgleichungen für wandgekühlte chemische festbettreaktoren. *Chemie Ingenieur Technik* **61**, 647-650.

Harris, C.K., Roekaerts, D., Rosendal, F.J.J., Buitendijk, F.G.J., Daskopoulos, Ph., Vreenegoor, A.J.N. and Wang, H. (1996) Computational fluid dynamics for chemical reactor engineering. *Chemical Engineering Science* **51**, 1569-1594.

Kalthoff, O. and Vortmeyer, D. (1980) Ignition/extinction phenomena in a wall cooled fixed bed reactor experiments and model calculations including radial porosity and velocity distributions. *Chemical Engineering Science* **35**, 1637-1643.

Kutsovsky, Y.E., Scriven, L.E., Davis, H.T. (1996) NMR Imaging of velocity profiles and velocity distribution in bead packs. *Physical Fluids* **8**, 863-871.

Launder, B.E., Spalding, D.B. (1972) *Lectures in mathematical models of turbulence.* Academic Press, London

Lerou, J.J. and Froment, G.F. (1977) Velocity, temperature and conversion profiles in fixed bed catalytic reactors. *Chemical Engineering Science* **32**, 853-861.

Li, C.H. and Finlayson, B.A. (1977) Heat transfer in packed beds - a reevaluation. *Chemical Engineering Science* **32**, 1055-1066.

Lloyd, B. and Boehm, R. (1994) Flow and heat transfer around a linear array of spheres. *Numerical Heat Transfer, Part A* **26**, 237-252.

Logtenberg, S.A. (1997) Computational fluid dynamics studies of fixed bed heat transfer. *M.S. Thesis*, Worcester Polytechnic Institute.

Logtenberg, S.A. and Dixon, A.G. (1998a) Computational fluid dynamics studies of fixed bed heat transfer. *Chemical Engineering and Processing* **37**, 7-21.

Logtenberg, S.A. and Dixon, A.G. (1998b) Computational fluid dynamics studies of the effects of temperature-dependent physical properties on fixed-bed heat transfer. *Industrial and Engineering Chemistry Research* **37**, 739-747.

Logtenberg, S.A., Nijemeisland, M. and Dixon, A.G. (1999) Computational fluid dynamics simulations of fluid flow and heat transfer at the wall-particle contact points in a fixed bed reactor. *Chemical Engineering Science* **54**, 2433-2439.

Mark, H.F., editor in chief. (1978) *Kirk & Othmer Encyclopedia of Chemical Technology*. 3rd edition, Wiley, New York.

Mark, H.F., editor in chief. (1985) *Encyclopedia of Polymer Science and Engineering.* 2nd edition, Wiley, New York.

McGreavy, C., Kam, E.K.T., Foumeny, E.A., Guidoum, A. and Ikponmwosa, A.N. (1984) A study of flow patterns in packed beds. *2nd International Symposium on Application of Laser Anemometry to Fluid Mechanics* Lisbon, July.

McGreavy, C., Foumeny, E.A. and Javed, K.H. (1986) Characterization of transport properties for fixed bed in terms of local bed structure and flow distribution. *Chemical Engineering Science* **41**, 787-797.

Melanson, M.M. (1984) Solid phase radial heat transfer in stagnant packed beds for low tube to particle diameter ratios. *M.S. Thesis,* Worcester Polytechnic Institute.

Morales, M., Spinn, C.W. and Smith, J.M. (1951) Velocities and effective thermal conductivities in packed beds. *Industrial and Engineering Chemistry Research* **43**, 225-231.

Papageorgiou, J.N. and Froment, G.F. (1995) Simulation models accounting for radial voidage profiles in fixed-bed reactors. *Chemical Engineering Science* **50**, 3043-3056.

Park, J. and Gibbs, J.G. (1999) Mapping flow and dispersion in a packed column by NMR. *AIChE Journal* **45**, 655-660.

Price, J. (1968) The distribution of fluid velocities for randomly packed beds of spheres. *Mech. Chem. Engng Trans.* **7**, 14.

Ranade, V.V. (1995) Computational fluid dynamics for reactor engineering. *Reviews in Chemical Engineering* **11**, 229.

Ranz, W.E. and Marshall Jr., W.R.(1952) Evaporation from drops, part 1. *Chemical Engineering Progress* **48**, 173-180.

Schuster J. and Vortmeyer, D. (1981) Geschwindigkeit in gasdurchströmten, isothermen kugelschüttungen. *Chemie Ingenieur Technik* **53**, 806-807.

Sederman, A.J., Johns, M.L., Bramley, A.S., Alexander, P. and Gladden, L.F. (1997) Magnetic resonance imaging of liquid flow and pore structure within packed beds. *Chemical Engineering Science* **52**, 2239-2250.

Thompson, K.E. and Fogler, H.S. (1997) Modeling flow in disordered packed beds from pore-scale fluid mechanics. *AIChE Journal* **43**, 1377-1389.

Tsotsas, E. and Schlünder, E.-U. (1990) Heat transfer in packed beds with fluid flow: remarks on the meaning and the calculation of a heat transfer coefficient at the wall. *Chemical Engineering Science* **45**, 819-837.

Vortmeyer, D. and Haidegger, E. (1991) Discrimination of three approaches to evaluate heat fluxes for wall-cooled fixed bed chemical reactors. *Chemical Engineering Science* **46**, 2651-2660.

Ziòlkowska, I. and Ziòlkowski, D. (1993) Modeling of gas interstitial velocity radial distribution over a cross-section of a tube packed with a granular catalyst bed. *Chemical Engineering Science* **48**, 3283-3292.

Appendices

Appendix 1 Overview of CFD simulations

This appendix contains an overview of all the performed CFD simulations. Only a few of the CFD simulations are reported on in the thesis, these tables are there to give a complete overview of the simulations performed.

Table 6. Overview of the CFD runs of the 10-sphere geometry.

Mesh	Run	v_{inlet} [m/s]	Reynolds	flow regime	# its	remarks
10spheres	10spheres	0.01	34	laminar	123	metal spheres
10spheres2	10spheres2	0.01	34	laminar	123	Al_2O_3 spheres
	10sphv=0,01noheat	0.01	34	laminar	120	flow only
	10sphv=0,01	0.01	34	laminar	131	
	10sphv=0,05nh	0.05	169	laminar	206	flow only
	10sphv=0,05	0.05	169	laminar	214	
10 spheres2#2	10sph2#2noheat	0.01	34	laminar	120	flow only
	10sph2#2	0.01	34	laminar	131	
	10sph2#20,01	0.01	34	laminar	196	continuity $1e^{-4}$
	10sph2#20,1	0.1	338	laminar	840	
	10sph2#20,05	0.05	169	laminar	221	
	10sph2cool	0.05	169	laminar	221	cooled wall
	10sph2hsph	0.05	169	laminar	230	heated spheres
10sph2loc0,09	10sph2loc0,09flow	0.01	34	laminar	122	flow only
	10sph2loc0,09	0.01	34	laminar	232	

Table 7. Overview of the CFD runs of the Nu number checks.

48,467 element mesh

Run	v_{inlet} [m/s]	Reynolds	q [W]	flow regime	# iterations	remarks
nucheck1	0	0	0.88569826	laminar	10	
nuchv=0,1	0.1	348	6.465971	laminar	86	
nuchv=0,01	0.01	35	2.3465981	laminar	96	
nuchv=0,001	0.001	3	1.2056898	laminar	126	
nuchv=0,0001	0.0001	0.3	0.91367453	laminar	146	
nuchv=1	1	3478	9.9585943	laminar	66	
nuchv=10	10	34,777	10.542231	laminar	56	
nuchv=0,2	0.2	696	7.9864407	laminar	81	
nuchv=0,3	0.3	1043	8.7038507	laminar	76	
nuchv=0,4	0.4	1391	9.1141615	laminar	71	
nuchv=0,5	0.5	1739	9.3796244	laminar	71	
nuchv=0,6	0.6	2087	9.5650101	laminar	71	
nuchv=0,7	0.7	2434	9.7020092	laminar	66	
nuchv=0,8	0.8	2782	9.807136	laminar	66	
nuchv=0,9	0.9	3130	9.8909502	laminar	66	

7,216 element mesh

Run	v_{inlet} [m/s]	Reynolds	q [W]	flow regime	# iterations	remarks
nuchcv=0	0	0	0.88440394	laminar	100	residual $1e^{-8}$
nuchcv=0,00005	0.00005	0.2	0.90198213	laminar	63	
nuchcv=0,0001	0.0001	0.3	0.91404426	laminar	63	
nuchcv=0,001	0.001	3	1.1976821	laminar	57	
nuchcv=0,01	0.01	35	2.3113546	laminar	50	
nuchcv=0,1	0.1	348	6.4644365	laminar	47	
nuchcv=0,25	0.25	869	8.3975687	laminar	43	
nuchcv=0,5	0.5	1739	9.342061	laminar	41	
nuchcv=0,75	0.75	2608	9.7052526	laminar	39	
nuchcv=1	1.0	3478	9.8969774	laminar	38	

232,593 element mesh

Run	v_{inlet} [m/s]	Reynolds	q [W]	flow regime	# iterations	remarks
nuchfv=0	0	0	0.93173325	laminar	11	
nuchfv=0,0001	0.0001	0.3	0.93757417	laminar	316	
nuchfv=0,001	0.001	3	1.2231172	laminar	272	
nuchfv=0,01	0.01	35	2.3011611	laminar	161	
nuchfv=0,1	0.1	347	6.98336	laminar	129	
nuchfv=0,25	0.25	869	11.806903	laminar	130	
nuchfv=0,5	0.5	1739	15.641298	laminar	123	
nuchfv=0,75	0.75	2608	17.497665	laminar	117	
nuchfv=1	1.0	3478	18.583879	laminar	114	
nuchfv=10	10	34,777	22.099157	laminar	93	

Table 8. Overview of the CFD runs of the mesh comparisons.

Air used as fluid phase

Mesh	Run	v_{inlet} [m/s]	Reynolds	regime	# its.	remarks
99% ntlr	dtdp2nt99lr17	0.01	17	laminar		
	dtdp2nt99lr96	0.055	95 (96)	laminar	105	
	dtdp2nt99lr200	0.115	198 (200)	laminar	123	reverse flow
	dtdp2nt99lr500	0.2875	495 (500)	laminar	495	reverse flow
	dtdp2nt99lr1922	1.105	1903 (1922)	laminar		no convergence
99% ntlr	dtdp2nt99lr17turb	0.01	17	turbulent	2184	flow 862
	dtdp2nt99lr96turb	0.055	95 (96)	turbulent		flow 662
	dtdp2nt99lr200turb	0.115	198 (200)	turbulent	1105	flow 566
	dtdp2nt99lr500turb	0.2875	495 (500)	turbulent	973	flow separate
	dtdp2nt99lr1922turb	1.105	1903 (1922)	turbulent		
97% ntlr	dtdp2nt97lr17	0.01	16 (17)	laminar		
	dtdp2nt97lr96	0.055	93 (96)	laminar	97	
	dtdp2nt97lr200	0.115	194 (200)	laminar	108	reverse flow
	dtdp2nt97lr500	0.2875	485 (500)	laminar	536	reverse flow
	dtdp2nt97lr1922	1.105	1864 (1922)	laminar	700	no convergence

Mesh	Run	v_{inlet} [m/s]	Reynolds	regime	# its.	remarks
97% ntlr	dtdp2nt97lr17turb	0.01	16 (17)	turbulent	2447	flow 894
	dtdp2nt97lr96turb	0.055	93 (96)	turbulent	1517	flow 617
	dtdp2nt97lr200turb	0.115	194 (200)	turbulent	1159	flow 561
	dtdp2nt97lr500turb	0.2875	485 (500)	turbulent	806	
	dtdp2nt97lr1922turb	1.105	1864 (1922)	turbulent		
99.5%	dtdp2nt995lr17	0.01	17	laminar		
	dtdp2nt995lr96	0.055	96	laminar	101	
	dtdp2nt995lr200	0.115	199 (200)	laminar	119	
	dtdp2nt995lr500	0.2875	498 (500)	laminar	224	reverse flow
	dtdp2nt995lr1922	1.105	1912 (1922)	laminar	500	no convergence
99.5%	dtdp2nt995lr17turb	0.01	17	turbulent		
	dtdp2nt995lr96turb	0.055	96	turbulent	1126	flow 450
	dtdp2nt995lr200turb	0.115	199 (200)	turbulent	876	flow 390
	dtdp2nt995lr500turb	0.2875	498 (500)	turbulent	632	flow 307
	~nt995lr1922turb	1.105	1912 (1922)	turbulent		

Water used as fluid phase, $T_{wall,max}$ = 353 K

Mesh	Run	v_{inlet} [m/s]	Reynolds	regime	# its.	remarks
97% ntlr	dtdp297turb96wat	0.0038	93 (96)	turbulent	1625	
	dtdp297turb500wat	0.01978	485 (500)	turbulent	1024	
97% ntlr	dtdp297lam96wat	0.0038	93 (96)	laminar	194	
	dtdp297lam500wat	0.01978	485 (500)	laminar	269	
99% ntlr	dtdp299turb96wat	0.0038	95 (96)	turbulent	1660	
	dtdp299turb500wat	0.01978	495 (500)	turbulent	1050	
99% ntlr	dtdp299lam96wat	0.0038	95 (96)	laminar	213	
	dtdp299lam500wat	0.01978	495 (500)	laminar	320	
99.5%	dtdp2995turb96wat	0.0038	96	turbulent	956	
	dtdp2995turb500wat	0.01978	498 (500)	turbulent	765	
99.5%	dtdp2995lam96wat	0.0038	96	laminar	203	
	dtdp2995lam500wat	0.01978	498 (500)	laminar	329	

Hydrocarbon mixture used as fluid

Mesh	Run	v_{inlet} [m/s]	Reynolds	regime	# its.	remarks
97% ntlr	dtdp297turb96wat	0.02876	93 (96)	turbulent	1259	
	dtdp297turb500wat	0.1498	485 (500)	turbulent	857	
97% ntlr	dtdp297lam96wat	0.02876	93 (96)	laminar	181	
	dtdp297lam500wat	0.1498	485 (500)	laminar	400	reverse flow
99% ntlr	dtdp299turb96wat	0.02876	95 (96)	turbulent	1260	
	dtdp299turb500wat	0.1498	495 (500)	turbulent	860	
99% ntlr	dtdp299lam96wat	0.02876	95 (96)	laminar	217	
	dtdp299lam500wat	0.1498	495 (500)	laminar	483	reverse flow
99.5%	dtdp2995turb96wat	0.02876	96	turbulent	710	
	dtdp2995turb500wat	0.1498	498 (500)	turbulent	531	
99.5%	dtdp2995lam96wat	0.02876	96	laminar	198	
	dtdp2995lam500wat	0.1498	498 (500)	laminar	450	reverse flow

The actual particle Reynolds number is stated for each case in Table 8, using the reduced size of the spheres. All Reynolds numbers in parentheses are based on a sphere with a one-inch diameter.

Table 9. Overview of the CFD runs of the original 44-sphere mesh.

Run	ur.	v_{inlet} [m/s]	Reynolds	flow regime	# its.	remarks
44sphRe1922	all -0.2	1.105	1922	laminar		flow 718 RR[1]
44sphRe1833	all -0.2	1.054	1833	laminar		flow 718 RR[2]
44sphRe1724	all -0.2	0.991	1724	laminar	958	flow 705 RR[2]
44sphRe1624	all -0.2	0.934	1624	laminar	994	flow 553 RR[2]
44sphRe1477	all -0.2	0.849	1477	laminar	643	flow 353 RR[2]
44sphRe1346	all -0.2	0.774	1346	laminar	585	flow 341 RR[2]
44sphRe1221	all -0.2	0.702	1221	laminar	570	flow 225 RR[2]
44sphRe1097	all -0.2	0.631	1097	laminar	549	flow 309 RR[2]
44sphRe986	all -0.2	0.567	986	laminar	876	flow 125 RR[3]
44sphRe879	all -0.2	0.506	879	laminar	430	flow 150 RR[3]
44sphRe769	default	0.442	769	laminar	323	flow 312
44sphRe664	default	0.382	664	laminar	213	flow 203
44sphRe564	default	0.324	564	laminar	194	flow 184
44sphRe468	default	0.269	468	laminar	176	flow 166
44sphRe373	default	0.215	373	laminar	145	flow 132

RR, relaxed residuals: At higher Reynolds numbers in the touching-spheres model the residual values had to be relaxed to end the iteration process. The procedure results in a solution with a larger error. The higher the Reynolds numbers the more relaxation of the residual values was necessary.

[1] Residual value of continuity relaxed 50 times from 0.0001 to 0.005. Residual value of energy relaxed 5 times from 1e-6 to 5e-6.

[2] Residual value of continuity 0.0005. Residual value of energy 5e-6.

[3] Residual value of continuity 0.0003. Residual value of energy 3 e-6.

Table 10. Overview of CFD runs of the final 44-sphere mesh.

Run	ur.	v_{inlet} [m/s]	Reynolds	flow regime	# its.	remarks
44sphnthcRe1922	all -0.2	1.116	1922	turbulent	595	flow separate
44sphnthcRe1833	all -0.2	1.065	1833	turbulent	597	flow separate
44sphnthcRe1724	all -0.2	1.001	1724	turbulent	596	flow separate
44sphnthcRe1624	all -0.2	0.943	1624	turbulent	470	
44sphnthcRe1477	all -0.2	0.858	1477	turbulent	453	
44sphnthcRe1477	all -0.2	0.858	1477	turbulent	1203	round off
44sphnthcRe1346	all -0.2	0.782	1346	turbulent	455	
44sphnthcRe1221	all -0.2	0.709	1221	turbulent	457	
44sphnthcRe1097	all -0.2	0.637	1097	turbulent	454	
44sphnthcRe986	all -0.2	0.537	986	turbulent	465	
44sphnthcRe879	all -0.2	0.511	879	turbulent	468	
44sphnthcRe769	all -0.2	0.447	769	turbulent	485	
44sphnthcRe664	all -0.2	0.386	664	turbulent	509	
44sphnthcRe564	all -0.2	0.328	564	turbulent	541	
44sphnthcRe468	all -0.2	0.272	468	turbulent	583	
44sphnthcRe373	all -0.2	0.216	373	turbulent	639	
~nthcRe373lam	default	0.216	373	laminar	121	
~nthcRe468lam	default	0.272	468	laminar	133	
~nthcRe564lam	default	0.328	564	laminar	145	
~nthcRe664lam	default	0.386	664	laminar	160	
~nthcRe769lam	default	0.447	769	laminar	176	

Appendix 2 Overview of the physical experiments

The physical experiments were all very similar. Table 11 shows all bed lengths at which measurements were taken. Table 12 gives an overview of all the Reynolds numbers for an entire measurement series. At all the bed lengths measurements were taken over the entire Reynolds number range.

Table 11. Overview of the different physical experimental series.

total bed length (z) [m]	heated bed length (L) [m]	number of spheres in bed
0.420	0.260	44
0.384	0.224	40
0.348	0.188	36
0.312	0.152	32
0.276	0.116	28
0.240	0.044	24
0.204	0.036	20
0.168	0.008	16
0.132	-0.028	12

One measurement at one Reynolds number and one bed length consists of four separate measurements. The thermocouple cross was placed at four different relative positions, 0, 15, 30 and 45 degrees all relative to the initial position, this way more data was gathered to get a better radial average profile.

Table 12. All physical experiments for bed length 0.348 m, Reynolds values identical for all other bed lengths.

rotameter	percentage airflow	pressure drop [psi]	Reynolds
27	20	0.1	373
27	25	0.2	468
27	30	0.3	564
27	35	0.6	664
27	40	1.0	769
27	45	1.5	879
27	50	1.8	986
27	55	2.2	1097
27	60	2.9	1221
27	65	3.5	1346
27	70	4.2	1477
27	75	5.2	1624
50	26	6.5	1724
50	27	7.5	1833
50	28	8	1922

Appendix 3 Structural details of the different CFD models

This appendix contains structural information about the different geometries used. It is added so that if necessary the models can be recreated for further research.

Nusselt check model structural details

The model created for checking the Nusselt number at no flow conditions consisted of one solid sphere in a flowing medium. The fluid was flowed through a duct rather than having an infinite flowing medium to be able to create a model with a reasonable size.

The two-inch (50.8 mm) diameter sphere was created with its center at the Cartesian coordinate (0,10,10). The units in creation of this model were inches. The enclosing duct entrance plane is at $y = 3$ with $-7 < x < 7$ and $3 < z < 17$. The exit plane is of the same dimensions at $y = 35$.

For mesh creation node spacing on all edges needs to be defined. The sphere, consisting of four surfaces, resulting in four equal sized edges per circumference has 10 nodes per edge; this is a node spacing of 0.175 inch. The node spacing on the duct is set at 1.00 inch resulting in 15 nodes on all sides on the inlet and exit planes and 33 along the walls of the duct.

For the coarser mesh with 7,216 elements, the node spacing on the sphere edges was set to 0.393 inch, 5 nodes per edge. The node spacing on the duct was set to 2 inch resulting in 8 nodes on the edges of the inlet and exit planes and 17 nodes along the duct wall. For the finer mesh with 323,593 elements the original node spacing was used on the sphere, 10 nodes per edge. The node spacing on the duct was reduced to 0.5 inch, resulting in 29 nodes on the edges of the inlet and exit plane and 65 nodes along the duct wall.

10-sphere model structural details

The model consists of a tube with 10 solid spheres located inside the tube. The fluid flows through the tube, bottom to top, around the spheres inside. Three slightly differing meshes were created for this geometry. All three meshes were based on the same topology.

The base topology was created in millimeters and consists of a tube with an axis running from the Cartesian coordinates (0,0,0) to (0,0,250). The radius of the tube was 59.6311.

The centers of the spheres in the tube were located at specific Cartesian coordinates as they are stated in Table 13. The way the spheres are divided into the several axial layers is 1,4,4,1.

Table 13. Location of the sphere centers in the 10-sphere topology.

layer	x	y	z
1	0	0	34.7
2	24.7	24.7	69.6311
2	24.7	-24.7	69.6311
2	-24.7	-24.7	69.6311
2	-24.7	24.7	69.6311
3	34.9311	0	111.1714
3	0	34.9311	111.1714
3	-34.9311	0	111.1714
3	0	-34.9311	111.1714
4	0	0	146.1024

Initially the 10spheres mesh was created with spheres with a radius of 24.7 mm therewith creating a model in which all contact points were actually touching. In the 10spheres mesh all solids were aluminum, the default solid in Fluent UNS.

The 10spheres2 mesh used the same topology as the 10spheres mesh with aluminumoxide spheres, as were used in the ANSYS model. The Al_2O_3 was defined with

a density of 2000 kg/m^3, a thermal conductivity of 1.2 W/m·K and a heat capacity of 800 J/kg·K.

The 10spheres2#2 mesh uses the exact copy of the ANSYS model, in which the spheres have a radius of 24.7 mm and do not quite touch each other nor the walls. This model facilitated higher flow velocities and was used for the direct comparison. The values given in Table 13 are for the adapted ANSYS model with actual contact points, the original model had a cylinder with a radius of 60 mm and spheres located at the points given in Table 14.

Table 14. Location of the sphere centers in the original ANSYS 10-sphere topology.

layer	x	y	z
1	0	0	34.7
2	24.8	24.8	69.5
2	24.8	-24.8	69.5
2	-24.8	-24.8	69.5
2	-24.8	24.8	69.5
3	35.07	0	110.98
3	0	35.07	110.98
3	-35.07	0	110.98
3	0	-35.07	110.98
4	0	0	146

The mesh density in all the 10-sphere geometries described above was based on the node spacing on the spheres. Again 10 nodes per ¼ circumference were used as a design parameter, this resulted in a node spacing of 4.31 mm, and this same node spacing was used on the cylinder wall. The total mesh size for the model with touching spheres was about 207,100 cells, the exact copy of the ANSYS model had approximately199,600 cells.

A third mesh, 10sph2loc0,09, used the original touching spheres and tried to facilitate higher flow velocities by refining the mesh locally at the contact points.

The mesh density and therefore the node spacing in this locally refined mesh was different than in the other 10-sphere models. The edges on the spheres facing other spheres were given an increased node density, 10 to 21, resulting in a node spacing of 1.9 mm. The edges on the cylinder were given a varying distribution, a higher density at the contact points with a node spacing of 1.9 mm and a lower density at the other parts with a node spacing of approximately 6.7 mm. The total mesh size was about 377,300 cells.

44-sphere final model details

The 44sphere model consists of a long (25 inches) narrow (2 inch diameter) tube filled with a 44 sphere fixed bed. This model was also initially created with touching spheres and later adapted to have both slightly smaller spheres and a mesh locally refined around the near contact points.

The cylinder is divided into two separate sections, the heated section and the calming section. All the wall surfaces in the heated section are merged into one complete surface. The wall surfaces in the calming section were sub-divided into several axial sections. These axial sections are based on the sphere layers as the wall surfaces run between the contact areas of the sphere layers. The calming section ends at layer nine and is sub-divided in 9 layers.

Table 15. Axial (z) coordinates of the 22 layers of spheres in the 44-sphere model.

layer	1	2	3	4	5	6	7	8	9	10	11
z	1	1.7071	2.4142	3.1213	3.8284	4.5355	5.2426	5.9497	6.6569	7.3640	8.0711
layer	12	13	14	15	16	17	18	19	20	21	22
z	8.7782	9.4853	10.1924	10.8995	11.6066	12.3137	13.0208	13.7279	14.4350	15.1421	15.8492

There are 22 layers of 2 spheres which are alternating next to each other in either x or y direction at (1,0), (-1,0) or (0,1), (0,-1) at different z coordinates, all units are in inches. The topology was built with the first layer of spheres at z = 1 on the x-axis, all other axial (z) coordinates are given in Table 15.

Sphere diameters were based on the original model, in which they were touching each other and the walls and were 1 inch. To facilitate turbulent solutions the sphere diameters were reduced to 99% of the original, 0.99 inch.

Node distribution on the spheres is not uniform, the density increases towards the sphere contact points, node spacing near the contact points is 0.06 inch away from the contact points it is 0.11 inch. There are 11 nodes on each quarter circumference. Node distribution on the cylinder wall in the packed region is similar, 0.06 inch near contact points and 0.12 inch away from the contact points. There are 20 nodes on a quarter circumference of the cylinder. The node distribution at the flow entrance plane is uniform with a node spacing of 0.11 inch; at the outlet the uniform node spacing is 0.26 inch. On the cylinder wall from the packed region to the outlet the node distribution gradually coarsens, from 0.11 inch near the bed to 0.26 inch near the outlet. The resulting mesh has 429,100 cells.

Appendix 4 CFD data and experimental fits at Re = 986

As was stated in the text this appendix is a collection of comparisons of CFD results with experimental data at a Reynolds number of 986 at the 9 different bed depths at which experiments were conducted, as stated in Table 11. Comparisons at lower bed depths are not considered valid comparisons due to differences in flow patterns between the experiments and the CFD simulations. It can be seen that at bed lengths other than z = 0.420 the radial temperature profiles are qualitatively different, especially at longer bed length the CFD simulation shows a lower temperature near the center of the bed.

In Figure 45 and Figure 46 the correction for the experimental result had to be adjusted to not indicate temperatures below the inlet temperature, which would be an incorrect assumption.

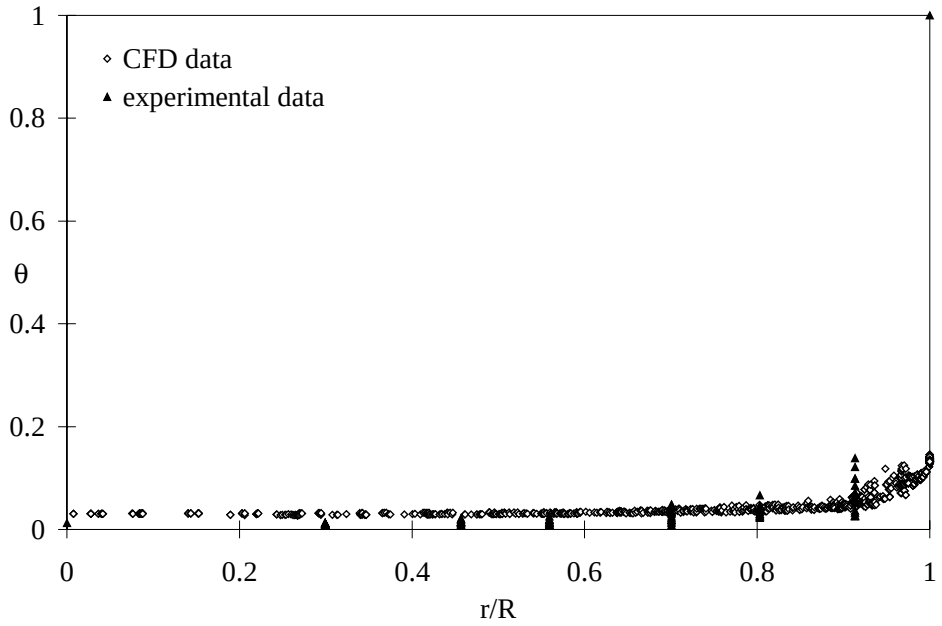

Figure 45. Comparison of CFD and experimental results at z = 0.132.

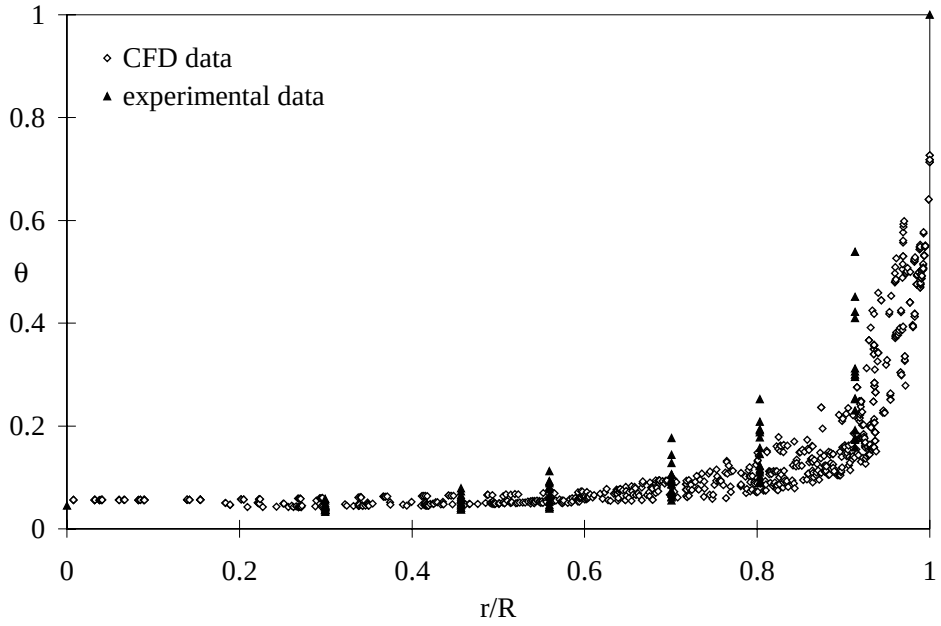

Figure 46. Comparison of CFD and experimental results at z = 0.168.

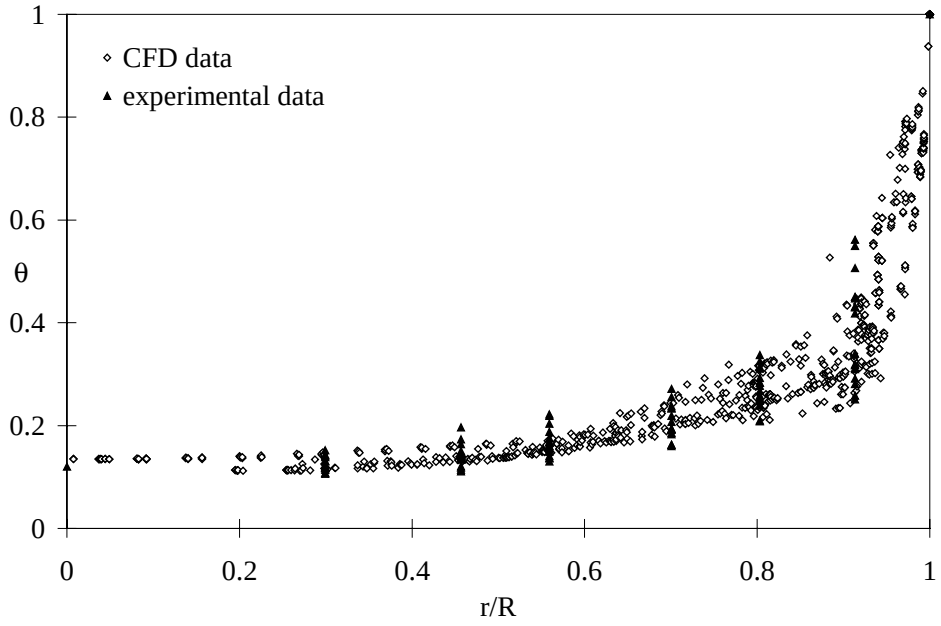

Figure 47. Comparison of CFD and experimental results at z = 0.204.

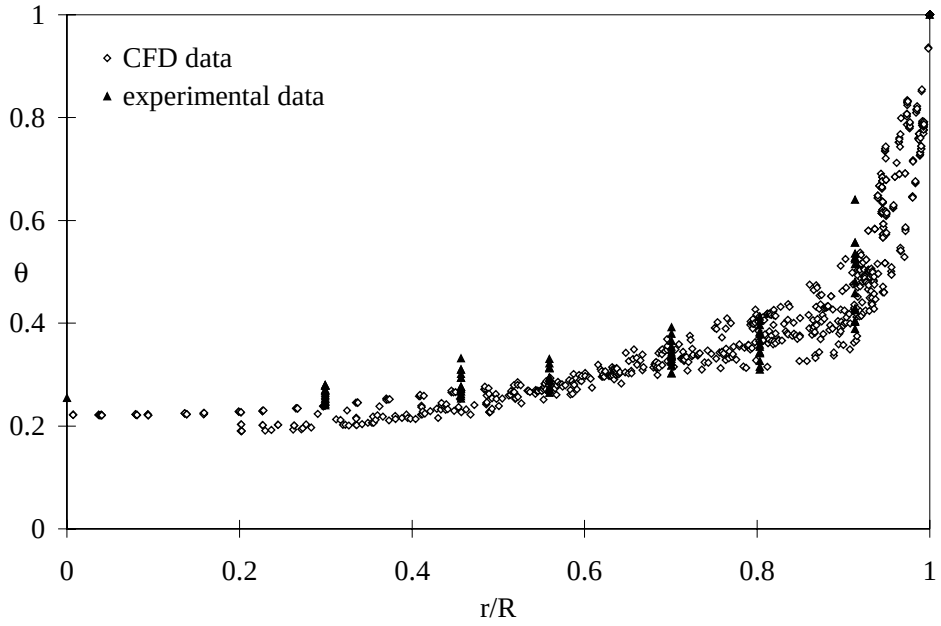

Figure 48. Comparison of CFD and experimental results at z = 0.240.

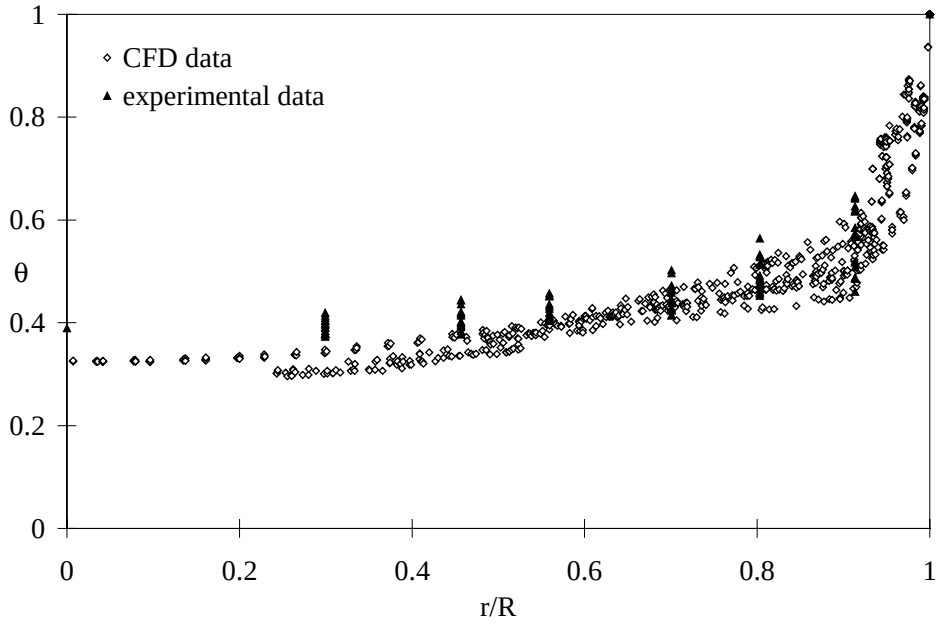

Figure 49. Comparison of CFD and experimental results at z = 0.276.

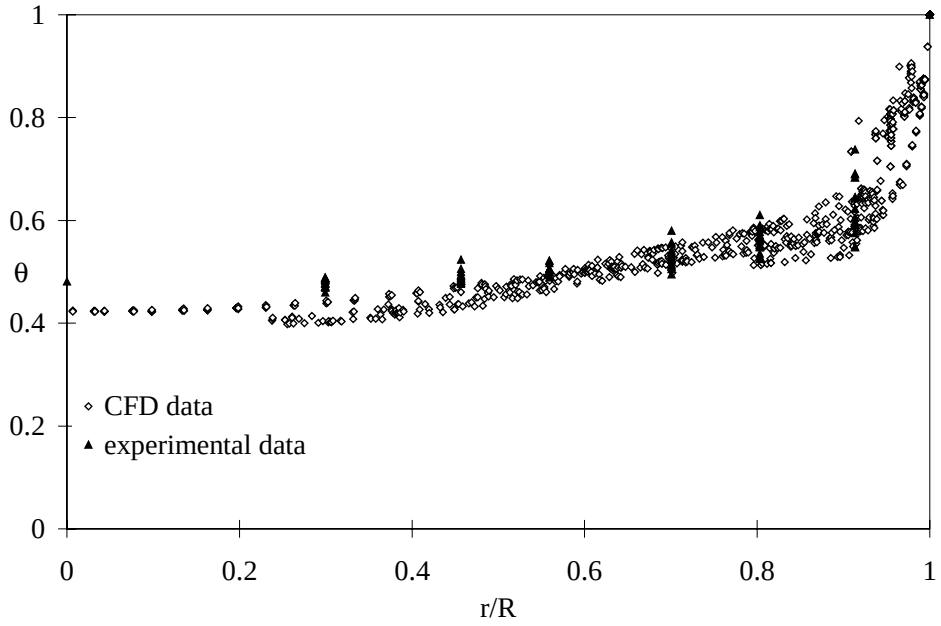

Figure 50. Comparison of CFD and experimental results at z = 0.312.

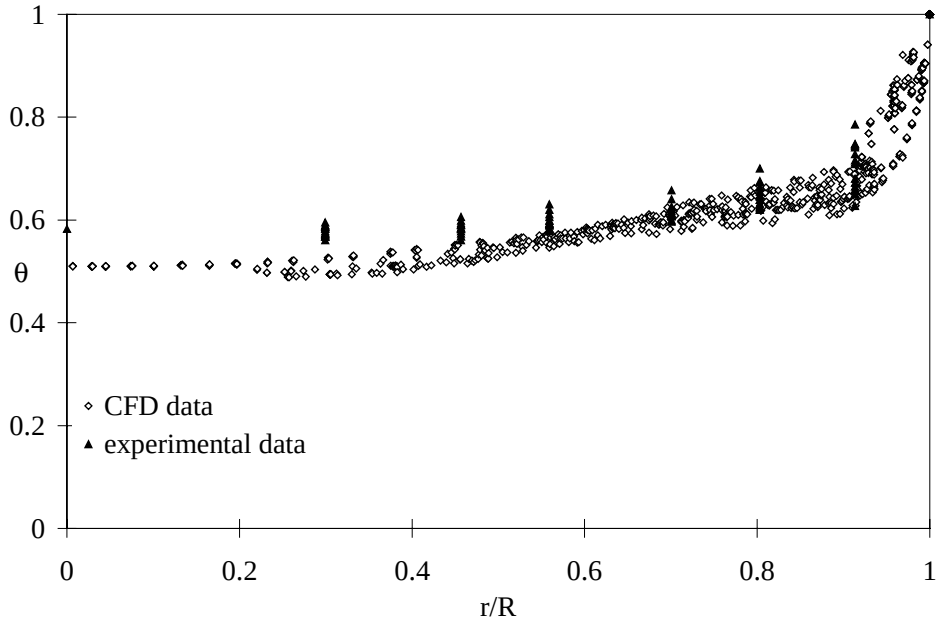

Figure 51. Comparison of CFD and experimental results at z = 0.348.

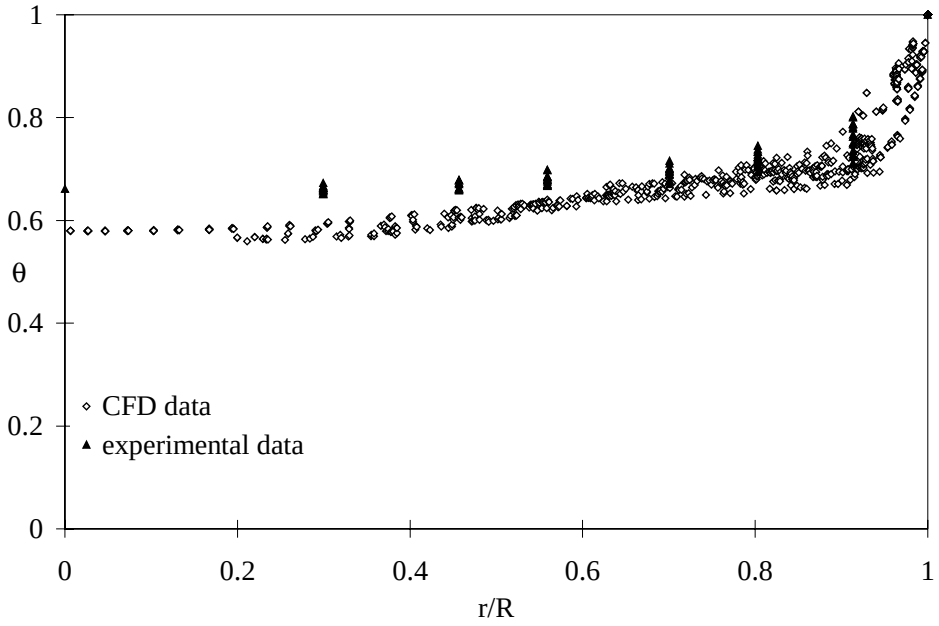

Figure 52. Comparison of CFD and experimental results at z = 0.384.

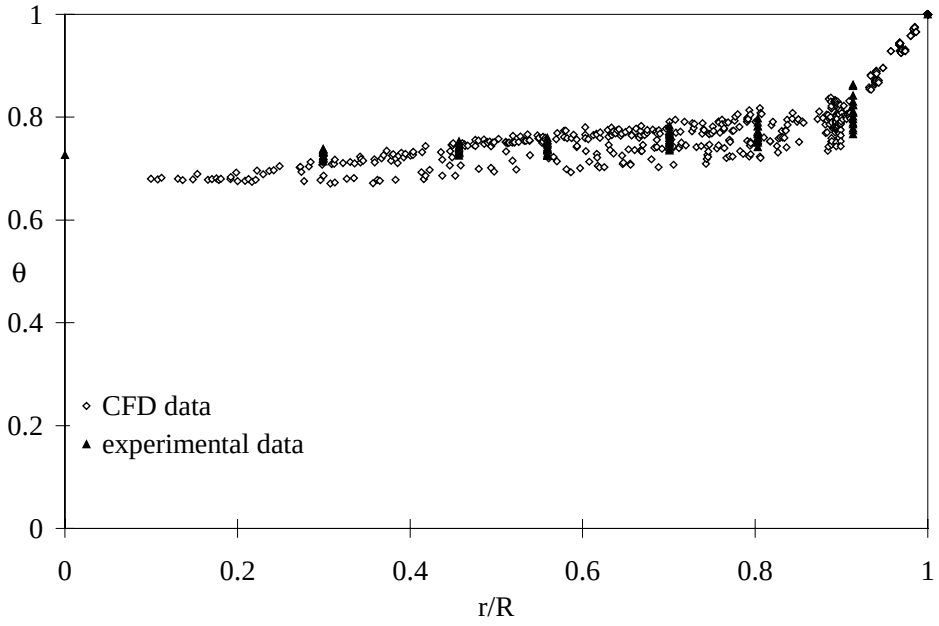

Figure 53. Comparison of CFD and experimental results at z = 0.420.